UNIVERSITY OF CALIFORNIA, SAN DIEGO

Electronic Properties of Low-Dimensional Systems

A dissertation submitted in partial satisfaction of the
requirements for the degree
Doctor of Philosophy

in

Physics

by

Aleksandr Rodin

Committee in charge:

Professor Michael Fogler, Chair
Professor Michael Anderson
Professor Prabhakar Bandaru
Professor Michael Holst
Professor Congjun Wu

2012

The dissertation of Aleksandr Rodin is approved, and it is acceptable in quality and form for publication on microfilm and electronically:

_____

_____

_____

_____

_____
Chair

University of California, San Diego

2012

DEDICATION

To my wife.

EPIGRAPH

What we're talking about here is how to deal
with a problem that has no solution.
—A. and B. Strugatsky

TABLE OF CONTENTS

LIST OF FIGURES

ACKNOWLEDGEMENTS

I would like to express my utmost gratitude to Professor Michael M. Fogler for his guidance over the past four years. It is his patience and enthusiasm that allowed me to reach this point of my academic career. This, without a doubt, would not have been possible without Professor Fogler's dedication to and involvement in his students' development into scientists.

I am also grateful to the group of Professor Dimitri Basov for giving me the opportunity to take part in their exciting project. This collaboration has provided me with invaluable experience and given me a chance to be a part of a larger scientific community.

My thanks go to my roommates who have been nothing other than great. I am thrilled about never having to deal with drama, allowing me to keep my sanity.

I thank all my friends for being there. This experience has been not only about academics, but also about forging new friendships and strengthening old ones. All the friends, near and far, have helped me through these years. Countless nights of homework, incalculable cups of tea, and innumerable bottles of various beverages made the experience, for the most part, unforgettable.

I thank my family for their endless support that never waivered. Their trust in me provided the motivational boost that helped me when I became overwhelmed. Their love gave me comfort to get me through the rough patches of the past four years.

Finally, I am grateful to my wife. Her understanding and patience allowed me to complete this journey. Her gentle, yet serious pep talks got me out of the worst apathy and gave me the energy that I needed. It is her cool, reasonable mind that managed to defuse me when the stress level approached the boiling point. It is her love and devotion that got me to where I am now.

Chapter 1 includes parts of the following published works: "Hopping transport in systems of finite thickness or length"(PRB, 2011); "Apparent Power-Law Behavior of Conductance in Disordered Quasi-One-Dimensional Systems" (PRL, 2010); "Numerical studies of variable-range hopping in one-dimensional systems" (PRB 2009) by A. S. Rodin and M. M. Fogler.

VITA

2012	Ph. D. Physics, University of California, San Diego, 2012. Advisor: Professor Michael M. Fogler.
2011	CPhil in Physics, University of California, San Diego, 2011.
2008	M. S. Physics, University of California, San Diego, 2008.
2007	B. S. Physics, *magna cum laude*, University of Southern California, 2007.

PUBLICATIONS

Z. Fei, A. S. Rodin, G. O. Andreev, W. Bao, A. S. McLeod, L. M. Zhang, G. Dominguez, M. Thiemens, M. M. Fogler, A. H. Castro-Neto, C. N. Lau, F. Keilmann, D. N. Basov, "Gate-tunable plasmons in graphene revealed by infrared nano-imaging", submitted for publication.

A. S. Rodin, M. M. Fogler, "Hopping transport in systems of finite thickness or length", Phys. Rev. B **84**, 125447, (2011).

A. S. Rodin, M. M. Fogler, "Apparent Power-Law Behavior of Conductance in Disordered Quasi-One-Dimensional Systems", Phys. Rev. Lett. **105**, 106801, (2010).

A. S. Rodin, M. M. Fogler, "Numerical studies of variable-range hopping in one-dimensional systems", Phys. Rev. B **80**, 155435, (2009).

ABSTRACT OF THE DISSERTATION

Electronic Properties of Low-Dimensional Systems

by

Aleksandr Rodin

Doctor of Philosophy in Physics

University of California, San Diego, 2012

Professor Michael Fogler, Chair

This work deals with transport and general electronic phenomena in low-dimensional systems. The first chapter is dedicated to Variable Range Hopping. It starts with a brief review of the general hopping formalism, based on previous work. Next, new methods and results are presented and discussed. In particular, studies of both Ohmic and non-Ohmic regime are performed and the stark differences between the two are elucidated. In addition, apparent power law dependence of current on voltage in disordered one-dimensional materials is analyzed. The results obtained compare favorably with the experiments. Finally, the behavior of the conducting network in d dimensions is discussed using the percolation approach.

The second chapter deals with plasmonic effects in graphene. After giving a short introduction to graphene and plasmonic behavior, current work is presented.

Charge oscillations in graphene half-plane are discussed and compared with experimental results obtained from near-field microscopy. In addition, plasmonic oscillations in a "narrow-flake" geometry are analyzed analytically and numerically, showing good agreement between the two methods.

Chapter 1

Introduction

For somebody living in a three-dimensional world, it may be hard to imagine what it is like for a physical system to have less than three dimensions. At the first glance, solving low-dimensional problems might seem like an interesting exercise with little connection to reality. Nevertheless, the discussion of low-dimensional systems if far from purely academic. It is true that every physical structure that we encounter possesses a full set of dimensions, even if the aspect ratio makes some more apparent than others. Luckily, such an aspect ratio can also deem some dimensions more important than others, effectively reducing the dimensionality of the system. Such is the case for, say, nanowires, where the radius is dwarfed by the length. This results in the free motion of charge carriers along the wire and the confinement in the transverse direction. Even more dramatic is the case of nanoribbons and nanotubes. In the first case, the boundary conditions impose certain requirements on the transverse momentum, turning the system into a collection of one-dimensional channels labeled by the transverse momentum quantum number. Similarly, for the case of the nanotubes, the angular periodicity also introduces independent one-dimensional channels.

It is not only quasi-one-dimensional systems that are important. With the discovery of graphene—a carbon allotrope initially considered unstable—we have been introduced to a truly two-dimensional system. The novel and exciting properties of this system make it a promising candidate for a number of applications, ranging from chemical sensors, to touch screens, all the way to transistors.

The world of low-dimensional systems is very diverse and full of phenomena specific to a particular dimensionality. This, coupled with the plethora of potential applications warrants a detailed study of these systems. This work is divided into two chapters: the first one explores hopping transport with emphasis on one dimension; the second one provides an introduction to the current work being done on graphene.

Chapter 2

Hopping Transport in Disordered Systems

2.1 General Hopping Formalism

2.1.1 Introduction

Mesoscopic systems occupy a position that is between the "common" macroscopic systems on one side and the "exotic" nanoscopic ones on the other. It is precisely this middle-ground position between the two worlds that makes such systems both very exciting and notoriously difficult to analyze. Unlike nanostructures, composed of a few to a few hundreds of atoms, mesoscopic structures are too large to be solved using traditional quantum mechanical techniques which involve writing down Schrödinger equation and using a computer to obtain the result. On the other hand, these mesoscopic systems are still too small compared to macrosystems to rely on the self-averaging that comes with size. Indeed, the presence of mesoscopic fluctuations is one of the key traits of the micron-size systems. These fluctuations arise primarily due to disorder that is practically unavoidable in these systems. Aside from ultra-pure crystals, all mesoscale structures possess a certain degree of disorder which arises primarily due to structural defects and impurities that are found inside the system.

The types of mesoscopic are too numerous to list completely, but some

broader classes are nanowires, thin films, nanoribbons, and, very importantly, polymer structures. Despite the prefix nano-, nanowires and nanoribbons are mesoscopic objects, described by a nanodimension only in the transverse direction. Mesoscopic systems are ubiquitous and, with organic polymers rapidly developing in the field of relatively cheap electronics, understanding of disordered systems is as important as ever. The first chapter of this work is dedicated to hopping transport in disordered materials. We begin by introducing the fundamentals of the hopping transport that have been developed over the years. [45, 17, 84, 50, 83, 77, 87]

2.1.2 Variable Range Hopping

As we have already mentioned, mesoscopic systems are typically disordered. The consequences of this disorder are far reaching. However, the most basic one, at least at the first glance, is the fact that it impedes electronic transport even in otherwise conducting materials. Unlike perfect crystals, where Bloch waves propagate freely, defects act as scattering centers for electrons, preventing the ballistic transport. Ultimately, the disorder localizes electrons, resulting in the so-called Anderson insulator. Instead of moving freely through the system, electrons are bound to a localized state (LS) with an exponentially decaying wavefunction.

Despite its generally negative effect on conductivity, disorder can actually facilitate electronic transport. Consider an insulator with the Fermi level inside the gap. Assuming that the gap is large enough to prevent thermal activation, the system will not conduct. The presence of disorder, however, creates LS at various energies throughout the sample. Therefore, if these LS are located close to the Fermi level, they can be utilized by the charge carriers for moving through the sample. Due to the exponentially decaying nature of the wavefunctions, the charges have to tunnel ("hop") between the individual LS. In addition, since LS have different energies, charges require phonons to be excited to move to higher energy levels and emit a phonon when they hop down.

It is natural to assume that LS are distributed randomly throughout the system. This means that tunneling lengths for different hops vary, which gives rise to the term Variable Range Hopping (VRH).

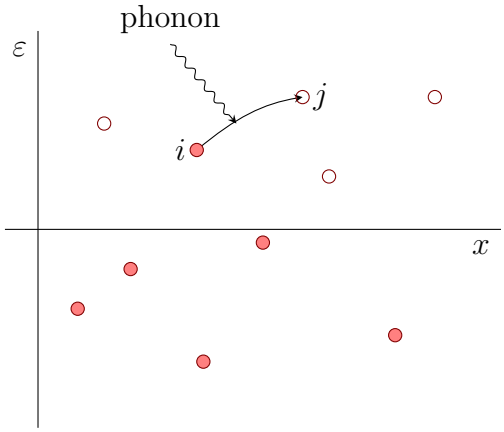

Figure 2.1: Phonon-assisted transport between localized states. Filled circles represent occupied LS; empty circles are unoccupied.

Since tunneling between all LS is allowed, the system can be regarded as a network of interconnected LS where the current from one LS (i) to another (j) is given by

$$I_{ij} = q\left(\Gamma_{i\to j} - \Gamma_{j\to i}\right) , \tag{2.1}$$

where $\Gamma_{i\to j}$ is the transition (hopping) rate from i to j and q is the charge. Equation (2.1) is the foundation of all the machinery that will be introduced in the later sections.

2.1.3 Transition Rate

Having defined the current between two localized states, we now turn to the transition rate. First and foremost, the transition rate depends on the presence of a charge carrier in the initial state i. In addition, the final state has to be vacant for the transition to take place. This means that the number of transitions per unit time is given by

$$\Gamma_{ij} = \langle \gamma_{ij} n_i (1 - n_j) \rangle , \tag{2.2}$$

where n_i and n_j are the occupation factors of the respective LS and the average is performed over time. All the quantities inside the brackets vary with time, which complicates the problem greatly. At this point, a key approximation is made: all the quantities inside the brackets are set to their average values instead of

fluctuating in time. For the occupation numbers it means that they are now given by Fermi-Dirac distribution

$$f_i = \frac{1}{e^{(\varepsilon_i - \eta_i)/T} + 1} \,. \tag{2.3}$$

Note that the energy of the LS and the local electrostatic potential are

$$\varepsilon_i = \varepsilon_i^0 + q\Phi_i \,, \tag{2.4}$$

$$\eta_i = \mu_i + q\Phi_i \,, \tag{2.5}$$

where ε_i^0 and μ_i are the bare energy and chemical potential of the state, respectively, and Φ_i is the electrostatic potential shift.

Recall that the hopping transport is phonon-assisted. This means that the transition rate depends on the availability of phonons of the correct energy, given by the Bose-Einstein distribution. Depending whether ε_i is greater or less than ε_j, a phonon will be either emitted or absorbed. This allows us to write down

$$\Gamma_{i\to j} = \Gamma_{ij} f_i (1 - f_j) \times \begin{cases} N(\Delta\varepsilon) \,, & \Delta\varepsilon > 0 \,, \\ N(|\Delta\varepsilon|) + 1 \,, & \Delta\varepsilon \leq 0 \,, \end{cases} \tag{2.6}$$

where $\Delta\varepsilon$ is the energy difference in the hop:

$$\Delta\varepsilon = \varepsilon_j - \varepsilon_i \,. \tag{2.7}$$

The final part that needs to be determined is the prefactor Γ_{ij}. First, one expects the transition rate to be suppressed due to localization. This introduces the tunneling term $\exp(-2x_{ij}/a)$ to the transition rate expression, where x_{ij} is the distance between the LS and a is the localization length. In addition, the prefactor contains algebraic dependence on the energy difference to counteract the divergence of $N(|\Delta\varepsilon|)$ at $\Delta\varepsilon \to 0$. This means that the prefactor is

$$\Gamma_{ij} = \Gamma_{ji} = G_0 |\Delta\varepsilon| e^{-\frac{2x_{ij}}{a}} \,, \tag{2.8}$$

where the parameter G_0 of dimension of conductance is related to electron-phonon coupling.

Assuming that $\varepsilon_i < \varepsilon_j$, we can now write down the expression for the current between the two LS from Eq. (2.1) with $q = 1$:

$$\begin{aligned}
I_{ij} &= \Gamma_{ij}\left\{f_i(1-f_j)N(|\Delta\varepsilon|) - f_j(1-f_i)[N(|\Delta\varepsilon|)+1]\right\} = \\
&= \Gamma_{ij}\left[N(|\Delta\varepsilon|)(f_i - f_j) - f_j(1-f_i)\right] = \\
&= \Gamma_{ij}\left[\frac{e^{-|\Delta\varepsilon|/2T}}{2\sinh\left|\frac{\Delta\varepsilon}{2T}\right|}\left(\frac{e^{-(\varepsilon_i-\eta_i)/2T}}{2\cosh\left(\frac{\varepsilon_i-\eta_i}{2T}\right)} - \frac{e^{-(\varepsilon_j-\eta_j)/2T}}{2\cosh\left(\frac{\varepsilon_j-\eta_j}{2T}\right)}\right) - \right. \\
&\left. - \frac{e^{-(\varepsilon_j-\eta_j)/2T}}{2\cosh\left(\frac{\varepsilon_j-\eta_j}{2T}\right)}\frac{e^{(\varepsilon_i-\eta_i)/2T}}{2\cosh\left(\frac{\varepsilon_i-\eta_i}{2T}\right)}\right] = \\
&= \frac{\Gamma_{ij}\left[e^{-|\Delta\varepsilon|/2T}\sinh\left(\frac{\varepsilon_j-\eta_j-\varepsilon_i+\eta_i}{2T}\right) - \exp\left(-\frac{\varepsilon_j-\eta_j-\varepsilon_i+\eta_i}{2T}\right)\sinh\left|\frac{\Delta\varepsilon}{2T}\right|\right]}{4\sinh\left|\frac{\Delta\varepsilon}{2T}\right|\cosh\left(\frac{\varepsilon_j-\eta_j}{2T}\right)\cosh\left(\frac{\varepsilon_i-\eta_i}{2T}\right)} = \\
&= \frac{G_0|\Delta\varepsilon|e^{-2x_{ij}/a}\sinh\left(\frac{\eta_i-\eta_j}{2T}\right)}{4\sinh\left|\frac{\Delta\varepsilon}{2T}\right|\cosh\left(\frac{\varepsilon_j-\eta_j}{2T}\right)\cosh\left(\frac{\varepsilon_i-\eta_i}{2T}\right)}\,. \qquad (2.9)
\end{aligned}$$

It is possible to absorb the numerical factor of 4 from the denominator into G_0 to avoid extraneous terms and define $\delta\eta = \eta_i - \eta_j$. In the expression above, the direction of the current is determined by the applied voltage through the sinh term in the numerator, whereas the magnitude depends also on the temperature and the energies of the LS.

Note that the current has a nonlinear dependence on the voltage $\delta\eta$. If, however, the applied voltage tends to zero, one ends up with the Ohmic regime. In this case, it is possible to expand the hyperbolic sine in the numerator. Additionally, one can also measure all the energies in the system from the common electrochemical potential η_0, which yields

$$I_{ij} = G_0\frac{|\Delta\varepsilon|}{2T}\frac{e^{-\frac{2x_{ij}}{a}}}{\cosh\left(\frac{\varepsilon_j}{2T}\right)\cosh\left(\frac{\varepsilon_i}{2T}\right)\sinh\left|\frac{\varepsilon_i-\varepsilon_j}{2T}\right|}\delta\eta = \frac{\delta\eta}{R_{ij}}\,, \qquad (2.10)$$

where we have defined the resistance between i and j in accordance with Ohm's law. For sufficiently low temperatures, it is possible to approximate the resistance as

$$R_{ij} \approx R_0 e^{u_{ij}}\,, \quad u_{ij} = \frac{2x_{ij}}{a} + \frac{|\varepsilon_i| + |\varepsilon_j| + |\varepsilon_i - \varepsilon_j|}{2T}\,, \qquad (2.11)$$

with a constant R_0. In the Ohmic regime, all the LS of the system for a so-called Miller-Abrahams resistor network. [60] The conductivity of such a network is typically described by Mott law, discussed in the next section.

Before we conclude this section, recall that we need a formula for the electrostatic potential Φ_i. It is determined by charges on the source and drain leads, and the perturbation of the electron density inside the sample (given by the occupation factors f_i). The relative importance of these contributions depends on the exact geometry of the device. We consider a typical situation where there is a metallic gate positioned parallel to the wire, with C denoting the capacitance to the gate per unit length of the wire. We further assume that the capacitive coupling to the leads is much smaller and can be neglected. In this case, we find

$$\Phi(x) = \frac{qn(x)}{C}, \tag{2.12}$$

where $n(x)$ is the deviation of the local density from equilibrium. Neglecting fluctuations in the local density of states and any correlation effects, we can directly relate $n(x)$ to the local chemical potential using the density of states g, $n(x) = g\mu(x)$, which implies

$$q\Phi_i = \frac{q^2 g}{C}\,\mu_i = (\epsilon - 1)\,\mu_i = \eta_i \left(1 - \frac{1}{\epsilon}\right)\,, \tag{2.13}$$

where ϵ is the dielectric constant, given by

$$\epsilon = 1 + (q^2 g/C)\,. \tag{2.14}$$

In comparison, in previous literature it was common to approximate Φ_i simply by $-Fx_i$, i.e., to assume that the electric field in the system is uniform. Although this may be reasonable for a sample of dimension $d > 1$ with bulk leads, it is inappropriate for a 1D geometry, as will be discussed later. In this work, we concentrate on the case of weak electron interactions. This means that we set $\epsilon = 1$, which allows us to replace all the energies in Eq. (2.9) by their bare values.

2.1.4 Mott Law

If one wanted to compute the Ohmic conductivity of a disordered system described by the Miller-Abrahams network, the first impulse might be to use the standard Kirchoff rules and solve the resistor problem. Very quickly, however, it becomes apparent that this is not a practical way of approaching the problem since

each LS is connected to $N-1 \gg 1$ other states and the total number of resistors is $N!$. Instead, we adopt a different approach.

As one can see from Eq. (2.11), the resistances of the links in the Miller-Abrahams network vary exponentially. Because of this, if one were to drive the current from one end of the system to another, not all links would contribute equally as the current will prefer the path of the least resistance. In a sense, there is a competition in the system: while highly resistive links are common, they are disfavored by the current; on the other hand, "easy" hops are preferred, but they are rare. Therefore, we are looking for the smallest u which will form a connected subnetwork.

Usually, one employs the percolation theory [87] to find this subnetwork. Following the percolation formalism for bond problems, [87] one can designate all links in the resistor network with $u_{ij} \leq u$ as open bonds and those with $u_{ij} > u$ as closed, where u_{ij} is given by Eq. (2.11). Varying u is similar to changing the fraction of open bonds in a traditional percolation problem.

From Eq. (2.11) one can see that only sites with energies between $-uT$ and uT can participate in the transport.

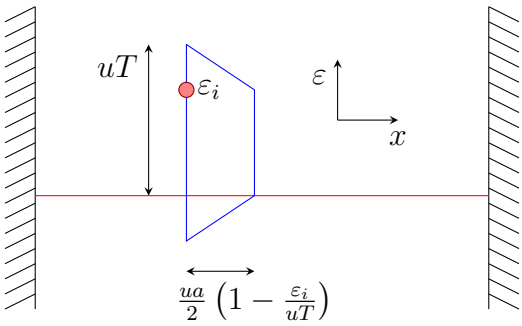

Figure 2.2: Energy-position space for a 1D system. Upper, lower, and right sides of the quadrilateral represent the contour where site j has to be found for $u_{ij} = u$. The red line is the Fermi level.

It is important for this argument that $uTga^d \gg 1$, where g is assumed to be constant. This requirement means that the available network is dense enough for the percolation approach to work. The opposite situation will be discussed later.

In the percolation theory, disordered systems are typically characterized

by their open bond density and here we compute its dependence on u. For a d-dimensional system it is given by

$$B(u) = \frac{\int_{-uT}^{uT} d\varepsilon_j \, \left[g(\varepsilon_j) \int d^d\vec{r}\, d\varepsilon_i \, g(\varepsilon_i) \Theta(u - u_{ij}) \right]}{\int_{-uT}^{uT} d\varepsilon \, g(\varepsilon)} \,. \tag{2.15}$$

Keeping the density of states g constant, this yields

$$B(u) = \beta_d \left(\frac{u}{u_M} \right)^{d+1} \,, \tag{2.16}$$

where $\beta_d = 1/2$ for 1D, $\pi/8$ for 2D, and $\pi/20$ for 3D and

$$u_M = \sqrt{\frac{2T_0}{T}} \,, \quad T_0 = \frac{1}{ga^d} \,, \tag{2.17}$$

a measure of a typical resistor. Since critical bond density B_c is a number that depends on the dimensionality of the system, Eq. (2.16) shows that the percolating resistance is

$$R_P \propto e^{u_c} \,, \quad u_c = \left(\frac{2T_0 B_c}{T \beta_d} \right)^{\frac{1}{d+1}} \,. \tag{2.18}$$

As was explained ealier, it is the percolating network that gives the main contribution to the conductivity of the system. Therefore, the resistance is expected to exhibit the stretched-exponential dependence on temperature. This behavior is the celebrated Mott law.

2.2 Hopping in One Dimension

2.2.1 The Basics

Following the discussion from Sec. 2.1, it might seem that we are on rather solid footing when it comes to understanding hopping transport. While it is true that Mott law is extremely useful for describing the conductivity of disordered systems, it does not provide a complete picture. The first issue that we will adress is its potential inapplicability to 1D systems.

It is well known that low-temperature transport in disordered 1D structures is distinguished by large mesoscopic fluctuations. Such fluctuations have been

measured [29, 98, 47, 3, 31] even in samples of considerable length. They arise from the interplay of localization and rigid geometrical constraints on possible current paths. The total resistance tends to be dominated by a few strong obstacles — "breaks" — which occur at random due to disorder in the sample. [45, 17, 84, 50, 83, 77] These breaks are the regions in energy-position space that contain no LS. In order for the current to go through, charge carriers are forced to perform long hops, which increases the resistance via the tunneling term $\exp[2x_{ij}/a]$. This unusual behavior can be contrasted with a more familiar case of dimensions $d > 1$. There, the current can go around the breaks, so that the mesoscopic fluctuations of transport properties are usually small and self-averaging.

The basis of Mott law lies in the percolation theory. It is known that there is no percolation threshold for 1D systems and this might render Mott law completely irrelevant for $d = 1$. However, the presence of energy dimension complicates the problem. While it is true that energy takes the dimensionality of the system to $d + 1$, the energy dimension is not equivalent to the physical dimension: links farther from Fermi level have higher resistance. For this reason, Mott law in 1D is rather special and we investigate its onset.

In this study, we consider 1D systems that are not too short, so that the coherent tunneling of electrons through their entire length [8, 91] is extremely improbable. Instead, electrons traverse each sample via VRH. By studying the VRH transport [87] one aims to extract information about the nature of electron localization and disorder in the system. However, this task is far from trivial. Despite the seemingly simple expressions defining VRH in 1D, experimental studies of the hopping are typically done in a narrow parameter range where usual theoretical approximations are still rather crude. Here, we demonstrate that large corrections appear when the transport properties of a standard VRH model are calculated numerically, which means, with fewer approximations.

Since one cannot rely on Mott law for accurate description of conductivity in 1D systems, the next best option would be to obtain an ensemble-averaged current-voltage characteristic curve. This curve would certainly depend on the temperature and the localization length, among other parameters. Our task is to

determine the functional dependence of conductivity on these various parameters.

2.2.2 Optimal Path Algorithm

When trying to solve a transpont problem, one approach is to utilize current conservation (the so-called Master eqution),

$$\sum_j I_{ij} = 0, \tag{2.19}$$

supplemented by suitable boundary conditions at the source and drain electrodes with the current I_{ij} given by Eq. (2.1). Unfortunately, these equations are nonlinear and involve an exponentially large spread of the values of the filling factor f_i, which makes the solution difficult to obtain. It can be done numerically, using some clever iterative techniques [52, 104, 59], however, the rate of convergence is slow. We proceed in a different direction, which enables us to map the problem to a resistor network even in the non-Ohmic regime. As a result, we can achieve practically the same speed of simulations in the non-Ohmic regime as in the Ohmic one.

As was already mentioned before, the conductance of a Miller-Abrahams resistor network is dominated by an optimal subnetwork with all other components giving subleading contributions. In 1D, this approximation means that the current does not branch, i.e., $I_{ij} = I$ in each link of the path.

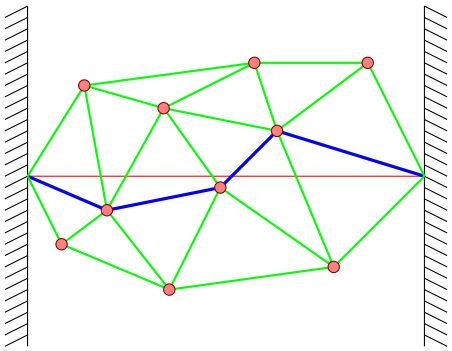

Figure 2.3: An optimal path through the Miller-Abrahams resistor network (blue). Red circles are localized states, green lines are other existing links, and the red line is Fermi level.

In an experimental situation, one would typically apply a voltage across a system and measure the current that flows in response to it. By varying the voltage, one obtains the I-V curve for the system. Here, we approach the problem from the opposite direction. Since the current does not branch as it flows through the sample, the total voltage drop V across the sample is the sum of voltage drops $\eta_i - \eta_j$ on the links. One can determine the optimal path by finding the sequence of the sites that gives the smallest V for a given I.

To facilitate the analysis, let us first define auxiliary variables

$$u_I \equiv \ln\left(\frac{TG_0}{I}\right) \tag{2.20}$$

and

$$S \equiv \frac{T}{|\Delta\varepsilon|}\exp\left(\frac{2x_{ij}}{a}\right)\cosh\left(\frac{\varepsilon_i-\eta_i}{2T}\right)\sinh\left|\frac{\varepsilon_i-\varepsilon_j}{2T}\right| \equiv Qe^{u_I}\cosh\left(\frac{\varepsilon_i-\eta_i}{2T}\right). \tag{2.21}$$

Combining Eqs. (2.20) and (2.21) with Eq. (2.9) results in

$$e^{-u_I} = \frac{\sinh\left(\frac{\eta_i-\eta_j}{2T}\right)}{S\cosh\left(\frac{\varepsilon_j-\eta_j}{2T}\right)}, \tag{2.22}$$

which can be solved for η_j:

$$\eta_j = T\ln\left(\frac{e^{\eta_i/2T} - Se^{-u_I+\varepsilon_j/2T}}{e^{-\eta_i/2T} + Se^{-u_I-\varepsilon_j/2T}}\right). \tag{2.23}$$

Note that the numerator of Eq. (2.23) must be positive so that the voltage difference is a real number. This sets a limit on the maximum current that can flow between sites i and j.

Unlike the internal hops, transitions between the source electrode and the first site inside the sample (as well as the last site and the drain) do not require phonons. This is due to the fact that the electrodes are metallic, which means that they possess a continuum of energy levels. We can account for this by using

$$S_c = \frac{2G_0}{G_c}\exp\left(\frac{2x_{ij}}{a}\right)\cosh\left(\frac{\varepsilon-\eta_i}{2T}\right) \tag{2.24}$$

in lieu of S. Here G_c is determined by the tunneling transparency of the contact between the sample and the electrode. We choose a representative value $G_c = 4G_0$.

Now that we can relate the voltage different between the sites to the site parameters, as well as the drawn current, it is possible to use the above equations to find the optimal path through the sample. To do so we use the well-known Dijkstra's algorithm [24] to calculate the minimum "cost" of getting from the source to the drain.

Dijkstra's Algrithm

We take a brief detour to describe the basis of Dijkstra algorithm. This algorithm was proposed by Edsger Dijkstra in 1956. It is a graph search algorithm designed to find the shortest path between two nodes of the graph given non-negative edge path costs.

The problem is initialized by computing a cost matrix of dimension $N \times N$, where N is the number of nodes on the graph. Each matrix element M_{ij} is the cost of moving from node i to node j. In addition, three arrays of length N are created. We label them as Cost (C), Parent (P), and Visited (V). The Cost array contains the cost of reaching each of the N nodes. The Visited array keeps track of the nodes that have been visited. Finally, the Parent array is used to reconstruct the lowest-cost path.

Here, we assume that we start at the node $i = 1$. In the beginning, all elements in the C array are set to infinity, except the first one, which is set to zero. All the elements in the P array are also set to zero, as are the elements in the V array.

At the start, we pick the node with the lowest Cost entry. Of course, it is site $i = 1$, since all other Cost elements are infinite. We mark $i = 1$ node as "visited" (Visited(1) = 1), which means it will not be reached by any other path again. Next, we proceed to recompute the Cost array for all other sites:

$$\mathrm{C}(j) = \mathrm{C}(1) + M_{1j}\,. \tag{2.25}$$

If this newly-computed C(j) is smaller than the original C(j), we replace the old value with the new one. In addition, we change the Parent entry

$$\mathrm{P}(j) = 1\,. \tag{2.26}$$

This concludes the first iteration of the algorithm. During the following iterations, we again pick out the yet-unvisited node with the lowest Cost and mark it at visited and update the Cost of all other nodes:

$$i = \text{index}\left\{\min\left[\mathrm{C}\left(\mathrm{V}=0\right)\right]\right\}\,, \tag{2.27}$$

$$\mathrm{V}(i) = 1\,, \tag{2.28}$$

$$\mathrm{C}(j) = \min\left[\mathrm{C}(j)\,, \mathrm{C}(i) + M_{ij}\right]\,, \tag{2.29}$$

$$\text{if } \mathrm{C}(i) + M_{ij} < \mathrm{C}(j)$$

$$\mathrm{P}(j) = i\,. \tag{2.30}$$

The algorithm runs until i is the index of the final node at which point the iteration ceases. The next step is to reconstruct the path iteratively in reverse order. Denoting the final node by index f, we have

$$\text{Path} = \left[\mathrm{P}(f);\, \mathrm{P}\left(\mathrm{P}(f)\right);\, \mathrm{P}\left(\mathrm{P}\left(\mathrm{P}(f)\right)\right) \ldots 1\right]\,. \tag{2.31}$$

Finally, it is also possible to obtain the array of costs that contributed to the final path:

$$\text{Costs}(i) = M_{\text{Path}(i+1),\,\text{Path}(i)}\,. \tag{2.32}$$

Using the Costs array, one can obtain the distribution of the costs of the links that participate in connecting the initial and final nodes.

Dijskra's Algorithm for Hopping

As we have already discussed, our primary problem is finding the optimal path that connects the source and drain electrodes. In the Ohmic regime, where the system can be represented by a network of resistors, we are free to use the original form of Dijkstra's algorithm. Actually, the shortest-path algorithm has already been used in the Ohmic VRH problem [37]. Here, each node corresponds to a LS and the cost is the resistance between two LS.

The problems appear when we try to tackle the non-Ohmic case. There, the resistance is a non-linear function of voltage and this prevents us from using the Miller-Abrahams network. All is not lost, however. Instead of trying to minimize

the total resistance of the path, we will instead try to minimize the total voltage V that is required to drive a current I. Thus, the cost c_i of getting to site i on the optimal path is

$$c_i = -\eta_i \,. \tag{2.33}$$

There is, however, one issue still. Typically, evaluation of the cost matrix is the first thing that one does when using Dijkstra's algorithm. Unfortunately, according to Eq. (2.23), the cost of reaching node j is a function of the cost of the earlier sites in the path. This means that one has to recompute the cost matrix at every iteration. Other than this minor issue, which results basically in a slower performance of the algorithm, the rule for updating the costs is unchanged:

$$c_j^{(n+1)} = \min\left(c_i^{(n)} + \delta\eta, c_j^{(n)}\right) \,. \tag{2.34}$$

Here, $c_i^{(n)}$ is the cost of site i at n th iteration. The cost increment $\delta\eta = \eta_i - \eta_j$ is computed using Eq. (2.23). The process terminates when the drain electrode is reached.

There one final, but extremely important point that we still need to discuss. In the non-Ohmic regime, we are using Dijkstra's algorithm in an unconventional fashion where the cost $\delta\eta = \delta\eta(c_i)$ depends non-linearly on the cost of reaching the previous node. For a fixed cost matrix, it is guaranteed that the algorithm finds a globally-optimal path. However, it would appear that we are running a risk of finding a local optimum that will prevent us from obtaining the true best path. That is, in the course of iterations we retain only the lowest cost so far. We effectively assume that for any i and j

$$\min(c_j) = \min(c_i + \delta\eta(c_i)) = \min(c_i) + \delta\eta(\min(c_i)) \,. \tag{2.35}$$

Let us show that this equation is satisfied, which implies that our algorithm works correctly even for the non-constant cost matrix. First of all, by our earlier assumption the current does not branch, and so the current through any link of the optimal path must be exactly I. Second, a sufficient condition for validity of Eq. (2.35) is $\partial c_j/\partial c_i \geq 0$. That is, increasing c_i by taking a less optimal path to the i th site would not help to decrease c_j. In view of Eq. (2.33), the last condition

can be written as

$$\frac{\partial c_j}{\partial c_i} = T\frac{\partial}{\partial c_i}\ln\left(\frac{e^{c_i/2T} + Q\cosh\left(\frac{\varepsilon_i+c_i}{2T}\right)e^{-\varepsilon_j/2T}}{e^{-c_i/2T} - Q\cosh\left(\frac{\varepsilon_i+c_i}{2T}\right)e^{\varepsilon_j/2T}}\right). \tag{2.36}$$

Taking the derivative yields

$$\frac{1}{2}\left[\frac{e^{c_i/2T} + Q\sinh\left(\frac{\varepsilon_i+c_i}{2T}\right)e^{-\varepsilon_j/2T}}{e^{c_i/2T} + Q\cosh\left(\frac{\varepsilon_i+c_i}{2T}\right)e^{-\varepsilon_j/2T}} + \frac{e^{-c_i/2T} + Q\sinh\left(\frac{\varepsilon_i+c_i}{2T}\right)e^{\varepsilon_j/2T}}{e^{-c_i/2T} - Q\cosh\left(\frac{\varepsilon_i+c_i}{2T}\right)e^{\varepsilon_j/2T}}\right]. \tag{2.37}$$

Both denominators have to be positive: the left one is composed only of positive terms and the right one must be positive so that the logarithm in Eq. (2.36) is real. Therefore, the only way that the derivative could be potentially negative is if Q is large enough and the hyperbolic sine in the numerator is negative. We now show that this actually never happens. From Eq. (2.36), it is clear that

$$Q < \frac{e^{-c_i/2T}}{\cosh\left(\frac{\varepsilon_i+c_i}{2T}\right)e^{\varepsilon_j/2T}} \equiv A\,. \tag{2.38}$$

Plugging in $Q = A + \zeta$ into the derivative expression and linearizing with respect to $\zeta < 0$, one gets

$$\frac{e^{-(\varepsilon_i+\varepsilon_j)/2T}}{8\zeta}\left(-\sum_{n=i,j}\frac{4^{\delta_{n,i}}\zeta^{2\delta_{n,j}}e^{\frac{\varepsilon_n}{T}}}{\cosh^2\left(\frac{c_i+\varepsilon_n}{2T}\right)} + \frac{2\zeta e^{\frac{\varepsilon_j}{T}}}{\cosh\left(\frac{c_i+\varepsilon_i}{2T}\right)\cosh\left(\frac{c_i+\varepsilon_j}{2T}\right)}\right) > 0\,, \tag{2.39}$$

as required.

In this section, we have successfully demonstrated that it is possible to use a modified Dijkstra's algorithm in order to find the optimal, non-branching path through a disordered 1D system. Not only are we able to obtain the total resistance/voltage cost for the total path, but we also can get this information for individual links in the path. This will be very useful later in our discussion. For now, however, we spend some time building up the analytical formalism of the problem at hand.

2.2.3 Analytic Approach

It is possible to use our newly-developed optimal path algorithm to obtain the distribution of resistances of individual links belonging to the optimal path. First, however, we determine the form of this distribution using analytical arguments.

Ohmic Regime

We start by discussing the Ohmic case: $u_I \to \infty$. According to previous theoretical studies, notably Refs. [50], [83], and [77], the logarithm of the average resistance of a link is on the order of the Mott value u_M, see Eq. (2.17). While links with $u \gg u_M$ are exponentially rare, they act as bottlenecks and the total resistance depends on them. In order for such high-resistance links to exist, the optimal path has to encounter regions in the energy-position (x-ε) space that are empty of LS.

In the Ohmic regime, the resistance between individual LS is given by Eq. (2.11). To guarantee the presence of a link with resistance u of greater, one needs to ensure that a certain region in the energy-position space, referred to as a "break", contains no LS. From Eq. (2.11), on can determine that a break of resistance u is diamond-shaped with diagonals $2uT$ and $ua/2$ and is centered around Fermi level, see Fig. 2.4.

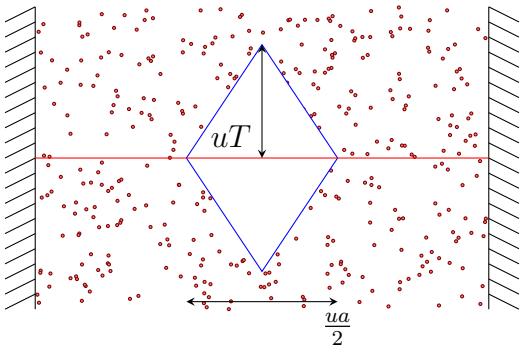

Figure 2.4: An Ohmic break in energy-position space. The blue lines bound the break, the red line is the Fermi level, and the red dots are LS.

Any hop across such a void will have the resistance of at least u. Actually, the horizontal diagonal can be moved by up to $ua/4$ left or right without changing the resistance of the break. This, of course, does not change the area of the void, given by

$$A = \frac{u^2 T a}{2}\,. \tag{2.40}$$

For a constant density of states g, the probability of the break formation

with resistance u or smaller can be given by

$$\mathrm{CDF}(u) = 1 - e^{-gA(u)} = 1 - \exp\left(-\frac{u^2}{u_M^2}\right), \tag{2.41}$$

in accordance with the Poisson distribution. Here, CDF stands for Cumulative Distribution Function. To get the PDF (Probability Distribution Function), we differentiate the CDF to get

$$P(u) = -\frac{d}{du}\exp[-gA(u)], \tag{2.42}$$

where $A(u)$ is the smallest possible area of a break with given u in the x-ε space. This formula was initially proposed by the authors of Ref. [77].

Of course, it is clear that the voids will never be perfect diamonds. Due to the discreteness of the LS, if one were to draw a contour connecting the LS nearest to the blue line in Fig. 2.4, the resulting shape would be far from a diamond. Therefore, as a method of refining $P(u)$ by taking into account the shape fluctuations of the break along its perimeter, Ruzin [80] proposed a refined formula

$$P(u) = C_0 \exp(2Bu/u_M) \times gA'(u)\exp[-gA(u)]. \tag{2.43}$$

While C_0 is determined essentially by the normalization of P, analytical calculation of the coefficient B is challenging. Ruzin gave a rough estimate $B \approx \sqrt{2}/3 \approx 0.5$. In this study, we calculate B numerically.

Non-Ohmic Regime

Determining the shape of the optimal break in the non-Ohmic regime is a bit more difficult due to the nonlinearity of the problem. Nonetheless, it is possible to do so, following the approach given in Ref. [26]. The first assumption that we make is that the temperature of the system is low. By that we mean that it is lower than other energies involved in the current expression, Eq. (2.9). This allows us to approximate the expression for the current as

$$I = \frac{2T}{R_0}\sinh\left(\frac{\delta\eta}{2T}\right)\exp\left(-\frac{2x_{ij}}{a} - \frac{|\varepsilon_i - \eta_i|}{2T} - \frac{|\varepsilon_j - \eta_j|}{2T} - \frac{|\varepsilon_i - \varepsilon_j|}{2T}\right), \tag{2.44}$$

where R_0 is a constant. In this simplified formula, we have gotten rid of the $|\Delta\varepsilon|$ prefactor since it has a subleading contribution compared to the exponential term. To determine the shape of the break, we define

$$u_{ij} = \ln \frac{R_{ij}}{R_0} = u_I + \ln \frac{\delta\eta}{T}\,, \quad u_I = \ln\left(\frac{T}{R_0 I}\right)\,, \quad \beta = \frac{\delta\eta}{T} = e^{u-u_I}\,. \tag{2.45}$$

First,

$$\begin{aligned} u_I &= -\ln 2 - \ln\left[\sinh\frac{\beta}{2}\right] + \frac{2x}{a} + \frac{|\varepsilon_i-\eta_i| + |\varepsilon_j-\eta_j| + |\varepsilon_i-\varepsilon_j|}{2T} \\ &= \frac{2x}{a} - \ln\left[e^{\beta/2} - e^{-\beta/2}\right] + \frac{|\varepsilon_i-\eta_i| + |\varepsilon_j-\eta_j| + |\varepsilon_i-\varepsilon_j|}{2T} \\ &= \frac{2x}{a} - \ln\left[1 - e^{-\beta}\right] + \frac{|\varepsilon_i-\eta_i| + |\varepsilon_j-\eta_j| + |\varepsilon_i-\varepsilon_j| - \beta T}{2T}\,. \end{aligned} \tag{2.46}$$

Using the fact that $\eta_j = \eta_i - \beta T$ and measuring all the energies from η_i, we write

$$u_I = \frac{2x}{a} - \ln\left[1 - e^{-\beta}\right] + \frac{|\varepsilon_i| + |\varepsilon_j + \beta T| + |\varepsilon_i - \varepsilon_j| - \beta T}{2T}\,. \tag{2.47}$$

The width of the break is maximum when $\varepsilon_i = 0$, which yields

$$x = \frac{a}{2}\left[w - \frac{|\varepsilon_j + \beta T| + |\varepsilon_j| - \beta T}{2T}\right]\,, \tag{2.48}$$

where $w = u_I + \ln\left(1 - e^{-\beta}\right)$.

From Eq. (2.48), we can determine the shape of the non-Ohmic break. Unlike the Ohmic break which is a (deformable) diamond, the non-Ohmic break has a hexagonal shape, see Fig. 2.5. The combination βT, which is equal to the electrochemical potential drop across the break, gives the the height of the middle part of the break in the x-ε space. Similarly to the Ohmic case, the central rectangular region can be moved left or right up to $wa/4$. To check for consistency, we allow $u_I \to \infty$, $\beta \to 0$:

$$w = u_I + \ln\left(1 - e^{-\beta}\right) \approx u_I + \ln\beta = u\,, \tag{2.49}$$

as expected. Thus, as the current flowing through the system goes to zero, we return to the Ohmic regime.

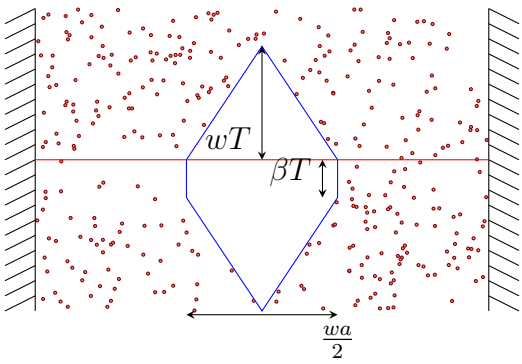

Figure 2.5: A non-Ohmic break. The red line is the electrochemical of the initial site i.

To get the area of the break, we integrate along ε_j:

$$\begin{aligned} gA &= g\int x(\varepsilon_j)\,\Theta\left[x(\varepsilon_j)\right]d\varepsilon_j \\ &= \frac{ga}{2}\left\{\int_0^{wT} w-\frac{\varepsilon_j}{T}d\varepsilon_j+\int_{-\beta T}^{0} w\,d\varepsilon_j+\int_{-wT-\beta T}^{-\beta T} w+\frac{\varepsilon_j+\beta T}{T}d\varepsilon_j\right\} \\ &= \frac{gTa}{2}\left\{w\left(2w+\beta\right)-\frac{w^2}{2}+w\beta+\frac{\beta^2}{2}-\frac{(w+\beta)^2}{2}\right\}=\frac{w^2+\beta w}{u_M^2}\,. \end{aligned} \tag{2.50}$$

In order to account for the possible perimeter corrections to $P(u)$, we consider the following trial form:

$$P(u)=C_0\exp\left[2B\frac{w}{u_M}+C\left(\frac{\beta}{u_M}\right)^D\right]\times gA'(u)\exp\left[-gA(u)\right]\,. \tag{2.51}$$

Here the contribution of the top and bottom parts of the perimeter is modeled after Eq. (2.43). It is proportional to the length of such parts $\sim w$ and the coefficient B. The contribution of the side walls of the break, of length βT, is written differently. Indeed, Ruzin's argument [80] suggests that they give no contribution at all. In fact, we found it necessary to include a correction albeit with a smaller exponent $D=0.5$. We have no other justification for this exponent except that it provides a good fit to the numerical $P(u)$, see below. Equation (2.51) applies for $u-u_I\gg 1$ and $u_I\gg u_M$. It refines the corresponding expression for $P(u)$ in Ref. [26] where the first (subleading) exponential term was not included. The Ohmic and non-Ohmic formulas, Eqs. (2.43) and (2.51), match at $u-u_I\sim 1$.

2.2.4 Link Resistance Distribution

Having established the basic formalism for the probability distribution of the link resistances in an optimal path, we now move to numerical methods to both check our predictions and determine the coefficients.

In order to conduct our simulations, we generate a number of LS in the x-ε space and then use the modified Dijkstra's algorithm to find the optimal path through the system and obtain the link resistances. Repeating this process for a large number of systems allows us to build the probability distribution of u, $P(u)$.

For each disorder realization, the LS are positioned randomly within the allotted area in x-ε space. The number of the LS is determined by multiplying the area by the density of states. Here is how we determine the energy range to be included in the simulations. Recall that in the Ohmic approximation the resistance between two LS is given by Eq. (2.11). This means that the tunneling resistance is $u_T = 2L/a$, where L is the length of the system. The height of such an Ohmic break would then be $u_T T$, see Fig. 2.4. This means that the optimal path would never go through energies above $u_T T$ and below $-u_T T$ as it would be more favorable to simply tunnel through the entire length of the sample. In the non-Ohmic regime, on the other hand, one needs to extend the range of the negative energies. It is clear from Eq. (2.23) that the path cascades down the energy coordinate, trying to keep the energy of the LS close to the local η.

At each L, the functional form of the $P(u)$ is expected to depend only on the dimensional ratio u/u_M. By running simulations at different combinations of a, g, and T, we convinced ourselves that this is indeed correct, for the exception of very small u where the discreteness of the system starts to matter. Fortunately, such u are irrelevant for the macroscopic transport properties as they do not determine the resistance. Thereafter we fixed $a = 4$, $g = 1/3$, and $T = 0.01$, which yields the characteristic temperature $T_0 = 3/4$ and the Mott parameter $u_M = 12.247$, cf. Eq. (2.17).

Ohmic Regime

To ensure we are in the Ohmic regime $u_I = 200 \gg u_M$ was used. The simulations were conducted for several different values of L: $L = 100, 200, 400, 500,$ and 1000. For each L in the set we generated many realizations of 1D wires, respectively, 20000, 10000, 5000, 4000, and 2000. We found optimal paths through the samples and created the PDFs of the link resistances, following the process described earlier. Finally, we fitted such PDFs to Eq. (2.43) using B as a single adjustable parameter. The quality of the fits was rather good, see an example in Fig. 2.6. Furthermore, even though Eq. (2.43) is meant to apply at $u \gg u_M$, it fits our numerical results for $u \lesssim u_M$ as well.

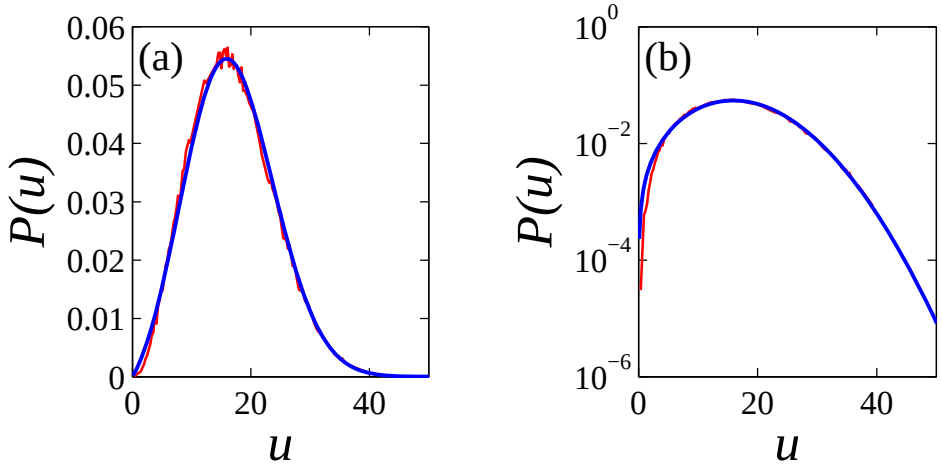

Figure 2.6: Numerical results for $P(u)$ in the Ohmic regime shown on (a) linear and (b) logarithmic scale. The small fluctuations are of statistical origin. Equation (2.43) with $B = 0.9$ is represented by the smooth thick line.

Interestingly, we found that B slowly but systematically increases with L. Larger B means that the formation of highly resistive links becomes easier. When plotted as a function of $1/L$, it was seen to vary linearly, tending to a constant for large L. The reason for this observed behavior has to do with the electrodes. As was mentioned earlier, electrodes are metallic and, therefore, contain states at all energies. Due to this, the hops from and to the electrodes are typically less resistive than those inside the system. In shorter samples, where the total number of hops through the sample N_u is about ten or so [see Eq. (2.56) below], these

"easy" hops impact the PDF. As the samples get longer, N_u increases and these two hops do not influence the overall PDF any more. To get the value of coefficient B in the thermodynamic limit, we used linear extrapolation to $L = \infty$. Our final estimate is

$$B = 0.92 \pm 0.02\,, \tag{2.52}$$

approximately twice larger than that of Ref. [80].

Two characteristic measures of the width of the distribution are its mode and its average. For $P(u)$ they are given by, respectively,

$$u_{\max} = \frac{1}{2}\left(B + \sqrt{B^2+2}\right)\, u_M = (1.30 \pm 0.02)\, u_M\,, \tag{2.53}$$

$$\langle u \rangle = \int_0^\infty u P(u) du = (1.39 \pm 0.02)\, u_M\,. \tag{2.54}$$

As expected, both are the order of the Mott parameter u_M. One more important quantity is the average number N_u of links on the path. It determines the relation between $P(u)$ and the probability density of breaks per unit length of the wire $\rho(u)$:

$$\rho(u) = \frac{N_u}{L}\, P(u)\,. \tag{2.55}$$

Since the width of each link is not smaller than $(a/2)u$, cf. Eq. (2.44), N_u can be estimated from below as $(2L/a)/\langle u \rangle \approx 1.4 L/a u_M$. According to our simulations, the actual N_u is approximately twice larger:

$$N_u = (3.04 \pm 0.07)\, \frac{L}{u_M a}\,. \tag{2.56}$$

Besides RR [77] and Ruzin [80], the calculation of $P(u)$ was previously attempted by Ladieu and Bouchaud. [46] They reported $u_{\max}$ and $\langle u \rangle$ that differ from our Eqs. (2.53) and (2.54) by 30-40% In fact, we were unable to verify that statement because the main equation of Ref. [46] has no solution. As written, that equation does not conserve probabilty. Consequently, we believe that our results constitute the first reliable calculation of function $P(u)$.

Non-Ohmic Regime

Let us now move on to the non-Ohmic regime. Before discussing the simulation results, we devote a bit of time to talking about the optimal path in this

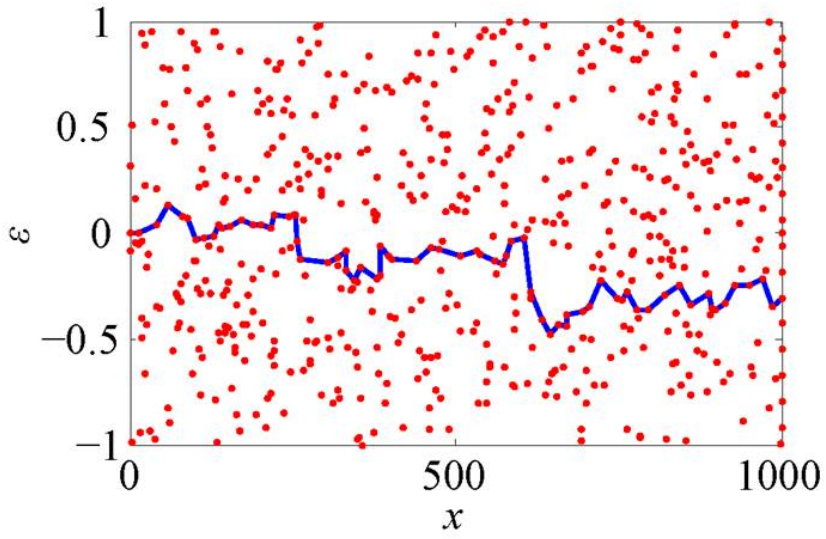

Figure 2.7: An example of the optimal path in a modestly non-Ohmic regime, $u_I = 25$. The dots represent localized states.

regime. In particular, we want to know how the path in a given sample changes with increasing current. As was established earlier, the optimal path is the sequence of hops that requires the minimum applied voltage to conduct a set current.

Consider an optimal path that was found for a collection of LS at some current u_I. Using Eq. (2.9), for any two LS that belong to the path, we write

$$R_{ij} \propto e^{u_I}(\eta_i - \eta_j) \propto (\eta_i - \eta_j)\, \frac{\cosh\left(\frac{\varepsilon_j - \eta_j}{2T}\right) \cosh\left(\frac{\varepsilon_i - \eta_i}{2T}\right) \sinh\left|\frac{\Delta\varepsilon}{2T}\right|}{\sinh\left(\frac{\eta_i - \eta_j}{2T}\right)} \,. \tag{2.57}$$

If the difference $\eta_i - \eta_j$ is small, the hyperbolic sine can be expanded and the resulting R_{ij} behaves as an Ohmic resistor where the resistance does not depend on the voltage. This is true for the "easy" hops, where the cost of hopping is low, giving small $\delta\eta$. Therefore, to observe non-Ohmic behavior, we turn our attention to the "difficult" hops—the hops that require significant voltage drops.

Typically, $\varepsilon_j < \varepsilon_i$:

$$\exp\left[-u_I\right] \propto \exp\left[\tilde{\eta}_i - \tilde{\eta}_j - |\tilde{\varepsilon}_i - \tilde{\eta}_i| - |\tilde{\varepsilon}_j - \tilde{\eta}_j| - |\Delta\tilde{\varepsilon}|\right] , \tag{2.58}$$

where we have expressed all quantities in units of $2T$. Setting $\tilde{\eta}_i = \tilde{\varepsilon}_i + \tilde{a}_i$, one obtains

$$\exp\left[-u_I\right] \propto \exp\left[\tilde{a}_i - \tilde{a}_j - |\tilde{a}_i| - |\tilde{a}_j|\right] . \tag{2.59}$$

In the expression above, a_i and a_j can be either greater or less than zero. This results in the following four combinations:

$$\tilde{a}_i > 0,\, \tilde{a}_j > 0 \quad \exp\left[-u_I\right] \propto \exp\left[-2\tilde{a}_j\right] , \tag{2.60}$$

$$\tilde{a}_i > 0,\, \tilde{a}_j < 0 \quad \exp\left[-u_I\right] \propto 1 , \tag{2.61}$$

$$\tilde{a}_i < 0,\, \tilde{a}_j > 0 \quad \exp\left[-u_I\right] \propto \exp\left[2\tilde{a}_i - 2\tilde{a}_j\right] , \tag{2.62}$$

$$\tilde{a}_i < 0,\, \tilde{a}_j < 0 \quad \exp\left[-u_I\right] \propto \exp\left[2\tilde{a}_i\right] . \tag{2.63}$$

A way to visualize the above situations is to keep in mind that positive $\tilde{a}_i$ means that the local electrochemical potential is above the energy of the LS. This means that the LS is typically occupied. On the other hand, negative $\tilde{a}_i$ means that the local η_i is below ε_i and the LS is generally empty.

From the expressions, one can see that for four pairs of LS given the same $\Delta\varepsilon$ and separation x, the maximum current is obtained when $\tilde{a}_i > 0$ and $\tilde{a}_j < 0$. This, of course, makes sense as it is preferred that the initial LS is full and the final one is empty. The worst case, on the other hand, is if the signs of $\tilde{a}$ are switched.

As one tries to increase the current through the system, all the η_i (and, therefore, $\tilde{a}_i$) on the optimal path become more negative, see Eq. (2.23). If before the attempted current increase the pair is described by either Eq. (2.61) or (2.63), application of additional voltage does not increase the current flow. Moreover, in the second case, decreasing $\tilde{a}_i$ actually suppresses the current. These two configurations will be referred to as "hard" pairs. They are similar to reverse-biased diodes where additional voltage application does not increase the current. Since this given can no longer support the required current, the optimal path will change, going to lower energies to avoid these hard pairs.

If, on the other hand, the pair is initially in the other two situations, additional voltage can increase the current flow. For both of these situations, increases exponentially with additional voltage application. We refer to these pairs as "soft" and they are similar to forward-biased diode because of their exponential dependence of current on voltage. These pairs will remain on the optimal path until $\tilde{a}_j$ becomes less than zero, turning the pair into a hard one, which has a maximum current that it can carry, as was described above.

It is possible to drive a number of conclusions from the above discussion, similar to the one found in Ref. [86] . First, within any optimal path, there is a probability of Ohmic pairs. We expect the probability of the formation of the Ohmic links not to vary too much with current since their behavior is current-independent. Indeed, Eq. (2.51) predicts that $P(u)$ transitions to the Ohmic form for $u < u_I$. In addition, hard links are typically avoided as they cannot maintain the required current. It is the hard links that give the highest values of u, therefore, we expect to see a sharp drop in $P(u)$ for large u. Due to probability conservation, the area under the curve has to be 1. Since the Ohmic regime does not change much and high u's are cut out, there is a feature that compensates. We find a narrow peak of width $\delta u \sim \ln(u_M^2/u_I)$ near the non-Ohmic threshold $u = u_I$. This narrow peak is due to the soft links that used to have resistances $u \gtrsim u_I$ in the Ohmic regime. Like for a forward-based diode, when a finite current is made to flow across the wire, such links self-generate $\delta\eta$ large enough to push their resistance back to an immediate vicinity of the non-Ohmic threshold $u \approx u_I$.

For parameters chosen in Fig. 2.8 this peak is so pronounced that it already dwarfs the "Ohmic" maximum at $u = u_{\max}$.

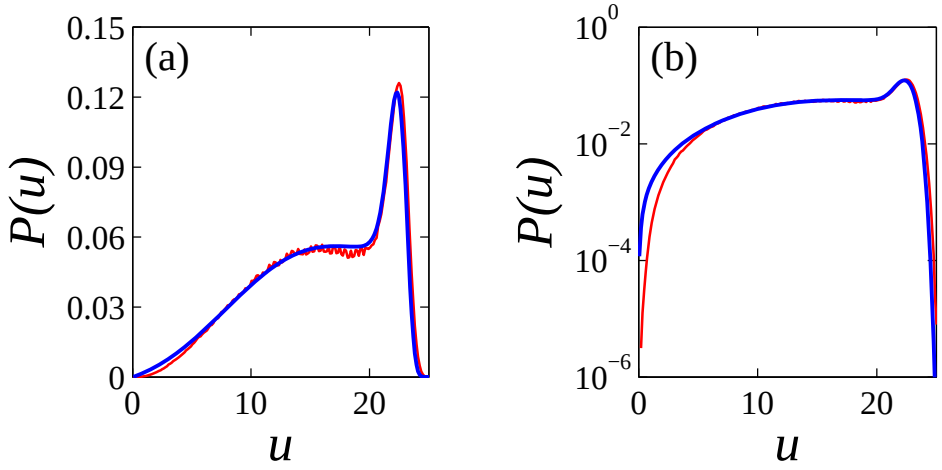

Figure 2.8: Numerical results for $P(u)$ $u_I = 20$ shown on (a) linear and (b) logarithmic scale (thin line). The small fluctuations are of statistical origin. The fitting formula (2.51) with $u_M = 12.247$, $B = 0.9$, $C = 0.75$, and $D = 0.5$ is represented by the thick line.

The simulation procedure in the non-Ohmic regime is identical to the Ohmic

case. The simulation was conducted at $u_I = 35, 30, 25$, and 20. Two values of u_M are used: 12.247 (same as above) and 20 (obtained by adjusting the temperature but keeping $g = 1/3$ the same). The fit of the numerical $P(u)$ to Eq. (2.51) for $u_M = 12.247$ can be seen in Fig. 2.8 and it is quite good at all but very small u (which are irrelevant).

2.2.5 Distribution of the Net Resistance

With the knowledge of $P(u)$, one can obtain the distribution of the net resistance. This quantity is, of course, more important since it is physically observable. The resistance of the system is given by the sum over all links,

$$R = R_0 \sum_{i=1}^{N_u} e^{u_i} \,. \tag{2.64}$$

Certainly, the resistances of the links are not truly uncorrelated; however, since R is dominated by the largest breaks, which are rare and well-separated, this should be a good approximation. To obtain the analytical formula for the total resistance distribution, we use the method of cumulants. A cumulant κ_m is given by

$$\ln \mathcal{G}(k) = \sum_{m=1}^{\infty} \frac{(ik)^m}{m!} \kappa_m \,, \tag{2.65}$$

$$\mathcal{G}(k) = \int dx \, P(x) e^{ikx} \,. \tag{2.66}$$

where $\mathcal{G}(k)$ is the characteristic function of the probability distribution $P(x)$.

First, the total resistance R/R_0 is a stochastic variable, given by

$$\frac{R}{R_0} = \sum_u e^u N(u) \,, \tag{2.67}$$

where $N(u)$ is the number of links of resistance u, itself a random variable. It is described by a Poisson distribution with the average $\bar{N}(u) = L\rho(u)$. Thus, for a given u, the probability that it contributes $e^u N$ to the total resistance is

$$P(e^u N) = \frac{e^{-\bar{N}} \bar{N}^N}{N!} \,. \tag{2.68}$$

Next, we obtain the characteristic function for the variable $e^u N$:

$$\begin{aligned}\mathcal{G}(k) &= \sum_N \frac{e^{-\bar{N}}\bar{N}^N}{N!}\exp\left(ike^u N\right) \\ &= e^{-\bar{N}}\sum_N \frac{\left[\exp\left(ike^u\right)\bar{N}\right]^N}{N!} = \exp\left\{\bar{N}\left[\exp\left(ike^u\right)-1\right]\right\} . \end{aligned} \tag{2.69}$$

From this, one gets the cumulants

$$\ln \mathcal{G}(k) = \sum_{m=1}^{\infty} \frac{(ik)^m}{m!}\underbrace{e^{mu}\bar{N}}_{\kappa_m} . \tag{2.70}$$

The total cumulant is obtained by summing all the cumulants:

$$\kappa_m^T = \int e^{mu}\bar{N}(u)du\,, \tag{2.71}$$

which allows one to reconstruct the total characteristic function

$$\mathcal{G}^T(k) = \exp\left\{\int \bar{N}(u)\left[\exp\left(ike^u\right)-1\right]\right\} . \tag{2.72}$$

Finally, taking its Fourier transform and making the change of variable from R to $U \equiv \ln(R/R_0)$, we recover

$$P_U(U) = \frac{1}{2\pi}\int \exp\left(U - ike^U\right)\mathcal{G}^T(k)dk\,, \tag{2.73}$$

equivalent to the result given by Raikh and Ruzin(RR) in Refs. [76] and [77].

In their work, RR obtained an analytical formula for the PDF $P_U(U)$ in the Ohmic limit without the subleading term:

$$P_U(U) = \sqrt{\nu}\,\exp\left[-\sqrt{\nu}\,\delta U - \exp(-\sqrt{\nu}\,\delta U)\right] , \tag{2.74}$$

$$\delta U \equiv U - \left(\sqrt{\nu}\,T_0/T\right), \tag{2.75}$$

$$\nu = \frac{2T}{T_0}\,\ln\left(\sqrt{\nu}\,\frac{L}{a}\right) . \tag{2.76}$$

This curve is given alongside our result in Fig. 2.9.

Note that in Ref. [46] an attempt was made to include correlations between adjacent links. As mentioned above, it does not compare well with our simulations.

In practice, even a numerical integration of the strongly oscillating functions in Eqs. (2.72) and (2.73) is difficult. We found it easier to directly implement Eq. (2.64) instead. To this end we draw u_i from the distribution $P(u)$

using a Monte-Carlo sampling (the usual acceptance-rejection algorithm). After N_u [Eq. (2.56)] of such resistances are generated, the total resistance of the wire is obtained by summing them. This procedure will be referred to as PDF-algorithm.

We first present our results for the Ohmic case in Fig. 2.9. The simulations are done for system size $L = 10^3$, localization length $a = 4$, and $u_M = 12.247$. This Figure illustrates the importance of the subleading term that was introduced into $P(u)$ in Ref. [80]. Without this term, the resistance for the identical systems is lower by about two orders of magnitude, despite the similar functional form. This means that excluding the subleading correction leads to reduced resistance. In addition, Fig. 2.9 demonstrates that our PDF-algorithm can successfully replicate the results obtained by the shortest-path algorithm. Since PDF-algorithm is considerably faster than the other one, it is preferred in the situations where one needs to analyze a large number of disorder realizations.

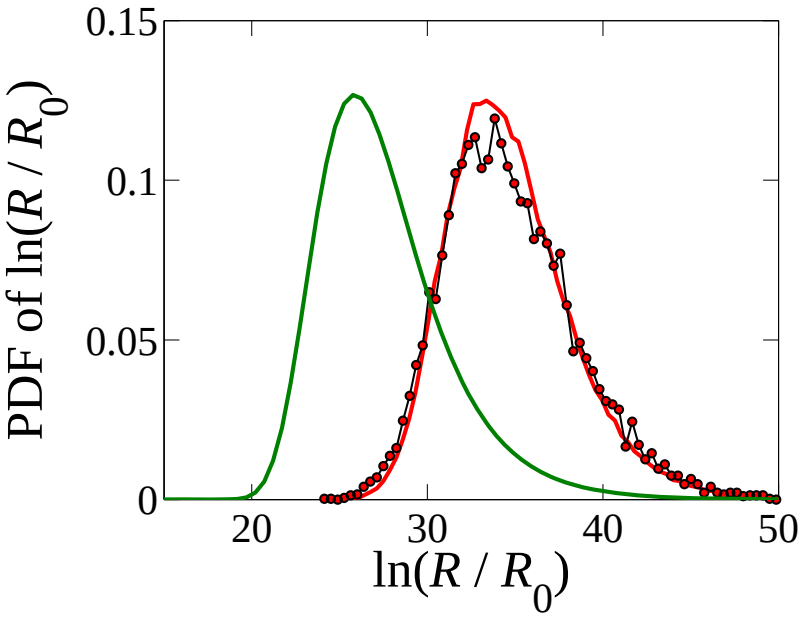

Figure 2.9: The PDF of the logarithm of the total resistance R in the Ohmic limit. The smooth curve on the right is obtained using the PDF algorithm; the markers correspond to the shortest-path simulation. The leftmost curve is obtained using Ref. [77].

Next, we move on to the non-Ohmic case. In Fig. 2.10, we present a se-

quence of four PDF's obtained from our shortest-path and PDF-algorithm simulations. From one curve to the next the current increases by the same factor of exp(5). A qualitative difference from the PDF for the Ohmic case (Fig. 2.9) is immediately apparent. The Ohmic PDF is skewed to the right, towards the large resistances. In contrast, the non-Ohmic curves are skewed the opposite way. This difference is due to the response of $P(u)$ to the rise in current. In both Ohmic and non-Ohmic regimes the net resistance of the system is determined by the largest breaks. However, in the non-Ohmic case there is almost a hard cutoff $\approx u_I$ on the largest possible u (Fig. 2.8). In other words, breaks with $u \gtrsim u_I$ are effectively eliminated, [26] making the large-resistance side of the PDFs of $\ln(R/R_0) \gg u_I$ drop sharply as well.

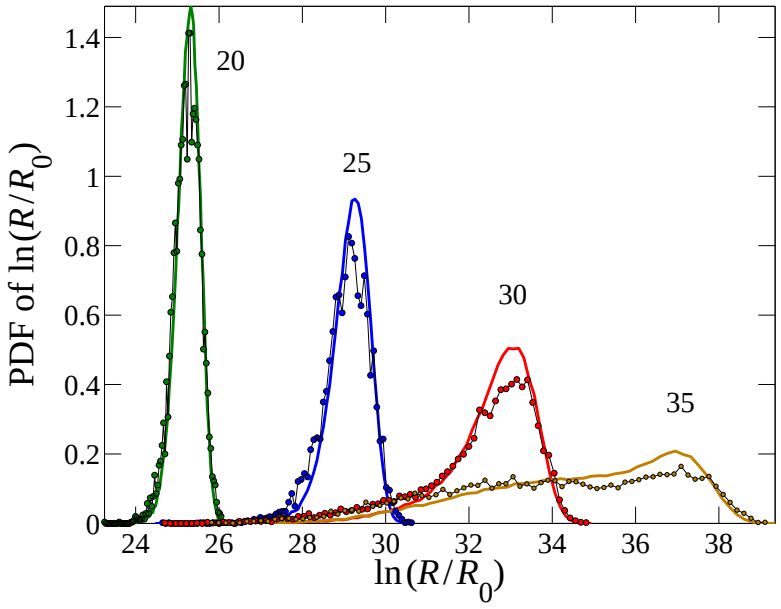

Figure 2.10: The PDF of the logarithm of the total resistance R for different u_I. The simulation parameters are the same as in Fig. 2.9. The smooth curves are obtained using the PDF algorithm, the markers are from the shortest-path simulations.

Another result of removing the highly resistant links is the PDF's approach to the Gaussian shape. By reducing the spread of the link resistances, it brings the system closer to the conditions at which the central-limit theorem is obeyed. This

can be seen in Fig. 2.10, where the curves become narrower and more Gaussian at lower u_I.

Finally, Figure 2.10 illustrates that the PDFs obtained from the shortest-path simulations and from the PDF-algorithm are in a good agreement. The curves produced by the latter are much more smooth because we could apply it to a larger number of disorder realizations: 10^5.

2.2.6 Conductance-Voltage Characteristics

In experiment, macroscopic transport properties are measured either as a function of current or as a function of voltage. In the former case, the ensemble averaging gives the average resistance $\langle R \rangle$; in the latter — the average conductance $\langle G \rangle$. If a large number of nominally identical wires is available simultaneously, this can be done in a single measurement, connecting them, respectively, in series and in parallel. [44] Otherwise, one can try to create the members of an ensemble one by one by varying gate voltage or other parameters of a single wire. [41]

In the non-Ohmic regime, it has been customary [63, 38, 74, 49] to characterize the field-dependence of the conductivity by means of the length parameter L_c:

$$\langle G \rangle (F,T) = \langle G \rangle (0,T) \exp\left(|F| L_c / T \right) . \tag{2.77}$$

In experiment, this law typically describes the first decade of the conductivity rise. Thereafter, deviations tend to occur. Indeed, in theory [86, 52, 90] L_c is expected to be not a constant but a function of F and T.

At large enough F, Eq. (2.77) eventually becomes a poor approximation. Theoretically, it should cross over to [26]

$$G \sim \frac{a}{2LR_0} \exp\left(-\sqrt{\frac{8T_0}{Fa}} \right) . \tag{2.78}$$

(At such fields mesoscopic conductance fluctuations are small, and so we denote $\langle G \rangle$ simply by G.) Note that it can be viewed as the 1D Mott law with the effective temperature [85, 57] $T_{\text{eff}} \sim Fa$ replacing the ambient temperature T.

Figure 2.11 shows the dependence of the average Ohmic conductivity

$$\langle G(0,T)\rangle = G_0 \exp\left[-(\Delta/T)^{\gamma}\right] \tag{2.79}$$

on temperature in an ensemble of samples of length $L = 250a$. To test the expected crossover behavior, we fit the low T data points using Eq. (2.79) with $\gamma = 1/2$, corresponding to the 1D Mott law. We fit higher T using $\gamma = 1$, representing activated transport. In the Mott regime we find $\Delta = 8.4T_0$. For the activated regime we get $\Delta = 0.62T_0$. Note the large difference between these values. As far as Δ is concerned, our numerical results are in a good agreement with the analytical theory of Raikh and Ruzin [77]. In the high-T regime it predicts $\Delta = T_0/2$. Their low-T formula reads

$$G = R_0^{-1} \exp\left(-\sqrt{\nu}\,\frac{T_0}{T}\right) , \tag{2.80}$$

where ν is given by Eq. (2.76).

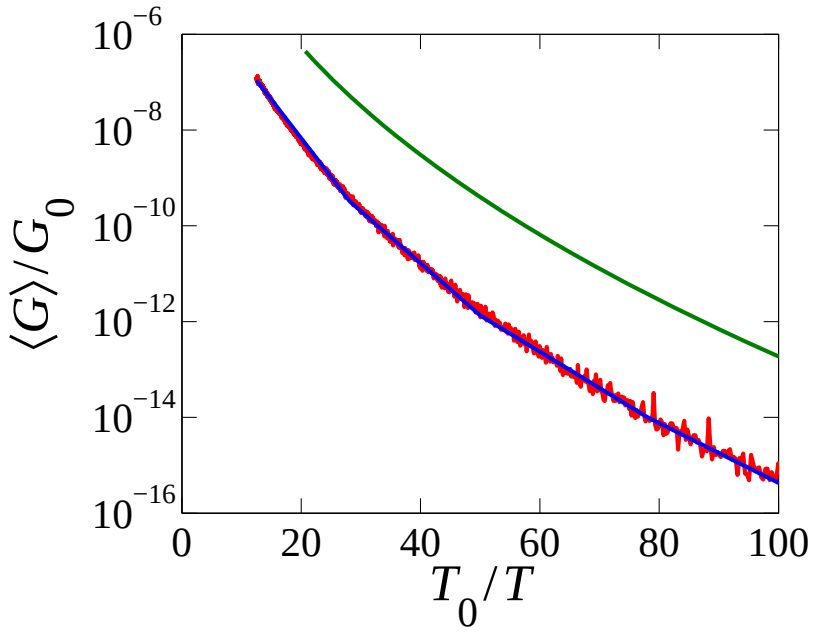

Figure 2.11: $\langle G\rangle$ as a function of T: (a) High T; the dashed line is the best fit for $\gamma = 1$ with $\Delta = 0.62T_0$ in Eq. (2.79). (b) Low T. The dashed line is a fit to the 1D Mott law, $\gamma = 1/2$ and $\Delta = 8.4T_0$ in Eq. (2.79). The upper curve is Eq. (2.80).

Therefore, RR result for Mott's Δ is

$$\Delta(T) = 2T_0 \ln\left(\sqrt{\nu}\,\frac{L}{a}\right) . \tag{2.81}$$

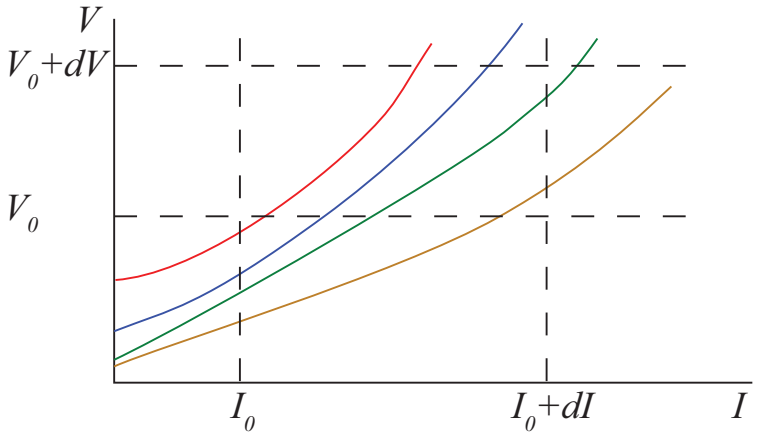

Figure 2.12: A sketch of V–I curves for an array of different wires. The continuity equation (2.83) follows from the conservation of the number of curves piercing the differential area element bounded by the dashed lines.

Strictly speaking, it is not a constant but a slow function of T. In the range of T where the fit to the Mott law was done, it is indeed close to $8.4T_0$. The large difference between the values of Δ in the Mott and the activated regime is due to the "large" logarithm $\ln(\sqrt{\nu}\, L/a)$.

When the RR formula is plotted alongside our numerical results, it is seen to exhibit a very similar shape yet a large difference in the absolute value, see Fig. 2.11(b). Despite the fact that we study exactly the same model, RR's predictions differ from our results by two orders of magnitude. We attribute this discrepancy to the "subleading" terms not included in the asymptotic theory of RR.

Since our shortest-path algorithm is formulated at a constant current (i.e., constant u_I), one may naively think that it is able to provide only the distribution of resistances. This is not so. Let us show that the PDFs of conductances and resistances are uniquely related even in the non-Ohmic regime.

Denote the PDF of having a given total voltage V at a fixed current I by $P_V(V|I)$ and the PDF of having a given current I at a fixed total V by $P_I(I|V)$. By inspecting the monotonically increasing V-I curves sketched in Fig. 2.12, we can write down the following continuity equation:

$$P_V(V_0|I_0)dV + P_I(I_0|V_0)dI = P_V(V_0|I_0+dI)dV + P_I(I_0|V_0+dV)dI\,, \qquad (2.82)$$

which simply states that the flow of the lines into the differential area from the left and the bottom edges equals the outflow through the top and the right boundaries. Expanding the right hand side for dV and dI, one obtains

$$\left[\frac{\partial}{\partial I}P_V(V|I)+\frac{\partial}{\partial V}P_I(I|V)\right]dVdI=0\,. \tag{2.83}$$

Integrating with respect to voltage, we get

$$P_I(I|V)=-\frac{\partial}{\partial I}\int_0^V P_V(V'|I)dV'\,. \tag{2.84}$$

As an application, let us show how the average conductance G_V at a given fixed voltage V,

$$G_V=\int_0^\infty P_I(I|V)\frac{dI}{R}\,,\quad R=\frac{V}{I}\,, \tag{2.85}$$

can be calculated.

In view of Eq. (2.84), the last relation can be written as

$$G_V=-\int_0^\infty \frac{IdI}{V}\frac{\partial}{\partial I}\int_0^V P_V(V'|I)dV'\,. \tag{2.86}$$

Next, we integrate it by parts:

$$G_V=-\left\{\frac{I}{V}\cancelto{0}{\int_0^V P_V(V'|I)dV'\Big|_0^\infty}-\frac{1}{V}\int_0^\infty dI\int_0^V P_V(V'|I)dV'\right\}\,. \tag{2.87}$$

and change the notation for the measure in the second integral from $P_V(V'|I)dV'$ to $P_R(R'|u_I)dR'$. We arrive at the formula

$$\frac{G_V}{R_0^{-1}}=\frac{T}{V}\int_{-\infty}^\infty\frac{du_I}{e^{u_I}}\int_0^\infty\Theta\left(\frac{Ve^{u_I}}{T}-\frac{R'}{R_0}\right)P_R(R'|u_I)dR' \tag{2.88}$$

for the desired average conductance at a fixed voltage. It is easy to see that in the Ohmic limit, $V\to 0$, Eq. (2.88) coincides with the average conductance at a fixed current, $\int P_R(R'|\infty)dR'/R'$, as expected.

To evaluate G_V as a function of V one needs to know $P_R(R'|u_I)$. We obtained it by the following procedure. First, an interval of interest in V is devided into a number of bins. Next, we take an interval of u_I from 5 to about $u_I=3u_M$ and in turn divide it into equidistant steps $u_I(j)$, $1\le j\le N_I=1000$, spaced by

Δu_I. For each $u_I(j)$ we generate $N_{\rm sam} = 200$ samples, i.e., sets of N_u individual u's, drawn from the distribution $P(u)$ using the acceptance-rejection algorithm. Finally, we convert the integrals in Eq. (2.88) into discrete sums,

$$\frac{G_V}{R_0^{-1}} = \frac{\Delta u_I}{V N_{\rm sam}} \sum_{j=1}^{N_I} \frac{T}{e^{u_I(j)}} \sum_{i=1}^{N_{\rm sam}} \Theta\!\left(\frac{V e^{u_I(j)}}{T} - \frac{R_i(j)}{R_0} \right), \tag{2.89}$$

where $R_i(j)$ is the total resistance of i th set for a given j, and then evaluate them numerically.

Alternatively, G_V can be reduced to a numerical quadrature, which this time contains no oscillating integrals. This is possible because G_V is dominated by large conductances, for which the saddle-point approximation in Eq. (2.73) is legitimate. After a straightforward derivation, one obtains

$$\begin{aligned} \frac{G_V}{R_0^{-1}} = \frac{T}{V} \int_{-\infty}^{\infty} \frac{du_I}{e^{u_I}} \int_0^{\infty} \Theta\!\left(\frac{V e^{u_I}}{T} - J_1 \right) \\ \times \sqrt{\frac{J_2}{2\pi}} \, \exp\left(t J_1 + J_0 \right) dt \,, \end{aligned} \tag{2.90}$$

$$J_n = N_u \int_0^{\infty} P(u) \left[\exp(nu - te^u) - \delta_{n,0} \right] du \,, \tag{2.91}$$

where $n = 0, 1, 2$, and δ_{ij} is the Kronecker symbol. All these integrals are rapidly converging, so that their numerical evaluation should cause no difficulty. However, we did not pursue this method.

The simulations were performed for $u_M = 5$, 7.5, 10, 12.5, and 15. The control parameter was T while all other values — a, g, L, and N_u — remained the same. Later we realized that in the non-Ohmic regime the number of hops N_u gradually increased with current. Equation (2.56) remains accurate only for $u_I > u_M$. Therefore, only $u_I > u_M$ points were included when plotting the five curves in Fig. 2.13.

We see that $L_c \approx 1.9 u_M a$, which is the average hop length. This implies that the average *conductance* is dominated by rare samples that do not contain large breaks, so that the total voltage is distributed roughly equally among all the hops. In contrast, we know that the average *resistance* is determined by typical samples where the breaks are present; the entire voltage is applied to the single most resistive hop, and the size of the non-Ohmic effect is much larger, see Fig. 2.15.

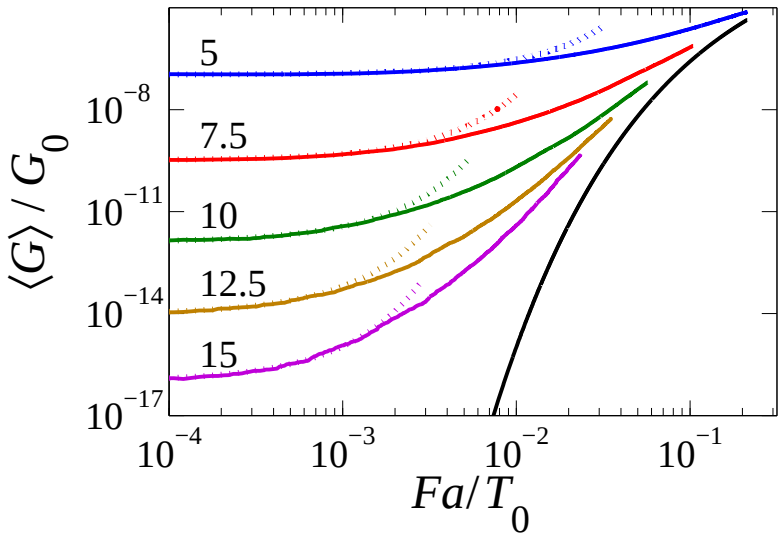

Figure 2.13: Conductance as a function of Fa/T_0 (five solid lines on the left) for $L = 10^3$ and $a = 4$. The values of u_M are indicated next to each curve. The fits to Eq. (2.77) used to extract L_c are shown by the dotted lines. The rightmost curve is Eq. (2.78).

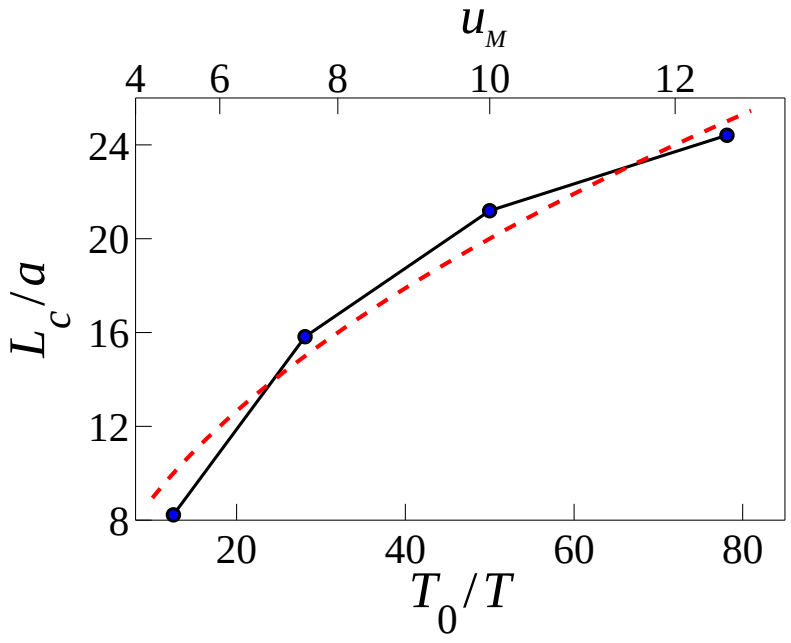

Figure 2.14: Characteristic length L_c [Eq. (2.77)] that determines the non-Ohmic behavior as a function of temperature (dots). For comparison, the dashed curve represents the relation $L_c/a = 1.9u_M$, which corresponds to a typical hop length.

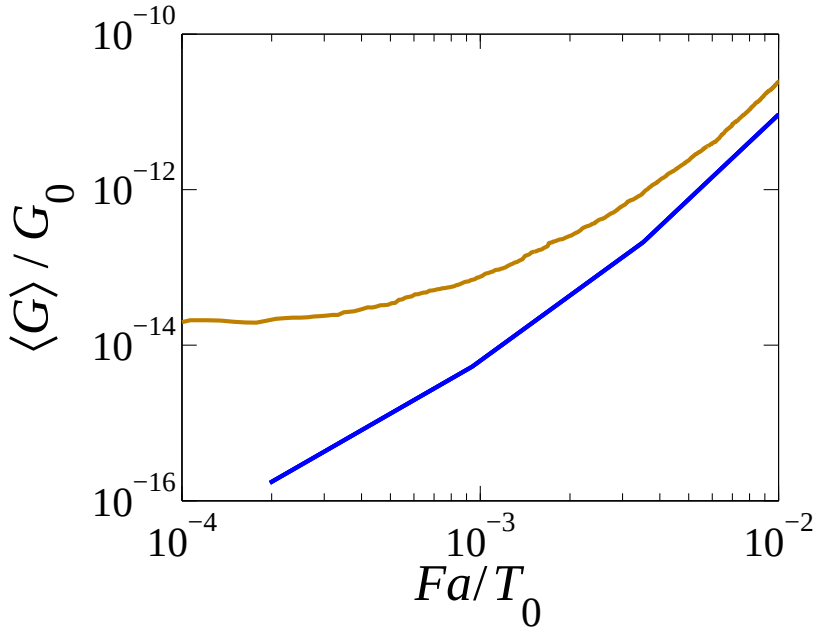

Figure 2.15: Dependence of the conductance on the scaled electric field averaged in two different ways. The upper line is the average conductance, the lower one is the inverse of the average resistance. Simulation parameters are the same as in Fig. 2.9.

At large F the rise of the conductance becomes less rapid than exponential and the curves in Fig. 2.13 tend to converge to a common T-independent envelope of Eq. (2.78), confirming the analytical predictions of Fogler and Kelley. [26] At such high electric fields F, high-resistance breaks are eliminated not only from rare samples but from typical ones. This can be deduced from the fact that averaging of the conductance G approaches the result of averaging of the resistance R (followed by taking the inverse). As evident from Fig. 2.15, the two curves indeed approach each other with increasing field.

2.2.7 Conclusion

At this point, let us recapitulate our findings. To the best of our knowledge we presented the first reliable calculation of the statistics of resistances in 1D VRH network, both in Ohmic and non-Ohmic regimes. Comparing with the previous theoretical work, we showed the importance of the correction to the PDF $P(u)$

proposed in Ref. [80]. We demonstrated that without this "subleading" term the conductance could be significantly overestimated, see Fig. 2.11. Figure 2.7 further illustrates the importance of such corrections by showing that there are no obvious diamond-like or hexagonal voids in the energy-position space invoked in the derivations of the leading asymptotic behavior. [77, 26]

Next, our calculations have verified the earlier analytical predictions [26] that large breaks are progressively eliminated at higher voltage, and that the PDF of resistances becomes more narrow, see Fig. 2.10. This disappearance of highly resistive hops equalizes different samples, making the averages of parallel and series setups of the wires approach the same value.

Let us now turn to experiments. Unfortunately, we could not find a clear evidence of the predicted behavior in published literature. A dedicated experiment to probe mesoscopic conductance fluctuations in non-Ohmic regime is desired as it was not on the agenda in previous studies of 1D VRH. At least two other caveats must also be kept in mind. First, most of "1D" electron systems studied experimentally were not truly one-dimensional. They either consisted of many parallel chains [3, 5] or had multiple subbands [44, 33, 31] or were bulk samples with a large aspect ratio. [70, 41] Such systems may behave as effectively 1D but only at low enough T. Finally, our model of disorder where LS are treated as points in the energy-position space may or may not be relevant for some of these experiments (see more below).

Turning to some specific examples, we consider first the measurements done on polydiacetylene single crystals, [5] which are quasi-1D materials. The Ohmic transport is consistent with 1D VRH behavior, showing a crossover from a simple exponential at relatively high temperatures, $\ln G \approx -\Delta_h/2T$, to a stretched exponential $\ln G \approx -(\Delta_l/T)^\gamma$ with $\gamma = 0.5$–0.75 at low T. As in our simulations, there is a substantial difference between these energy scales, e.g., in sample S1, $\Delta_h = 320\,\mathrm{K}$ and $\Delta_l = 2570\,\mathrm{K} \approx 8\Delta_h$. In the same sample at high electric fields Eq. (2.78) is observed, with $8T_0/a = 0.049\,\mathrm{eV/nm}$ (in our notations). Assuming that $T_0 \approx \Delta_h$, this gives a reasonable estimate of the localization length $a = 4.3\,\mathrm{nm}$. At modest fields, the transport data were fitted to Eq. (2.77) and L_c

was extracted. It was seen to have the same temperature dependence $L_c \propto T^{-0.5}$, as in our simulations. Moreover, the numerical value of L_c is close to what we find. For example, $L_c = 32.5\,\mathrm{nm}$ at $T = 25\,\mathrm{K}$ in the experiments, which can be compared to $L_c \sim 1.9a\sqrt{2T_0/T} = 40\,\mathrm{nm}$ that we find, cf. Fig. 2.14.

Next, let us consider another experiment, which was done on arrays of GaAs quantum wires. [44] The dependence of G on F and T that we have calculated here is in a reasonable agreement with some of those experimental results but some strong deviations are also apparent. In the simulations, the range of activated behavior in the Ohmic regime spans at best two decades in G. In the experiment, it is much wider (three decades), and occupies most of the temperature range studied.

The initial rise of G with F is again exponential over approximately one decade, see Fig. 2.16. However the behavior of parameter L_c in this exponential law was deemed to be surprising in Ref. [44]. Therefore, let us discuss it. Physically, L_c is the distance between "critical hops" in a sample, i.e., those highly resistive links that generate the dominant portion of the total voltage. In a typical sample, length L_c has to be much larger than the average hop length $u_M a$. In fact, at low T one would naively expect L_c to be of the order of the sample length L. This is because in a typical sample all the voltage drops on a single break. At higher T, where the activated transport is observed, the voltage is shared by many breaks, [77] and so L_c is supposed to decrease exponentially. However, this is not what was observed. At low T, two out of three samples, measured in Ref. [44] had $L_c \approx L/50$, while the L_c of the third was about $L/10$. As T was increasing, L_c was decreasing but rather slowly, perhaps, as $T^{1/2}$.

In light of our findings, this behavior of L_c is *not* surprising. The above reasoning does not take into account that the measurements were done not on a single wire but on several hundreds of them, connected in parallel. It is logical to assume that some wires conducted much better than others because they happened to have no breaks. These wires could short out the wires which were poor conductors, reducing the net L_c down to the typical hopping length.

We now demonstrate that L_c extracted from our model has numerical val-

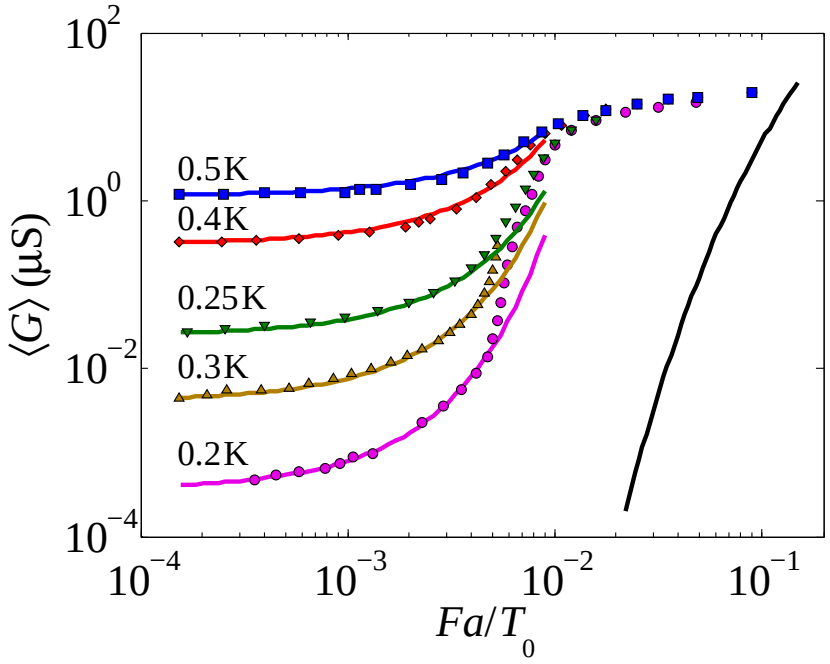

Figure 2.16: G of sample 1 of Ref. [44] as a function of Fa/T_0 for different T(markers). $T_0 = 6.2\,\mathrm{K}$ is determined from the best fit of Eq. (2.80) to the Ohmic conductance (not shown) and $a = 0.4\,\mu\mathrm{m}$. The best fits to Eq. (2.77) are shown by the lines. The rightmost curve is Eq. (2.78).

ues and functional behavior similar to what was measured experimentally. Our L_c, which was found by fitting the low-voltage part of $G(F)$ curves in Fig. 2.13 to Eq. (2.77) is plotted in Fig. 2.14. The intervals of T_0/T are different in our simulation and the experiment; however, there is a small overlap. For our leftmost point, $T_0/T = 12.5$ we have $L/L_c \approx 30$, similar to the numbers quoted above.

The problem arises when we consider the high-field behavior reported in Ref. [44]. Experimental $G(F,T)$ curves tend to approach a common T-independent limit, as in our calculations, Fig. 2.13. However, this limit is strongly underestimated by our Eq. (2.78), see Fig. 2.16. While we do not know the origin of this discrepancy, it is possible that the different behavior seen in the two experiments is just another example of a dilemma, which has a long history in the VRH literature. Previously, it was discussed mostly in the context of bulk materials where majority of experiments have been done so far. However, it is tempting to make a comparison with our 1D case because the VRH exponent of the Efros-Shklovskii

law in any dimension nominally coincides with the 1D Mott law exponent $\gamma = 1/2$.

The essence of the dilemma is as follows. There are a number of systems where non-Ohmic behavior does follow Eqs. (2.77) and (2.78) that we have observed in our simulations. However, this is usually the case when parameter Δ in Eq. (2.79) is large, say, tens or hundreds of K. Very different and still poorly understood behavior occurs when T_0 is relatively small (according to one study, [107] when $\sqrt{T_0/T} \lesssim 12$). The high-field nonlinearities in this second group are much stronger. In the extreme cases, the I–V characteristic was determined to be S-shaped, [48, 89] which led to hysteretic conductivity jumps by orders of magnitude [48, 71] and circuit oscillations. [89] [Note that the negative differential conductivity (NDC), which is also sometimes observed in the non-Ohmic regime, [2] is a different effect. In that case the I–V characteristic is N-shaped. The magnitude of the nonlinearity is much weaker. According to the theory, [16, 67, 54, 64] this NDC requires special conditions, e.g., narrow energy bands or low carrier densities.] Interestingly, in systems that show conductivity jumps the Ohmic conductance shows a simple activation rather than VRH behavior. [48, 71]

It has become common [97, 22, 89, 107, 33, 58, 51, 30, 71, 6] to attribute strong nonlinearity and S-shaped I–V to electron overheating. It is assumed that G is the function of the electron temperature T_e, which can be much higher than the ambient temperature T. A phenomenological equation is postulated,

$$\dot{Q} = GF^2 = \alpha(T_e^\beta - T^\beta)\,, \tag{2.92}$$

where α and β are adjustable constants. (Usually, $4 < \beta < 8$.) This equation is supposed to represent the balance between the Joule heat delivered into electron system from the external field and the heat transferred from electrons to phonons. Surprisingly, this equation has been shown to provide an accurate description of some VRH systems, including the the one we are trying to make comparison to. [44, 33]

By itself, the idea of hot electrons is not objectionable. Actually, our Eq. (2.78) can be viewed as the 1D Mott law with the electron temperature $T_e \sim Fa$ (similar to Refs. [85] and [7]). The difficulty is that the required T_e is unusually large. Indeed, let us define the length $L_{\text{e-ph}} = T_e/F$. It has the physical meaning

of a characteristic distance over which an electron must be accelerated by the external field to gain the extra energy $T_e \gg T$. In our model, where LS are treated as points, the largest achievable $L_{\text{e-ph}}$ is of the order of a. Electrons cannot propagate farther without suffering an exponential decay. Yet to get a stronger I–V nonlinearity than predicted by our Eq. (2.78), $L_{\text{e-ph}}$ must exceed a. For example, to reproduce the high-field part of the data shown in Fig. 2.16, we need perhaps $L_{\text{e-ph}} \sim 10a$.

In principle, $L_{\text{e-ph}} \gg a$ is possible if the disordered system is a granular metal or equivalently, an array of random-sized quantum dots. In this case the upper bound on $L_{\text{e-ph}}$ is presumably set by the size of metallic grains, while the exponential decay length a is much smaller, being suppressed by weak tunneling between the grains. The granular-metal model can also explain a wide range of the activated Ohmic behavior as a manifestation of the Coulomb blockade. Finally, it has been suggested [48] that the conductivity jumps may be related to lifting of the Coulomb blockade by collective depinning. Transport in a 1D version of this model was recently studied in Ref. [27] but the case of extremely strong fields was not considered. It remains to be seen whether this model can yield a better agreement with the experiments. [44]

It has been speculated that the overheating is driven by the electron interactions, which we did not address here. The simplest way to introduce some interaction effects into the existing formalism is to consider larger dielectric constant $\epsilon > 1$. The importance of such effects requires further study.

Finally, as mentioned above, most of electron systems studied should behave as effectively 1D only at low enough T. The dimensional crossover as a function of temperature in a strip geometry has been studied by RR in Ref. [78]. It would be interesting to investigate the electric-field counterpart of this crossover.

2.3 Apparent Power-Law Behavior in Quasi-1D Systems

From the last section, it is clear that when measuring the conductance $G(V,T) \equiv I(V,T)/V$ of a system characterized by variable range hopping, one expects ot see a (stretched) exponential behavior. However, over the last decade, observations of different laws,

$$I \propto VT^{\alpha}, \quad V \ll (2\pi/\gamma)T, \tag{2.93}$$

$$\propto V^{\beta+1}, \quad V \gg (2\pi/\gamma)T, \tag{2.94}$$

have been reported in systems as diverse as carbon nanotubes [15, 102, 9, 42, 32, 62, 19, 21], InSb [106] and GaAs [18, 95] quantum wires, $NiSe_3$ whiskers [88], polymer nanofibers [4, 75], inorganic [96, 21] and organic nanowires [108], as well as polymer films [105, 99]. The coefficients α, β, and γ vary among different materials and different samples of the same material.

A five-parameter formula frequently used to fit the experimental data is

$$I = c_0 T^{\alpha+1} \sinh\left(\frac{\gamma' V}{2T}\right) \left|\Gamma\left(1 + \frac{\beta}{2} + i\,\frac{\gamma V}{2\pi T}\right)\right|^2 . \tag{2.95}$$

For $\gamma' = \gamma$ the asymptotic behavior of $I(V,T)$ is given by Eqs. (2.93) and (2.94). Agreement with Eq. (2.95) was advocated as evidence for tunneling into Luttinger liquid (LL) [34] — a one-dimensional (1D) system with nonperturbative interaction effects. (For strong interactions the LL can also be modeled as a 1D Wigner crystal [23].) In this picture, the system contains a tunneling barrier, e.g., a poor contact, but is otherwise clean and free of localization. The power-laws are due to renormalization of this barrier by many-body effects. However, there is a problem with this interpretation. The actual calculations [43, 81, 11, 61, 82] within the LL model give $\alpha = \beta$ and $\gamma = \gamma' = 1$, which is not always consistent with the parameters of the empirical fits (a notable exception is Ref. [18]).

Another reason to doubt the relevance of the LL effects in some of these experiments is the fact that the systems studied are neither perfectly clean nor truly 1D. They are, typically, collections of many parallel 1D channels, whose

total number ranges from several hundred to many thousands, each containing multiple impurities.

In this section, we show that in such quasi-1D systems the conventional mechanism of transport, which is the VRH, can also lead to Eqs. (2.93)–(2.95). This is because at low enough T the hopping length is not much smaller than the length L of the wires. In this case, the VRH conductance deviates from the usual formula, Eq. (2.79). The hopping is dominated by hopping paths that consist of a few approximately equidistant hops [92, 53, 35, 10]. Although rare, such configurations can always be found in a sample if the number of channels is large enough. Hence, despite mesoscopic fluctuations that accompany rare events, $G(V,T)$ can be a smooth quasi-power-law function.

Following the procedure described in Sec. 2.2.6, we obtain a number of G-V curves at different temperatures, from which we can get the I-V profiles. Our results are illustrated in Fig. 2.17. In the inset of Fig. 2.17 we show a set of I-V curves computed for a set of fixed T. In the main panel, we collapse them onto a single "universal" curve described by Eq. (2.95).

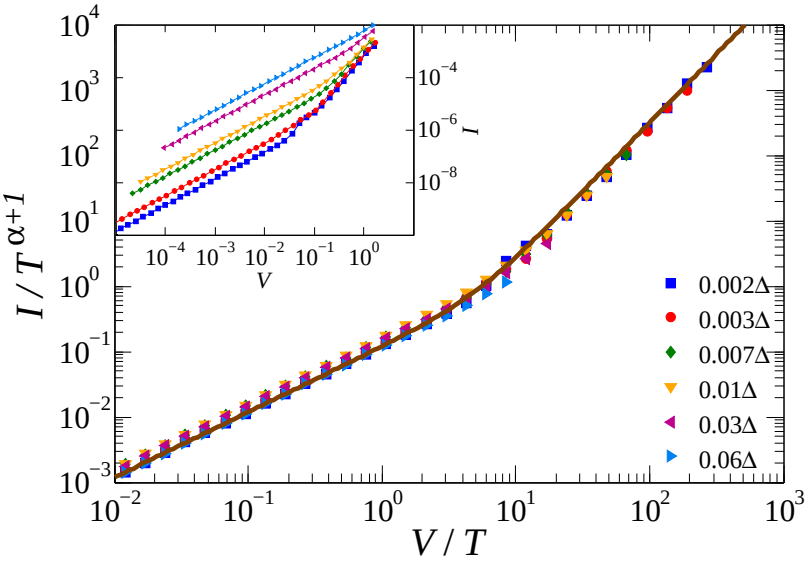

Figure 2.17: Collapse onto the "universal curve" of Eq. (4) (solid line) for the numerical results for $L = 30$ and $a = 4$ (symbols) as $I/T^{\alpha+1}$ *vs.* V/T, with $\alpha = 1.75$, $\beta = 1.1$, and $\gamma = 1$. T is in the units of $\Delta = 4T_0$. Inset: Same data plotted as I *vs.* V.

Let us compare the quality of the data collapse to those in the aforementioned experiments [96, 88, 4, 108, 75, 19, 105, 99]. The range of T shown in Fig. 2.17 is a factor of 30. In the experiments, Eq. (2.93) rarely spans more than one decade in T. The range of V, where the *non*-Ohmic conductance follows the "universal" curve in the experiments, is usually less than a decade. In our case, it is wider than one decade. Still, the dependences that we find numerically are not true power-laws. If we look at wider ranges of V and T, the deviations are seen. Therefore, our numerical results for the VRH transport, just like the experiments, demonstrate only the apparent power-law behavior (APLB) restricted to a certain parameter range.

In our calculations, this range is located near the inflection point of the curve $\ln G_\Omega$ *vs.* $\ln T$, see Fig. 2.18. Near the corresponding temperature $T_{\rm inf}$ the curve can be approximated by a straight line with a certain slope α, in agreement with Eq. (2.93). Further analysis, following Refs. [92, 53, 35], which is discussed below, leads to analytical estimates

$$\alpha = N_{\rm inf} - 1 - \frac{2}{N_{\rm inf}}\,, \quad N_{\rm inf} = c_1\sqrt{\frac{L}{a}}\,, \tag{2.96}$$

$$\beta + 1 = c_2\alpha\,, \quad \gamma = c_3\,\frac{2\pi a}{L}\,, \tag{2.97}$$

$$T_{\rm inf} = c_4 T_0\,\frac{a}{L}\,, \quad T_0 \equiv \frac{1}{ga}\,. \tag{2.98}$$

Here g is the density of states and c_i's are coefficients of the order of unity. In comparison, our simulations give $\alpha = 1.75$, $\beta = 1.1$, and $\gamma = 1$ for $L/a = 7.5$. For $L/a = 12.5$, we get $\alpha = 2.4$, $\beta = 1.7$, and $\gamma = 0.6$. This implies $c_1 \approx 1.1$, $c_2 \approx 0.85$, $c_3 \approx 1.2$, and $c_4 \approx 0.4$.

Our numerical results are comparable with typical experimental numbers. They are also consistent with the observed trend that longer and more disordered wires produce larger α and β but smaller γ. A more detailed comparison would require taking into account particularities of a given set of samples beyond our generic model. Due to individual variations in the nature of disorder and the parameters of electron-phonon coupling, α and β may acquire additional corrections of the order of unity.

The results for the Ohmic regime (Fig. 2.18) were obtained by choosing a

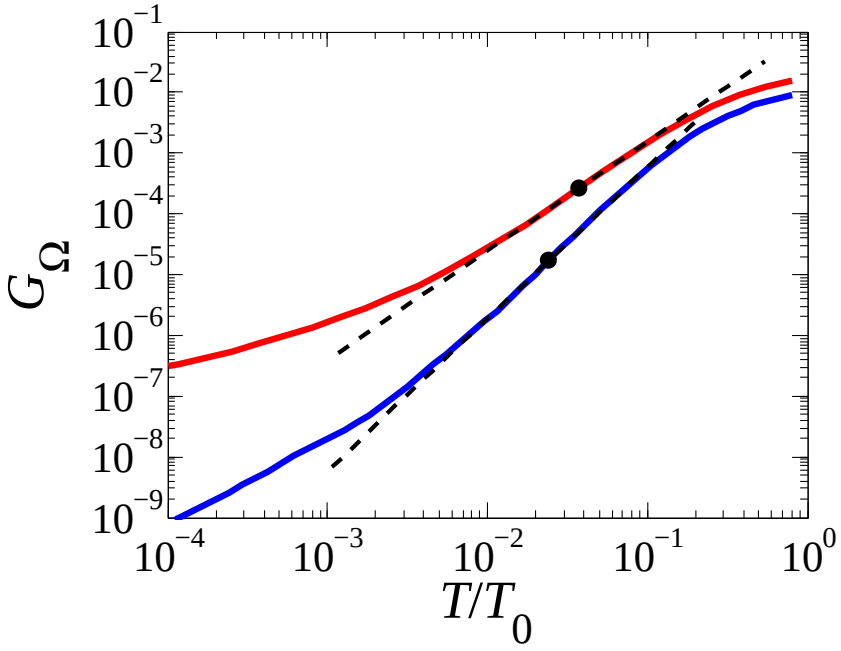

Figure 2.18: The Ohmic conductance *vs.* temperature for $L = 30$ (upper curve) and $L = 50$ (lower curve) with $a = 4$. The dashed lines serve to illustrate the apparent linearity of the curves near their inflection points (dots).

very large $u_I = 40$ to ensure $V \ll T$. We analyzed two different system lengths: $L = 30 = 7.5a$ and $L = 50 = 12.5a$. For $L = 30$ we generated an ensemble of $20,000$ samples and for $L = 50$ we used $10,000$ samples in order to average out the mesoscopic fluctuations. (Actually, using 500 samples would give results of comparable quality.) Figure 2.18 clearly demonstrates more than a decade of the APLB of Eq. (2.93) near the inflection points of the curves. Note that this point is located at a lower temperature for the longer sample.

Having determined the range of T where we get the Ohmic APLB, we proceeded to analyzing the non-Ohmic behavior of the system in this range of temperatures. To this end we fitted the results for higher V to Eq. (2.95). For $L = 30$, Fig. 2.17, we found a good collapse in both the Ohmic and non-Ohmic regimes. All curves in Fig. 2.17 were cut at $V = 2$, since at that point the curves were beginning to saturate as they approached the maximum current possible in the system. The collapse obtained for $L = 50$ (not shown) was equally good. The quality of our data collapse matches or exceeds that in the experiments [4, 88, 96,

108, 19, 75, 105, 99]. The values of the fitting parameters α, β, and γ have already been discussed (see more below).

Let us now examine how the APLB we have found numerically can be understood in the light of established theory of 1D VRH. According to this theory, transport is characterized by several regimes. At low T, the conductance of the ensemble is dominated by rare paths with nearly equidistant sites, see Fig. 2.19(b). This regime was studied in Refs. [35, 10, 12] for two intermediate sites and in Refs. [92, 53] for a chain of many sites (Ref. [92] is available online as Ref. [72]). Adopting the derivation in Ref. [92] to the 1D case we can show that at a given T the main contribution to G_Ω comes from the chains of $N = \sqrt{2L/\lambda a}$ hops, where λ is the solution of the equation $\lambda \simeq \ln(\lambda/LgT)$. In addition, [35, 10, 101]

$$\frac{d\ln G_\Omega}{d\ln T} \simeq N - 1 - \frac{2}{N}\,. \tag{2.99}$$

At $T = T_{\rm inf}$, we have $\lambda \sim 1$, which yields Eq. (2.96).

For $T > T_{\rm inf}$, the system enters the regime where the transport is limited by rare highly resistive links — "breaks" — on the optimal path [45, 50, 77]. As a result, the Ohmic conductance, which can be derived from the formulas of Ref. [77], obeys Mott law. The concavity of the $\ln G_\Omega$ *vs.* $\ln T$ curve is opposite in the two temperature ranges, which creates the inflection point, see Fig. 2.18.

The non-Ohmic transport is also characterized by an S-shaped curve of $\ln I$ *vs.* $\ln V$, with its own inflection point. For example, at $T \gg T_{\rm inf}$, the theory [26] predicts

$$\ln\frac{V}{T_0} = -\frac{u_I^2}{u_M^2} + \ln\left(\frac{8L/a}{u_I^2}\right)\,, \quad u_M \equiv \sqrt{\frac{2T_0}{T}}\,. \tag{2.100}$$

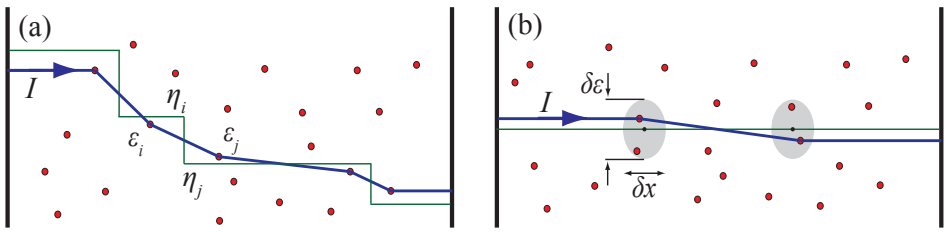

Figure 2.19: (a) A typical hopping path through the wire (thick line). The thin line represents electrochemical potential η. (b) A rare path [92, 53, 35, 10] made of equal-length hops. Here $\delta\epsilon \sim NT$ and $\delta x \sim Na$, where N is the number of hops.

By the argument similar to that used in the Ohmic regime, $\beta + 1$ in Eq. (2.94) is determined by the maximum slope, i.e., the derivative of $\ln I$ with respect to $\ln V$:

$$\beta + 1 = \max\left(-\frac{du_I}{d\ln V}\right) = \frac{u_M}{4} = \sqrt{\frac{T_0}{8T}}\,. \tag{2.101}$$

We see that $\beta + 1 \propto T^{-1/2}$ is not a constant but decreases with T, in qualitative agreement with experiments [108, 75, 19]. This explains why the data collapse onto the universal curve of Eq. (2.95) can be achieved only in a limited range of T.

At $T = T_{\rm inf}$, Eq. (2.100) is at the border of its validity. Hence, Eq. (2.101) gives only the order of magnitude estimate, $\beta + 1 \lesssim \alpha$, which is the first part of Eq. (2.97). Finally, to get γ we note that the crossover to the T-independent behavior in Eq. (2.95) takes place at $\gamma V \sim 2\pi T$. On the other hand, according to Eq. (2.100), this occurs at $u_I \sim u_M$ where $V/T_0 \sim LT/aT_0$. Combining these expressions, we recover the second part of Eq. (2.97).

Formulas (2.96)–(2.97) predict numerical values and relations among α, β, and γ that are in agreement with most of the cited experiments [96, 88, 4, 108, 75, 19, 105, 99]. Additionally, they provide a way of estimating the localization length a. For example, taking parameters $\alpha = 4.3$, $\beta = 2.1$, $\gamma = 0.25$, $L \sim 1\,\mu$m of a representative $MoSe_2$ nanowire from Ref. [96], we find $a \sim 40\,$nm for this sample (W3). Other samples measured in that work showed $\alpha \propto 1/\sqrt{M}$ scaling with the number of transport channels M. In our model the same scaling occurs if $a \propto M$, as in a weakly disordered quasi-1D metal. In such a system a can be enlarged by applying an external magnetic field [13]. This is one convenient way to further test our model experimentally. Alternatively, it may be possible to vary the disorder strength and therefore a by electrostatic gating, while monitoring the predicted trends in α, β, and γ.

Another model we considered in search for the APLB was the interrupted-strand model (ISM) [28, 27]. Therein a metallic wire is divided into segments by randomly positioned impurities of tunneling transparency $e^{-s} \ll 1$, which turn it into a chain of weakly coupled quantum dots. In the simulations we studied wires with $N_i = 50$ impurities of strength $s = 4$. While we did observe the APLB in

such wires ($\alpha = 3.75$, $\beta = 1.6$, $\gamma = 0.15$), the quality of the data collapse was not as good as in Fig. 2.17. Otherwise, the results were similar.

Note that the VRH in the ISM is analogous to multi-dot cotunneling in a granular metal. The latter also leads, in all spatial dimensions, to the power-law conductance behavior with $\alpha = \beta = 2N_d - 4$, N_d being the number of dots involved in one cotunneling event [94]. Hence, the APLB is not uncommon in the VRH regime.

2.4 Structure of the hopping network in finite-size systems of arbitrary dimension d

2.4.1 Introduction

The previous two sections of this chapter dealt with hopping in quasi-one-dimensional systems. To reiterate, usually, the Ohmic conductance as a function of temperature T is described by the Mott law:

$$G \sim \exp\left[-\left(\frac{T_0}{T}\right)^{\frac{1}{d+1}}\right], \tag{2.102}$$

where we assume that g can be treated as a constant at all T of interest. [1] However, sometimes systems do not follow the behavior predicted by Eq. (2.102) and instead exhibit a different T dependence. In particular, for certain temperature ranges power-law-like behavior

$$G \sim T^{\alpha} \tag{2.103}$$

has been observed experimentally in a variety of quasi-1D materials. [106, 88, 96, 108] The value of α varies widely even between samples of the same material, showing the dependence on the length of the system.

Following Ref. [92, 35] we also argued that the Mott law results from typical events of the dense resistor network, see Fig 2.20(b). On the other hand,

[1] In particular, we do not consider the physics of Coulomb gap and the Efros-Shklovskii law of VRH [87].

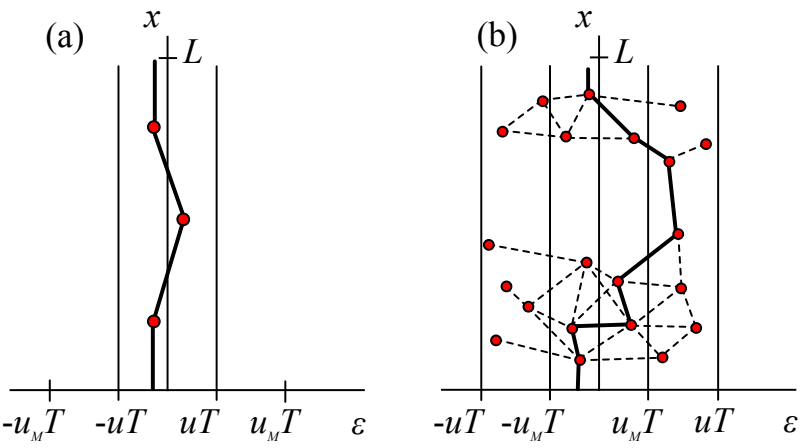

Figure 2.20: (a) Rare hopping paths that dominate the ensemble-averaged conductance of 1D VRH transport at low T. (b) Typical hopping path at higher T. The thick black line represents the dominant subnetwork, responsible for the conductance.

quasi-power-law behavior originates from rare, approximately equidistant chains of hopping sites like the one shown in Fig. 2.20(a).

In this section, we study how the transition between these seemingly distinct mechanisms of transport occurs as a function of T. While we are mainly interested in $d = 1$, where we can utilize both numerical simulations and analytical computations, we also study the case $d > 1$ using qualitative physical considerations.

This section is organized as follows. Section 2.4.2 discusses the approach we take to analyze the problem. Sections 2.4.3 and 2.4.5 deal with 1D and higher-dimensional systems, respectively. The discussion of prior treatment of the problem is found in Sec. 2.4.6. Finally, the derivations are located in the Appendix.

2.4.2 Percolation Approach

We have already described the standard Miller-Abrahams resistor network[60] in terms of percolation formalism in Sec. 2.1.4 when we introduced Mott law. Recall that Eq. (2.16) shows that the percolating resistance $u_c = [2T_0B_c/(T\beta_d)]^{\frac{1}{d+1}}$ scales with $(1/T)^{\frac{1}{d+1}}$, as predicted by Mott law. However, this result neglects the finite probability of rare paths that have higher conductivity than the percolating

network. To account for the contribution from these paths, we define the crossing probability $P_L(u)$ as the probability that there exists a path that traverses a system of length L with all link resistances smaller than u. Thus, $P_L(u)$ is is a cumulative distribution function (CDF) of the critical values of u.

In traditional bond problems, the crossing probability evolves smoothly with the open bond fraction as the network becomes denser. Likewise, in our problem $P_L(u)$ is expected to vary smoothly with changing u. This means that the geometry of the network also undergoes a gradual development from isolated clusters of open bonds to a dense network spanning the system, see Fig. 2.21.

It is clear that the form of $P_L(u)$ depends on the dimensionality of the system and the details are left for the following sections where we treat 1D and higher-dimensional systems separately. Here we give the motivation for determining the crossing probability.

Since the conductance of the system is approximately given by e^{-u}, where u is the measure of resistance of the most resistive link of the subnetwork, multiplying e^{-u} by $P_L(u)$ gives the probability distribution of the conductance. Disregarding the details due to the dimensionality, for a finite-size system $P_L(u)$ is a sharply increasing smooth step-like function. The product of a rapidly decaying exponential with $P_L(u)$ results in a maximum which allows one to approximate the average conductance as

$$G(T) \sim e^{-u_*}\,, \tag{2.104}$$

where u_* is the location of the maximum of the product $e^{-u}P_L(u)$. Equation (2.104) means that $G(T)$ is a smooth function unless there is a discontinuity in $u_*(T)$. Such jumps may indeed occur in the presense of multiple local maxima because both e^{-u} and $P_L(u)$ are exponential functions of u.

In the following sections we discuss the form of the crossing probability and determine the distribution of conductance for different dimensionalities.

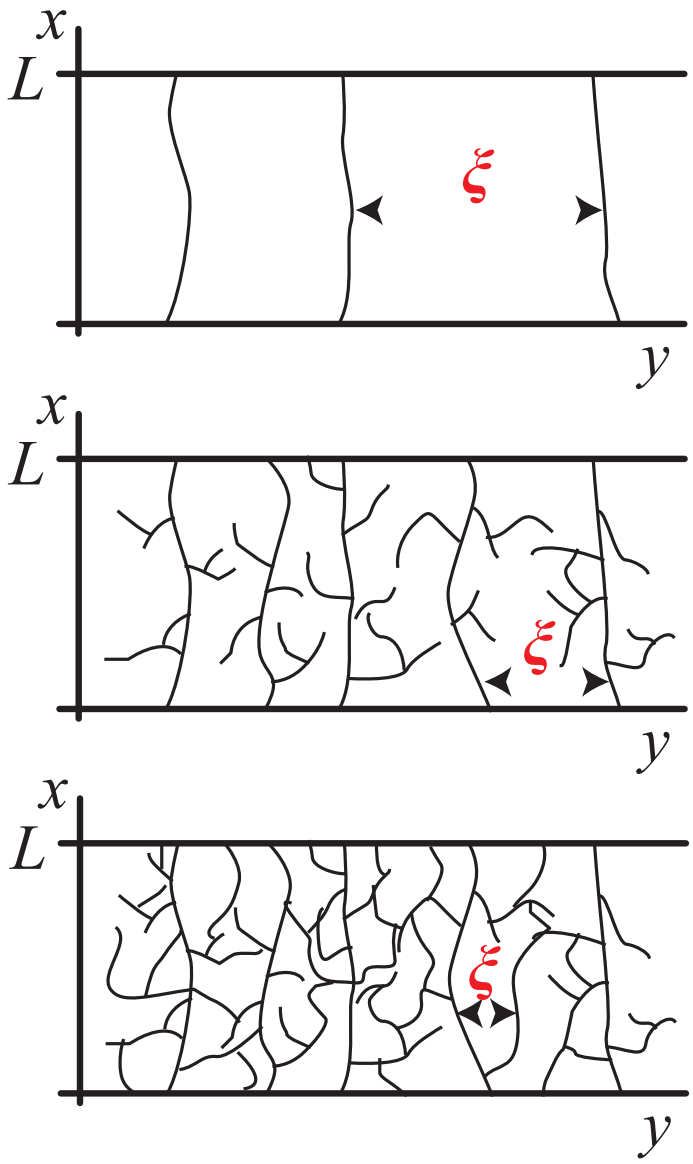

Figure 2.21: Evolution of a 2D network with increasing u. As the value of u is raised from top to bottom panels, the network progresses from independent conducting strands to an interconnected grid. The correlation length ξ decreases as the network becomes denser.

2.4.3 1D systems

Analytical approach

Although there is no simple way to compute the crossing probability analytically, it is possible to estimate its behavior at extremal values of u. One can approximate the high-u behavior of $P_L(u)$ using the following geometrical argument. Recall that the area of a diamond break is equal to $Tau^2/2$. Given the density of states g, the probability that there are no sites found within the diamond is $\exp\left[-u^2/u_M^2\right]$. If the sample length is L, the number of breaks of the above size that can fit in the sample is $2L/(ua)$. Finally, the probability that there will be no breaks of resistance u or above is

$$\ln\left[P_L(u)\right] \sim -\frac{2L}{ua}\exp\left[-\frac{u^2}{u_M^2}\right]. \tag{2.105}$$

Applying Eq. (2.104) results in the following expression for u_*:

$$\frac{au_M^2}{2L} = e^{-\frac{u_*^2}{u_M^2}}\left(2+\frac{u_M^2}{u_*^2}\right). \tag{2.106}$$

For sufficiently large values of u_* we can drop the second term inside the parentheses. We, therefore, obtain the behavior of G as

$$G \sim \exp\left[-u_M \ln^{\frac{1}{2}}\left(\frac{4L}{au_M^2}\right)\right]. \tag{2.107}$$

Equation 2.107 reproduces the result obtained in Ref. [77]. There, the authors integrated the resistance distribution using the resistance of the largest expected break as the upper limit of the integral. This took into account the finite size of the system, giving a result that agrees with ours.

We can also determine the behavior of $P_L(u)$ for $u \ll 1$.

To analyze the behavior of $P(u)$ at low u, we introduce the function

$$Z_{N-1}(u,L) = g^{N-1}\int_0^\infty \prod_{i=1}^{N} d\vec{r}_i \int_{-uT}^{uT} \prod_{i=1}^{N-1} d\varepsilon_i Q_i\,, \tag{2.108}$$

$$Q_i = \delta(L-\sum_{i=1}^{N} x_i)\prod_{i=1}^{N}\Theta(u-u_{i,i-1})\,. \tag{2.109}$$

Summing over all N's yields the unnormalized probability of finding a path with all link resistances $\leq u$. For any path, the energies of the electrode sites, ε_0 and ε_N, are both 0. In addition, in higher dimensional systems, the first and the last hops have no lateral displacement in order to reduce the resistance. Taking the Laplace transform of Eq. (2.108) with respect to L changes the integrand into

$$\tilde{Q}(u_i) = \prod_{i=1}^{N} e^{-sx_i}\Theta(u-u_i)\,. \tag{2.110}$$

Introducing an auxilary variable

$$\phi_i = u - \frac{|\varepsilon_i| + |\varepsilon_{i-1}| + |\varepsilon_i - \varepsilon_{i-1}|}{2T}\,, \tag{2.111}$$

results in

$$\tilde{Z}_{N-1}(u,s) = g^{N-1}\int_{-u_0T}^{u_0T}\prod_{i=1}^{N-1} d\varepsilon_i \prod_{i=1}^{N}\Omega_i\,, \tag{2.112}$$

$$\Omega_i = \int_0^\infty d\vec{r}_i\Theta\left(\phi_i - \frac{2r_i}{a}\right)e^{-sx_i}\,. \tag{2.113}$$

In 1D, all Ω_i's have the same form:

$$\Omega_i = \frac{1-e^{-\frac{\phi_i as}{2}}}{s}\,. \tag{2.114}$$

We introduce two changes of variables: $\zeta \equiv \varepsilon/(u_0T)$ and $c = as/2$. This turns Eq. (2.112) into

$$\tilde{Z}_{N-1}(u,c) = g^{N-1}\left(\frac{a}{2}\right)^N \frac{(uT)^{N-1}}{c^N} f_{N-1}(0)\,, \tag{2.115}$$

where

$$f_j(\zeta) = \int_{-1+\zeta\Theta(\zeta)}^{1+\zeta\Theta(-\zeta)} d\eta\, A(\zeta,\eta) f_{j-1}(\eta)\,, \tag{2.116}$$

$$A(\zeta,\eta) = 1 - e^{-\lambda}\,, \tag{2.117}$$

$$\lambda(\zeta,\eta) = uc\left(1 - \frac{|\zeta| + |\eta| + |\zeta-\eta|}{2}\right)\,. \tag{2.118}$$

$$f_0(\zeta) = \Omega_0(\zeta)\,. \tag{2.119}$$

Taking the inverse Laplace transform gives

$$Z_{N-1}(u,L) = \frac{1}{2\pi i}\int_{-i\infty+\gamma}^{-i\infty+\gamma} dc\,\frac{2}{a}\tilde{Z}_{N-1}(u,c)e^{2Lc/a}\,. \tag{2.120}$$

We approximate the result of the integral by Eq. (2.122) with c_0 being the largest pole, given by the solution to the equation

$$g^{N-1}\left(\frac{a}{2}\right)^{N-1}\frac{(uT)^{N-1}}{c_0^{N-1}}f_{N-1}(0)=1\,. \tag{2.121}$$

For $N \gg 1$ we expect $f_{N-1}(\zeta) \simeq \alpha\kappa_0^{N-1}\psi(\zeta)$, where $\kappa_0 = \kappa_0(u,c)$ is the largest eigenvalue of the integral operator $A(\zeta,\eta)$ and $\alpha(u,c)$ is the overlap of $f_0(\zeta)$ with the corresponding eigenfunction $\psi(\zeta)$. Substituting $f_{N-1}(0) \simeq \alpha\kappa_0^{N-1}\psi(0)$ into Eq. (2.121) yields

$$\ln[P_L(u)] \sim \frac{2Lc_0}{a}\,, \tag{2.122}$$

where c_0 is the solution of

$$\frac{\kappa(uc_0)}{uc_0}=\frac{u_M^2}{u^2}\,. \tag{2.123}$$

Equation (2.122) provides the lower limit of the spanning probability since it takes into account only the possibility of the nearest-neighbor hopping. This approximation is, however, justified for sufficiently low uT. For $u \ll u_M$, one obtains

$$|c_0| = \frac{1}{u}\ln\left(\frac{u_M^2c_0^2}{\kappa_*}\right) = \frac{2}{u}W\left(\frac{\sqrt{\kappa_*}}{2}\frac{u}{u_M}\right)\,, \tag{2.124}$$

where $\kappa_* \approx 1.18$ and W is the Lambert function. The value of κ_* comes from Ref. [92] where authors determined the largest eigenvalue for the operator $A(\eta,\xi)$ above for small u. Our Eq. 2.124 is similar to an equation in Ref. [73]. Unlike our paper, however, the authors treated a 3D system using the number of hops N as their main variable, in contrast to u which we employ. In addition, the correlation between adjacent impedances was taken into account. Since our model is simpler, it is possible to solve the equation for c_0. In the case of small u, u_* is given by the solution of

$$\frac{4L}{a}W\left(\frac{\sqrt{\kappa}}{2}\frac{u_*}{u_M}\right)^2 = u_*^2\left[1+W\left(\frac{\sqrt{\kappa}}{2}\frac{u_*}{u_M}\right)\right]\,. \tag{2.125}$$

One can see that the crossing probability for both large and small values of u is concave down. It means that there are no discontinuities in the value of u_*, signifying a smooth transition from power-law behavior to exponential dependence. Indeed, this is the behavior that we observed for Ohmic conductance in our previous work [79].

To obtain $P_L(u)$ for intermediate values of u, we resort to numerical computation discussed below.

2.4.4 Numerical results

The crossing probability $P_L(u)$ is a cumulative distribution function (CDF) of the critical values of u. To obtain its form, we generate an ensemble of 10^5 systems at a particular L and T and find u_c for each one of them. From this array of u_c's we construct the crossing probability $P_L(u)$. We now explain how the critical value of u is extracted from each disorder realization.

For any system of length L, $P_L(u > 2L/a) = 1$, therefore we are only interested in $u < 2L/a$. This means that, according to Eq. (2.11), only the sites with $|\varepsilon| < 2LT/a$ are necessary in our computation. Thus, for each individual realization we generate n sites, where n is randomly extracted from the Poisson distribution with the mean given by $4L^2Tg/a$. This mean corresponds to the expected number of sites in the energy-position space for a system of length L with density g. These sites are then positioned, at random, within the allowed region in the energy-position space. At the ends of each sample we fix sites at $\varepsilon = 0$ in order to simulate the electrodes since we are looking for a path that connects them via localizes states inside the sample.

To determine u_c, we first note that it has to be between $u_{min} = 0$ and $u_{max} = 2L/a$. Next, we take a trial value of u_c: $u_{tr} = (u_{max} + u_{min})/2$ and check whether there is a path at this u_{tr}. It is done by only considering the sites with $|\varepsilon| \leq u_{tr}T$ to speed up the process and by constructing a resistance (cost) matrix between the sites. Following Eq. (2.11), if u_{ij} between any two sites is less than u_{tr}, make the resistance equal 1. Otherwise, make it infinite. We then use Dijkstra's algorithm to find the lowest-cost path between the electrodes. If the cost is finite, i.e., all resistances are below u_{tr}, the trial value is too high. On the other hand, infinite total cost implies that we underestimated u_c. In the first case, we need to look at lower values of u and redesignate $u_{max} = u_{tr}$. In the other case we call $u_{min} = u_{tr}$. From the new values of the bounds, we obtain a new u_{tr} and repeat the process fifteen times to estimate the u_c at which the first finite-resistance path

appears.

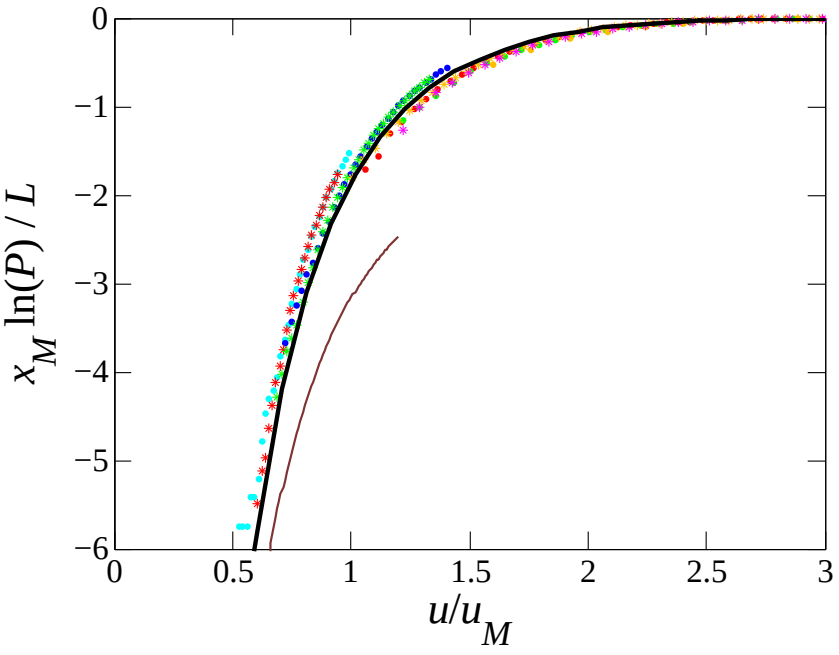

Figure 2.22: The collapse of the numeric results onto a common curve. Circles correspond to $L = 100a$; stars denote $L = 30a$. Different colors represent the temperatures ranging from $5 * 10^{-5}$ to $5 * 10^{-3}$ for $L = 100a$ and from 10^{-4} to 10^{-2} for $L = 30a$.

After we obtain all $P_L(u)$'s, we plot $x_M \ln(P_L)/L$ versus u/u_M, where $x_M = u_M a/2$, as seen in Fig. 2.22. Plotting data in this set of coordinates results in the collapse of data onto a common curve. We connect the low- and high-u behavior by the following interpolation formula:

$$P = 1 + \sum_{k=1}^{k_m} \frac{(-1)^k}{k!} e^{-\rho k} [\rho(l-k)]^{k-1} (k - k\rho + l\rho)\,, \tag{2.126}$$

where $l = \frac{2L}{ua}$, $\rho = \frac{1}{1+1.8\frac{u_M}{u}} \frac{u^2}{2u_M^2}$, and $k_m = \text{floor}[l]$. The deviation from the general curve for higher values of u results from the fact that the number of hops is not sufficiently large in our moderately long systems. The formula in Eq. 2.126 for different l and ρ comes from the crossing probabity of a 1D system without the energy coordinate. Here we simply replace the two variables to provide the interpolating fit.

In order to obtain the formula that provides a general curve, we turn our attention to a simplified toy model of the system in question. We consider a 1D system without energy of length L with radomly positioned localized states. The task is to compute the probability that the largest distance between any two neighboring sites is less than or equal to R. For a system with N hops the unnormalized probability is given by

$$Z_{N-1}(R,L) = g^{N-1}\int_0^R \prod_{i=1}^{N} dx_i \delta(L - \sum_{j=1}^{N} x_j)\,, \tag{2.127}$$

where x_i is the length of the ith hop. Taking the Laplace transform of Eq. (2.127) and integrating over x_i, one obtains

$$\tilde{Z}_{N-1}(R,s) = g^{N-1}\left(\frac{1-e^{-sR}}{s}\right)^N\,. \tag{2.128}$$

Performing the inverse Laplace transform and summing over all N gives the total $Z(L)$:

$$Z(L) = \sum_{N=1}^{\infty}\sum_{k=0}^{N}\frac{N(-1)^k[g(L-kR)]^{N-1}}{k!(N-k)!}\Theta(L-kR)\,. \tag{2.129}$$

To normalize the probability, we let $R > L$ and Eq. (2.129) gives e^{gL}. Since we expect the probability to be equal to unity at that point, we divide the expression by the exponential. Next, we introduce a change a variables $l = L/R$ and $\rho = gR$ to get:

$$P(l) = \sum_{N=1}^{\infty}\sum_{k=0}^{N}\binom{N}{k}\frac{(-1)^k[\rho(l-k)]^{N-1}e^{-\rho l}}{(N-1)!}\Theta(l-k)\,. \tag{2.130}$$

According to the Heaviside functions, the maximum value that k can attain is $k_{max} \equiv k_m = \text{floor}[l]$. All the terms with $k = 0$ add up to 1 which allows the total sum can be rewritten as:

$$P(l) = 1 + \sum_{k=1}^{k_m}\sum_{N=k}^{\infty}\binom{N}{k}\frac{(-1)^k[\rho(l-k)]^{N-1}e^{-\rho l}}{(N-1)!} \tag{2.131}$$

Summing the inside terms over N results in Eq. (2.126).

One can also proceed by summing Eq. (2.128) for all N:

$$\tilde{Z}(R,s) = \frac{\frac{(1-e^{-sR})}{s}}{1-\frac{g(1-e^{-sR})}{s}}\,. \tag{2.132}$$

This results in

$$P(R,L) = \frac{e^{-\rho l}}{2\pi i} \int_{\gamma - i\infty}^{\gamma + i\infty} ds \frac{\frac{(1-e^{-s})}{s}}{1 - \frac{\rho(1-e^{-s})}{s}} e^{sl} \,. \tag{2.133}$$

Applying the residue theorem, we get

$$P(R,L) = \frac{e^{-\rho l}}{\rho} \sum_{j=-\infty}^{\infty} e^{s_j l} \left[-\frac{k(s_j)}{k'(s_j)} \right] , \tag{2.134}$$

$$k(s) \equiv \frac{1 - e^{-s}}{s} , \tag{2.135}$$

where s_j are the roots of $k(s) = 1/\rho$. The contour if integration is shown in Fig. 2.23.

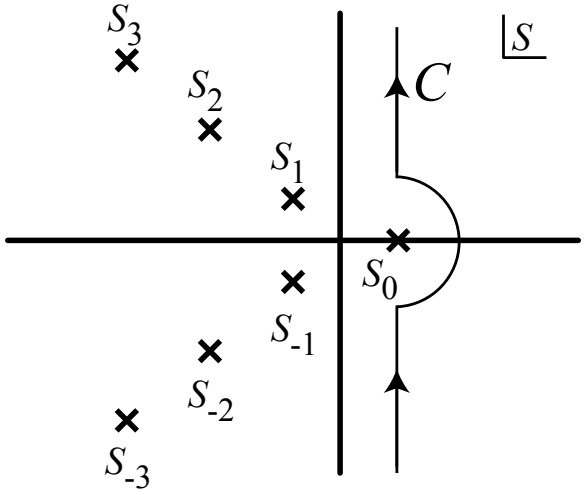

Figure 2.23: The contour used in Eq. (2.133). For $\rho \ll 1$, all the residues are negative. When ρ becomes sufficiently large, however, the dominating residue becomes positive and approaches ρ.

For large l the real root s_0 dominates and is given by

$$s_0 = \rho + W_n(-\rho e^{-\rho}) \,, \tag{2.136}$$

where $n = \Theta(\rho - 1) - 1$ and W_i is the Lambert function. Therefore

$$P(l) \simeq \frac{e^{-\rho l}}{\rho} e^{s_0 l} \left[-\frac{k(s_0)}{k'(s_0)} \right] = \frac{s_0 e^{l \frac{s_0 - \rho}{\rho}}}{\rho(1 - \rho + s_0)} \,. \tag{2.137}$$

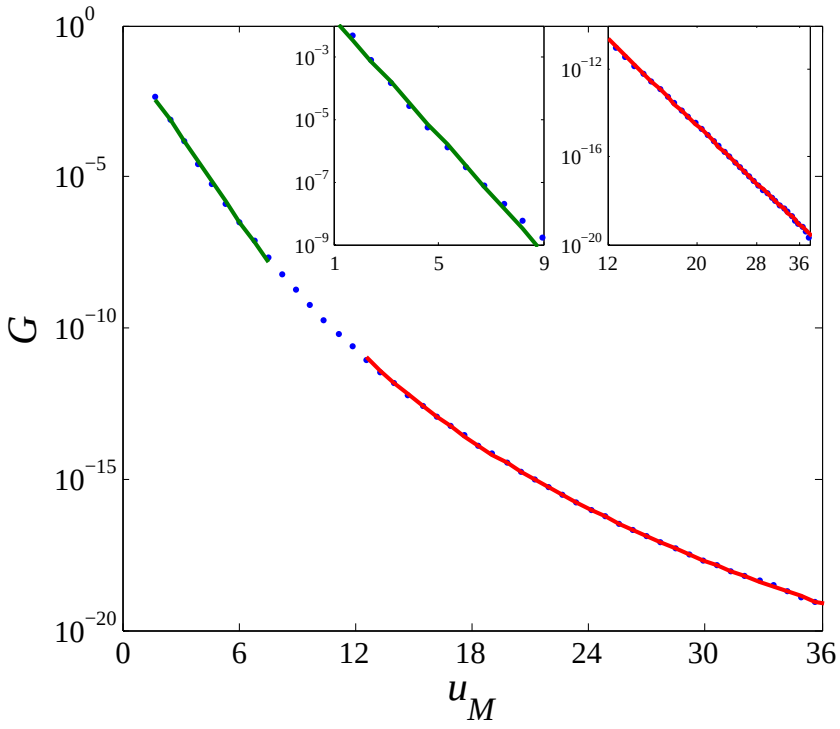

Figure 2.24: Dependence of G on T. The insets demonstrate the data individually in different axes to bring out the exponential and power-law natures of the dependence.

Having obtained the interpolation formula, we now construct the G-T curve. The average conductance is given by

$$\langle G \rangle = \int e^{-u} P(u) du \gg e^{-2L/a} , \tag{2.138}$$

where the inequality represents the many-hop requirement. To illustrate the result, we choose $L = 100a$ and plot the G-T curve in Fig. 2.24. It shows a smooth transition from a power-law-like behavior at high u_M to a stretched exponential at low ones. Thus, we have offered a plausible explanation for the seemingly irreconcilable T dependences of G.

2.4.5 Higher Dimensions

Unlike 1D, higher dimensions possess a percolation threshold u_c because of the presense of transverse physical dimension. In this section we provide qualitative analysis of the forms of $P_L(u)$ and $G(T)$.

At low values of u, the behavior of $P_L(u)$ is similar for all dimensionalities since the paths are rare and non-interacting. In effect, systems in higher dimensions behave as ensembles of individual wires with independent paths. The only difference in the computation arises from the presense of the transverse coordinates. For a detailed treatment of a 3D system see Ref. [92].

For the behavior of the crossing probability around the percolation threshold, we turn to earlier work. In particular, arguments for the stretched exponential form of the crossing probability have been given [14, 40, 66]:

$$P_L(u) \sim \exp(-L/\xi)\,, \tag{2.139}$$

where ξ is the correlation length. We define the typical hopping length $r_M \equiv \frac{1}{4} a u_M$. The correlation length of the network for $u \lesssim u_c$ is then given by

$$\xi \sim r_M |\epsilon|^{-\nu}\,, \tag{2.140}$$

where ν is the critical exponent and the percolation parameter ϵ is

$$\epsilon \equiv \frac{B - B_c}{B_c} = \left(\frac{u}{u_c}\right)^{d+1} - 1\,. \tag{2.141}$$

Below the percolation threshold, ξ can be understood as a typical size of a connected cluster. For $u > u_c$, on the other hand, it is the typical size of a region where bonds do not contribute to the network.

At very low values of u, only clusters consisting of single bonds are present in the system. Increasing u causes individual bonds to coalesce, forming larger clusters. Very rarely there appear collections of sites that span across the entire film. These clusters are fairly straight and unbranched, since introducing kinks and branching involves adding more bonds.

Going to higher values of u creates more conducting paths crossing the system and more branching, see Fig. 2.21. Since the number of open bonds is now higher, the paths are not necessarily straight. In addition, clusters within the bulk become connected to the conducting backbones, forming dangling bonds. These dangling bonds generally do not contribute to the conductance since they are not long enough to connect individual crossing paths.

Finally, at sufficiently high u's, dangling bonds reach neighboring backbones to allow transport between them. This results in the formation of a percolating network that spans the system, Fig. 2.21, meaning that $\xi \ll L$. As even larger values of u are considered, the network becomes denser as the percolating cluster absorbs smaller clusters.

Since low-u crossing probability for higher dimensions is similar to that of 1D systems, the conductance has a similar form for all dimensionalities. At high T, the conductance is determined by the percolation threshold and the details of the dimensional behavior are discussed below. The regime that connects the low- and high-T parts is described by

$$\ln G \sim u_M \left[1 - \left(u_M^2 \frac{a}{L}\right)^{\frac{1}{\nu-1}}\right] . \tag{2.142}$$

The difference in the high-T behavior stems from the distinct forms of $P_L(u)$ in the vicinity of the percolation threshold. It results from the values of the critical exponent ν in Eq. (2.140). Taking the derivative of Eq. (2.139) we get

$$\frac{dP_L(u)}{du} \sim P_L(u) \frac{L(d+1)u^d}{r_M u_c^{d+1}} |\epsilon|^{\nu-1} . \tag{2.143}$$

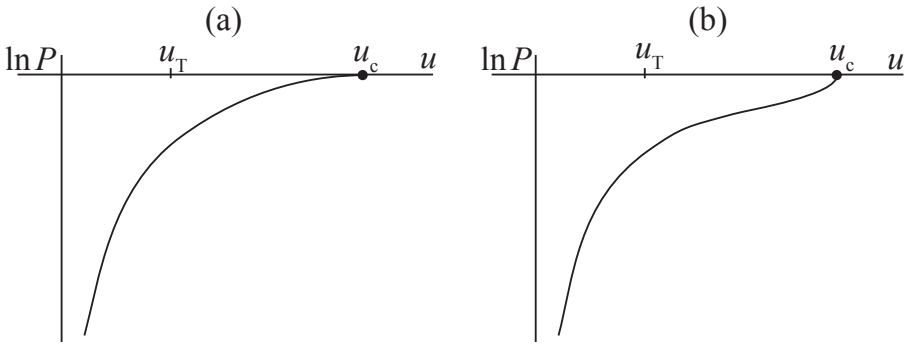

Figure 2.25: $P_L(u)$ for 2D, (a), and 3D, (b). Low-u regime is defined by Eq. (2.122); high-u part of the curve is given by Eq. (2.139). u_T denotes the resistance where the transition between the regimes occurs. A qualitative difference in the vicinity of u_c is apparent.

As $u \to u_c$, $\epsilon \to 0$ and for $\nu > 1$, as in 2D, the curve approaches unity horizontally. In the case of $\nu < 1$, as in 3D, the curve goes to 1 with infinite slope,

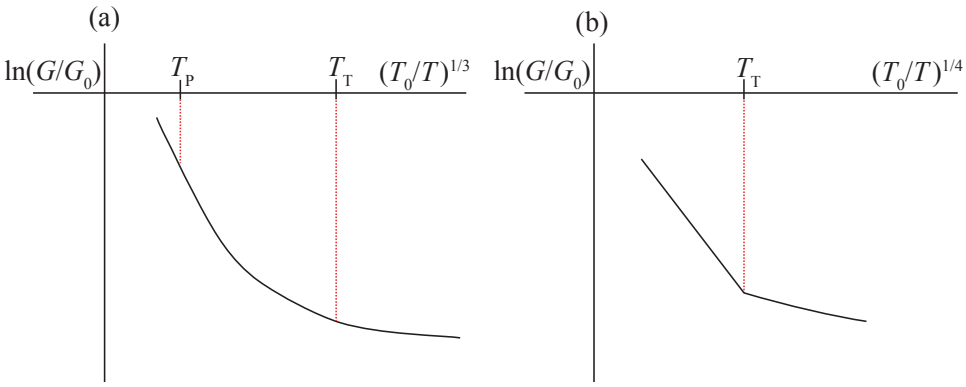

Figure 2.26: G as a function of T for 2D, (a), and 3D, (b). 3D plot shows an abrupt transition between the regimes, unlike 2D, where the transition is smooth.

see Fig. 2.25. This means that while in 2D $\ln[P_L(u)]$ is always concave down, in 3D the curve changes concavity. This results in different transitions between low- and high-T regimes depending on the dimensionality of the system.

Consider 2D first. Decreasing u_M causes the curve to be compressed horizontally, moving the maximum to the smaller values of u. For sufficiently high $T > T_p$, the maximum of the product of e^{-u} and $P_L(u)$ is at u_c. At this point, the conductance of the system is determined by the percolating network, per Mott law, rather than by rare events and becomes $\sim e^{-u_c}$. Since u_c scales linearly with u_M, Eq. (2.16), the logarithm of $G(T)$ varies linearly with decreasing u_M, see Fig 2.26(a). Since $P_L(u)$ is always concave down, the high-T regime smoothly transitions into the 1D-like behavior observed for $T < T_T$.

Similarly to 2D case, 3D also exhibits two distinct regimes: low-T behavior, reminiscent of 1D, and high-T percolation. Unlike 2D, however, the transition between the regimes is noticeably different due to the change of concavity of $P_L(u)$ in 3D. Since the slope of $P_L(u)$ is greater than 1 in the vicinity of u_c, when e^{-u} intersects it to the right of the inflection point, the maximum ends up at u_c. This means that there is an abrupt transition from the low-T regime to the high-T behavior in contrast to the gradual change observed in 2D, see Fig. 2.26(b).

2.4.6 Discussion and Conclusion

In our study we used the simplified formula for u and neglected prefactors. An earlier work [35] treated a specific case of transport involving three hops. There the authors took into account the lack of phonons in the transition between the electrodes and the sample to obtain more accurate results. They demonstrated a power-law dependence of Ohmic conductance on temperature with the power of 4/3. This result indicates that the power-law behavior can indeed arise in disordered systems usually treated according to Mott formalism.

As is obvious from Ref. [35], knowing the exact number of hops N in a path permits one to determine the dependence of conductance on temperature. Unfortunately, in reality it is impossible to guarantee that the transport through a system involves a specific number of hops. Therefore, N is not the ideal variable to be used to determine the G-T behavior of an ensemble. This led us to adopt u as the principal variable in our approach since it bears a direct connection with the resistance.

In this section, we have investigated the dependence of Ohmic conductivity on temperature in disordered quasi-1D materials. In particular, we have demonstrated that experimentally observed exponential and power-law dependences can arise in this model. We also used numerical computations and theory of percolation to probe into the region that lies between the two traditionally considered regimes. The significance of our results is due to (1) showing the applicability of percolation theory to the problem at hand and (2) resolving the question of two seemingly incompaticle T dependences.

Our results provide a good explanation for the behavior observed in systems with a large number of channels [106, 88, 96, 108]. However, individual wires [56] and similar systems, like graphene nanoribbons [36], exhibit significant mesoscopic fluctuations. Therefore, our method is not applicable for them and further theoretical analysis is required. Nonetheless, our results are not limited to ensembles of 1D wires. What we have shown here can be extended to 2D ribbons (and lateral junctions) and 3D thin films. This is because we have shown that systems regardless of their dimensionality undergo a similar network evolution with the variation

of u.

Examples of 2D systems that can be studied using our method include important structures such as GaAs devices [41] and bilayer graphene p-n junctions [69]. Unfortunately the range of T and the sample width were too narrow in Refs. [41, 69] to apply our analysis. Extending the parameter range would allow one to assess the applicability of the theory better. Finally, in 3D our approach describes thin films [103, 20]. Reference [103] indeed demonstrates the Mott behavior transitioning to a power-law-like dependence with decreasing temperature. In applying our method to Ref. [20] one would needs to keep in mind that the proper model would need to use exponential-like DOS. In addition, it should also address changes in film morphology and doping level with thickness. However, qualitatively there is an agreement as the thinnest films studied do display a sharp change from strong to weak T-dependence below some T, which we predict.

Possible future work using our approach may involve Coulomb interaction effects, non-constant density of states, and non-Ohmic transport.

This chapter includes parts of the following published works: "Hopping transport in systems of finite thickness or length"(PRB, 2011); "Apparent Power-Law Behavior of Conductance in Disordered Quasi-One-Dimensional Systems" (PRL, 2010); "Numerical studies of variable-range hopping in one-dimensional systems" (PRB 2009) by A. S. Rodin and M. M. Fogler.

Chapter 3

Plasmons in Graphene

This chapter deals with plasmonic effects in graphene. We begin by presenting a very brief overview of graphene. Latter sections are dedicated to elucidating the plasmonic phenomena.

3.1 Graphene Fundamentals

Everyone who has ever held a pencil has encountered graphene. The lead inside the pencil is made of graphite, which is an allotrope of carbon. Bulk graphite is composed of individual, single-atom thick layers, held together by weak van der Waals force. These layers are composed of covalently bound carbon atoms, arranged in a hexagonal lattice. It is these individual sheets of carbon that we refer to as graphene. When one moves graphite against paper, these layers are shed off the lead, leaving a dark trail. As it turns out, there are applications for graphene which extend beyond taking notes.

Even though graphite has been used for marking and writing for over four hundred years, it was only in 2004 that graphene was isolated. [68] Immediately, the attention of the scientific community was turned to this newly discovered exotic material. There are a number of properties that make graphene very exciting. First and foremost, it is a truly two-dimensional material. Prior to its discovery, it was suspected that such a system would be unstable in three dimensions. Nevertheless, it is stable enough to not only exist, but also be stretched and twisted without

breaking. In addition, it is of great academic interest due to its peculiar linear dispersion (which we will discuss shortly). Finally, graphene's electronic properties have stimulated a significant amount of research in applied science.

Graphene's properties are strongly tied to its structure. Every carbon atom in the 2D lattice is bound to three other carbons. The bonds are forms by the hybridization of s and p orbitals. Since the bonds are coplanar, the resulting hybridized orbital is sp^2, which mixes the one s and two of the p orbitals. This leads to the formation of $a = 1.42$ Å σ bonds between carbon atoms. The remaining p orbital forms covalent bonds with the neighboring atoms, resulting in a π band. Every carbon atom contributes four electrons, three of which participate in the σ bonds, leaving one in the remaining p orbital. This results in half-filling of the π band in a pure material.

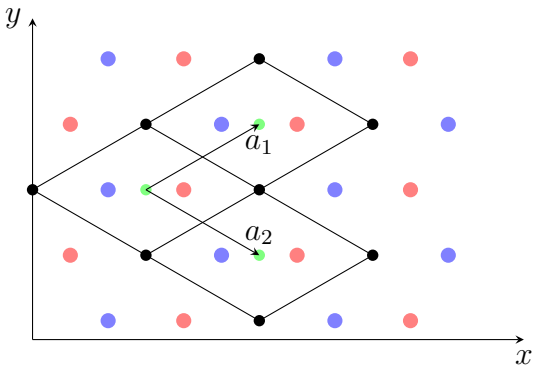

Figure 3.1: The triangular lattice with two atoms A and B(red and blue) per unit cell. The lattice vectors a_1 and a_2 are $a(3, \pm\sqrt{3})/2$.

Hexagonal lattices are not Bravais lattices. Instead, one can visualize them as triangular lattices with two atoms (A and B) per unit cell, see Fig. 3.1. Naturally, the reciprocal lattice is also triangular, as is shown in Fig. 3.2.

The system is typically analyzed using the tight-binding model with the Hamiltonian given by

$$H = -\gamma_0 \sum_{\text{n.n.}} \left[a_i^\dagger b_j + h.c. \right] + \mu \sum_i \left[a_i^\dagger a_i + b_i^\dagger b_i \right] , \tag{3.1}$$

where the summation is over the nearest neighbors and $\gamma_0 \approx 2.8$ eV. Note that while we are including only the nearest neighbor hopping, it is possible to include

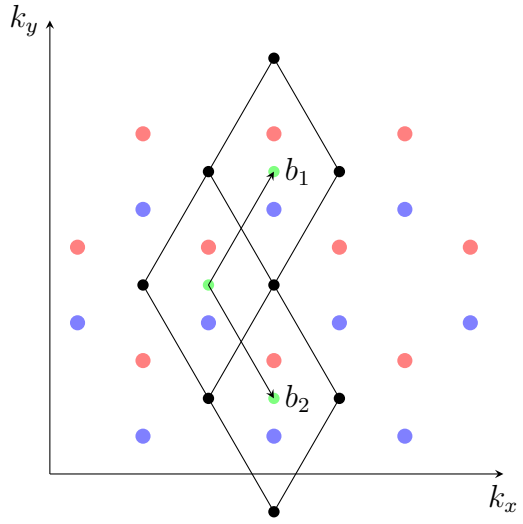

Figure 3.2: Reciprocal lattice with unit cells shown. The lattive vectors are b_1 and $b_2 = (2\pi/3a, \pm 2\pi/\sqrt{3}a)$.

hopping terms for the next-nearest neighbor. The contribution from the other term, however, is much smaller and we do not take it into account.

To obtain the dispersion relation of the system, we go to the Fourier space and transform the operators as $a_i^\dagger = \sum_k e^{-i\vec{k}\cdot\vec{r}} a_k^\dagger$. Now, notice that the nearest neighbors for any point A (or B) are three sublattice B (or A) points. One of them lies in the same unit cell as the original site and the other two are in the two unit cells separated by the lattice vectors $a(3, \pm\sqrt{3})/2$. From this we can write the Hamiltonian as

$$H = \sum_k (a_k^\dagger \; b_k^\dagger) \begin{pmatrix} -\mu & f_k \\ f_k^* & -\mu \end{pmatrix} \begin{pmatrix} a_k \\ b_k \end{pmatrix} , \tag{3.2}$$

$$\begin{aligned} f_k =& \gamma_0 \left\{ 1 + \exp\left[ia\left(\frac{3k_x}{2} + \frac{\sqrt{3}k_y}{2} \right) \right] + \exp\left[ia\left(\frac{3k_x}{2} - \frac{\sqrt{3}k_y}{2} \right) \right] \right\} \\ =& \gamma_0 \left\{ 1 + 2\cos\left[\frac{\sqrt{3}ak_y}{2} \right] \exp\left[i\frac{3ak_x}{2} \right] \right\} . \end{aligned} \tag{3.3}$$

Diagonalizing the Hamiltonian, we get the energies

$$\begin{aligned}\xi_k^b &= -\mu + b\sqrt{f_k f_k^*} = -\mu + b\varepsilon_k \\ &= -\mu + b|\gamma_0|\sqrt{1 + 4\cos\left(\frac{3ak_x}{2}\right)\cos\left(\frac{\sqrt{3}ak_y}{2}\right) + 4\cos^2\left(\frac{\sqrt{3}ak_y}{2}\right)}\,. \end{aligned} \tag{3.4}$$

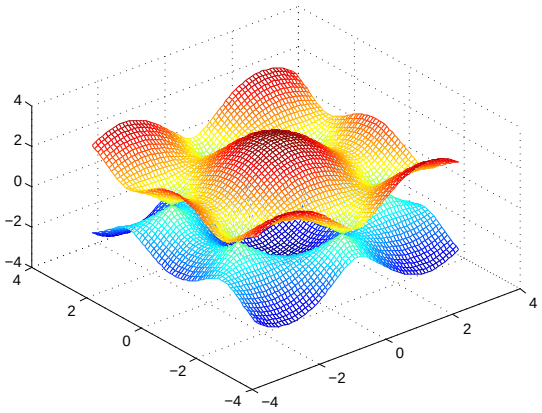

Figure 3.3: The band structure of graphene.

Let us now investigate the dispersion relation close to $\xi_k^b = 0$. We denote $k_x = k\cos\theta$ and $k_y = k\sin\theta + 4\pi/(3a\sqrt{3})$ and expand to the first order in k. This casts the dispersion relation into a radially symmetric form:

$$\xi_k^b = -\mu + b\underbrace{|\gamma_0|\frac{3a}{2}}_{\hbar v_F}k\,, \tag{3.5}$$

where we have introduced the Fermi velocity $v_F = 10^8$cm/s. We have thus shown that at low energies massive electrons follow the dispersion relation for massless particles. The point $k = 0$ is referred to as the Dirac point.

Using the linear approximation, one writes down the Dirac Hamiltonian as

$$H = \sum_k (a_k^\dagger\ b_k^\dagger)\begin{pmatrix} -\mu & \hbar v_F k e^{-i\theta_k} \\ \hbar v_F k e^{i\theta_k} & -\mu \end{pmatrix}\begin{pmatrix} a_k \\ b_k \end{pmatrix}. \tag{3.6}$$

Going back to the first quantization, we find that the eigenstates of the two-by-two matrix are

$$\psi_k = \frac{1}{\sqrt{2}}\begin{pmatrix} 1 \\ \pm e^{i\theta_k} \end{pmatrix}, \tag{3.7}$$

corresponding for conduction and valence bands, respectively.

Before we move on, there is something else worth mentioning. Since there are two atoms inside each unit cell, there will be two inequivalent Dirac points inside each Brilloin zone, see Fig. 3.2. The simplest consequence of this is the introduction of a two-fold degeneracy. Therefore, whereas usually the degeneracy of the system would be equal to two (due to the spins), here it is equal to four (spins and the so-called valley degeneracy).

This concludes our very rudimentary overview of graphene basics. In the next section, we will talk about collective excitations in graphene. Any additional concepts will be introduced as needed. For an excellent review of graphene, see Ref. [65].

3.2 Graphene Plasmonics

Plasma oscillation in materials is a well-known phenomenon. These oscillations arise in response to a perturbation of the equilibrium charge distribution. Coulomb interaction creates a restoring force that depends on the electronic properties of the material. Therefore, the modes of the oscillation are intimately connected to the band structure of the system.

These charge oscillations are not only exciting from the academic point of view, but also offer a range of potential applications. First and foremost, plasmonics can be used in atomic and molecular sensors. Since the oscillation modes depend on the electronic structure of a material, adsorption of foreign atoms or molecules will alter the modes which results in the change of absorption and emission peaks. In addition, plasmonic materials are currently investigated for their use in computer chips as they can work at higher frequencies compared to traditional electronics. Finally, photovoltaics can benefit from plasmon resonance that can improve the absorption of solar cells.

Our current project deals with observing plasmonic behavior in graphene, bringing together the exciting new material with the rapidly-growing field of plasmonics. We start by giving a brief overview of particle-hole excitations in graphene

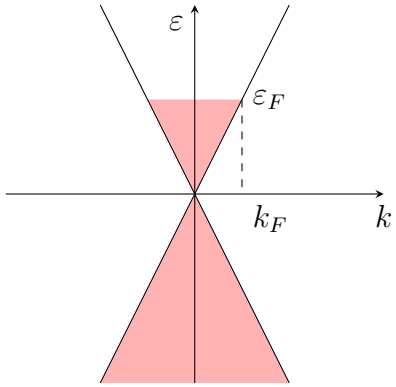

Figure 3.4: Electron-doped graphene. Shaded energies are filled, while the unshaded energy states are empty.

and then dedicating the rest of this section to plasmons in 2D in general and graphene in particular.

3.2.1 Particle-Hole Excitations

Consider an electron-doped graphene system. In this system, all states with negative energies are filled, while the positive states are filled up to a certain energy, referred to as the Fermi energy, ε_F, see Fig. 3.4. The assumptions that are made here are that $\gamma_0 \gg \varepsilon_F \gg k_B T$. This allows us to use the linearized version of the problem and also to set the temperature of the system to zero.

In such a system, it is possible to create particle-hole excitations. These excitations are formed when an electron from one of the filled states gets kicked up to one of the empty states, which invariably lie in the conduction band. If an electron comes from the conduction band, such a process is called intra-band; otherwise, it is referred to as interband.

Let us start with the intra-band processes, see Fig. 3.5. The excitations are created by a photon of energy ε_P and momentum $\vec{q}$. Since the electron must always remain on the energy-momentum cone, we have limits on the allowed values of $\vec{q}$. If an electron moves from energy $\varepsilon = \hbar v_F k$ to $\varepsilon' = \hbar v_F k'$, the minimum momentum that can move it there is $q_{\min} = k' - k = \varepsilon_P/(\hbar v_F)$, parallel to $\vec{k}$. The largest q, on the other hand, would come into play if we first reflected $\vec{k} \to -\vec{k}$ and then moved

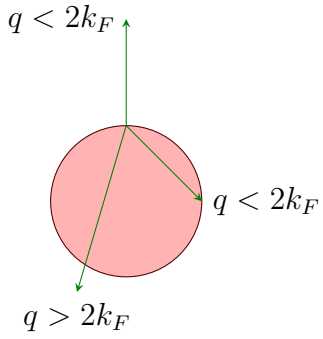

Figure 3.5: Intra-band transitions

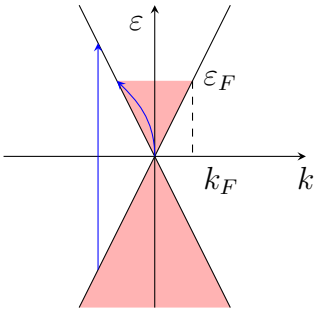

Figure 3.6: Inter-band transitions

it up by $\varepsilon_P/(\hbar v_F)$. This means that

$$\varepsilon_P/(\hbar v_F) \leq |q| \leq 2k + \varepsilon_P/(\hbar v_F)\,. \tag{3.8}$$

Since the largest possible momentum k is k_F, we insert it on the right-hand side of the above inequality.

Next, we look at the inter-band transitions, shown in Fig. 3.6. In this case, the minimum $\varepsilon_P = \varepsilon_F$. However, for such a transition to take place, we need $q = k_F$. On the other hand, for $q = 0$ transitions, the minimum energy is $2\varepsilon_F$. Putting together what we know about inter- and intraband excitations, we obtain a diagram that shows the allowed transitions, see Fig. 3.7.

Notice the empty triangle at the left part of the Figure. This is the region where particle-hole excitations are forbidden due to energy and momentum conservation. Thus, only collective excitations can occur in this range of parameters. These collective excitations appear in response to the external potential, which is

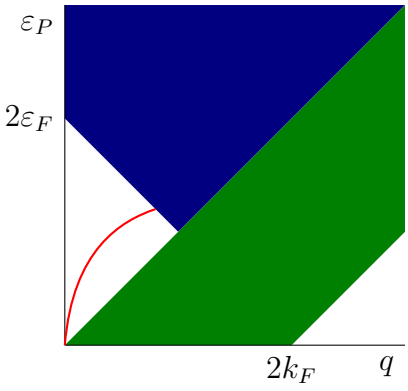

Figure 3.7: Particle-hole excitation. Green region corresponds to intra-band processes; blue region is inter-band. The red line is the plasmon branch, discussed below.

connected to the total potential by the equation

$$\phi_{\text{ext}}(q,\omega) = \varepsilon(q,\omega)\phi_{\text{tot}}(q,\omega)\,, \tag{3.9}$$

where $\varepsilon(q,\omega)$ is the dielectric function. It is clear from this expression that if $\varepsilon(q,\omega) \to 0$, then the total potential can oscillate in the absence of the external potential. This is precisely what we mean by collective excitations. Therefore, what one needs to obtain is the formula for the dielectric function.

Fortunately, this has already been done using the Random Phase Approximation (RPA) formalism. [100] RPA is based on the creation and subsequent annihilation of electron-hole pairs by a photon travelling through the system. The important feature of RPA is that it neglects the interactions between charges which would lead to energy renormalization and a finite lifetime of the excitations. Following every annihilation, the photon is re-emitted with the same momentum as it started with. On its path, it can temporarily excite any number of electron-hole pairs, but only one at a time. Summing up the contributions from all these possible paths yields the RPA dielectric function

$$\varepsilon^{\text{RPA}}(q,\omega) = 1 - \tilde{V}(q)\chi(q,\omega)\,, \tag{3.10}$$

where $\chi(q,\omega)$ is the polarizability and $\tilde{V}(q)$ is the Coulomb interaction. The polarizability function is typically computed using Feynman diagrams, however, it is also possible to do so directly without invoking Green's functions.

Consider a system with particle density $\rho(r,t)$. At time t_0 and external perturbing potential $\phi_{\text{ext}}(r,t)$ is switched on, leading to the perturbing Hamiltonian

$$H_{1I}(t) = \int dr \rho(r,t)\phi_{\text{ext}}(r,t)\,. \tag{3.11}$$

Note that we are working in the interaction picture. This means that, according to Kubo formalism, for any operator A the thermal average at times $t > t_0$ is

$$\langle A(t)\rangle = \langle A(t_0)\rangle_0 - i\int_{t_0}^{t} dt' \langle [A_I(t), H_{1I}(t')]\rangle_0\,. \tag{3.12}$$

The averages on the right-hand side are performed over the eigenstates of the original Hamiltonian without the perturbation.

$$\begin{aligned}\langle \delta\rho(r,t)\rangle =& \langle \rho(r,t)\rangle - \langle \rho(r)\rangle_0 \\ =& \int_{t_0}^{t} dt' \int dr' \phi_{\text{ext}}(r',t') \underbrace{\left\{ i\langle [\rho(r',t'),\rho(r,t)]\rangle e^{-\gamma(t-t')} \right\}}_{\chi(r-r';t-t')}\,.\end{aligned} \tag{3.13}$$

The factor $e^{-\gamma(t-t')}$ with $\gamma > 0$ is introduced to ensure convergence for $t \gg t'$. Generally, one takes $\gamma \to 0^+$ at the end of the calculation; however, it is possible to introduce damping by keeping γ finite. We assume that the material is isotropic and, therefore $\chi(r',r;t-t') = \chi(r-r',;t-t')$.

We start the calculation by going to the Fourier space:

$$\begin{aligned}\chi(q;t-t') &= i\int dr \langle [\rho(r',t'),\rho(r,t)]\rangle e^{-iq(r-r')} e^{-\gamma(t-t')} \\ &= \frac{i}{V^2}\int dr \sum_{q_1,q_2} \langle [\rho(q_1,t'),\rho(q_2,t)]\rangle e^{-iq(r-r')} e^{iq_1 r'} e^{iq_2 r} e^{-\gamma(t-t')} \\ &= \frac{i}{V^2}\int dr \sum_{q_1,q_2} \langle [\rho(q_1,t'),\rho(q_2,t)]\rangle e^{ir(q_2-q)} e^{-ir'(q_1+q)} e^{-\gamma(t-t')} \\ &= \frac{i}{V}\langle [\rho(-q,t'),\rho(q,t)]\rangle e^{-\gamma(t-t')}\,.\end{aligned} \tag{3.14}$$

The logic behind the last line is that the answer should not depend on r', setting $q_1 = -q$. In addition, the oscillatory integral along r only gives a non-zero result V when $q_2 = q$.

The density operator is defined as

$$\rho(r) = \Psi^\dagger(r)\Psi(r) = \frac{1}{2}\sum_{k_1,k_2}\sum_{s,s'=\pm} c^\dagger_{k_1,s}c_{k_2,\,s'}\left(1, se^{-i\theta_{k_1}}\right)\begin{pmatrix}1\\ s'e^{i\theta_{k_2}}\end{pmatrix}e^{i(\vec{k}_2-\vec{k}_1)\cdot\vec{r}}\,. \quad (3.15)$$

We introduce $\vec{q} = \vec{k}_2 - \vec{k}_1$. Renaming $k_1 \to k$, one obtains

$$\rho(q) = \sum_k \sum_{s,s'=\pm} c^\dagger_{\vec{k},s}c_{\vec{k}+\vec{q},s'}\frac{1}{2}\left(1 + s\,s'e^{i(\theta_{\vec{k}+\vec{q}}-\theta_{\vec{k}})}\right)\,. \quad (3.16)$$

The creation and annihilation operators evolve in time. This time evolution only depends on the unperturbed Hamiltonian in our linear response theory. Since the Hamiltonian is diagonal in momentum space, $H_0 = \sum_s \sum_k \xi^s_k c^\dagger_{k,s}c_{k,s}$ (with $s = \pm$ as the band index), this yields

$$\begin{aligned}\dot{c}_{q,s}(t) &= i\sum_{s'}\sum_k [\xi^{s'}_k c^\dagger_{k,s'}c_{k,s'}, c_{q,s}(t)]\\ &= e^{iH_0t}i\sum_{s'}\sum_k [\xi^{s'}_k c^\dagger_{k,s'}c_{k,s'}, c_{q,s}]e^{-iH_0t} = -i\xi^s_q c_{q,s}(t)\,, \quad (3.17)\\ c_{q,s}(t) &= c_{q,s}e^{-i\xi^s_q t}\,. \quad (3.18)\end{aligned}$$

Finally, we obtain the form of $[\rho(-q,t'),\rho(q,t)]$:

$$\begin{aligned}[\rho(-q,t'),\rho(q,t)] = \sum_{k_1,k_2}\sum_{s_1,s'_1,s_2,s'_2=\pm} &[c^\dagger_{k_1,s_1}c_{k_1-q,s'_1}, c^\dagger_{k_2,s_2}c_{k_2+q,s'_2}]\times\\ &\exp\left[i\left(\xi^{s_1}_{k_1} - \xi^{s'_1}_{k_1-q}\right)t'\right]\exp\left[i(\xi^{s_2}_{k_2} - \xi^{s'_2}_{k_2+q}\right)t\Big]\times\\ &\frac{1}{4}\left(1 + s_1\,s'_1e^{i(\theta_{k_1-q}-\theta_{k_1})}\right)\left(1 + s_2\,s'_2e^{i(\theta_{k_2+q}-\theta_{k_2})}\right)\,. \quad (3.19)\end{aligned}$$

The commutator of the creation/annihilation operators gives

$$[c^\dagger_{k_1,s_1}c_{k_1-q,s'_1}, c^\dagger_{k_2,s_2}c_{k_2+q,s'_2}] = c^\dagger_{k_2+q,s_1}c_{k_2+q,s'_2}\delta_{s'_1,s_2} - c^\dagger_{k_2,s_2}c_{k_2,s'_1}\delta_{s_1,s'_2}\,. \quad (3.20)$$

Since the commutator will be sandwitched between the eigenstates of H_0, the subindeces of the creation and annihilation operator pairs have to be identical to give a non-zero contribution.

Plugging this result back into the expression above gives us

$$\begin{aligned}[\rho(-q,t'),\rho(q,t)] = \sum_k \sum_{s_1,s_2=\pm} &(c^\dagger_{k+q,s_1}c_{k+q,s_1} - c^\dagger_{k,s_2}c_{k,s_2})\times\\ &\exp\left[i(\xi^{s_2}_k - \xi^{s_1}_{k+q})(t-t')\right]\frac{1 + s_1s_2\cos(\theta_k - \theta_{k+q})}{2}\,. \quad (3.21)\end{aligned}$$

Taking the thermal average turns the creation-annihilation products into Fermi-Dirac distributions. Finally, Fourier transfoming the result with respect to time leaves us with the formula for polarizability:

$$\chi(q,\omega) = \frac{g}{V}\sum_{k}\sum_{s,s'=\pm}\frac{n_F(\xi_k^{s'}) - n_F(\xi_{|k+q|}^{s})}{\xi_k^{s'} - \xi_{|k+q|}^{s} + \omega + i\gamma}\frac{1 + s's\cos(\theta_k - \theta_{k+q})}{2}\,, \tag{3.22}$$

where we have added a factor $g = 4$ to account for the degeneracy. After all the summations have been performed for $T = 0$, [100] the result is

$$\chi(q,\omega) = \chi_0(q,\omega) + \Delta\chi(q,\omega)\,, \tag{3.23}$$

$$\chi_0(q,\omega) = -i\pi\frac{F(q,\omega)}{\hbar^2 v_F^2}\,, \tag{3.24}$$

$$\Delta\chi(q,\omega) = -\frac{g\mu}{2\pi\hbar^2 v_F^2} + \frac{F(q,\omega)}{\hbar^2 v_F^2}\left[G\left(\frac{\omega+2\mu}{q}\right) - G\left(\frac{\omega-2\mu}{q}\right)\right]\,, \tag{3.25}$$

$$G(x) = i\left[x\sqrt{1-x}\sqrt{1+x} - \arccos x\right]\,, \tag{3.26}$$

$$F(q,\omega) = \frac{g}{16\pi}\hbar v_F^2 q^2\frac{-i}{\sqrt{v_F q - \omega}\sqrt{v_F q + \omega}}\,, \tag{3.27}$$

$$\omega = \Re\left(\omega\right) + i\gamma\,. \tag{3.28}$$

From the expression above, it is possible to show that for vanishing γ, the imaginary part of the dielectric function inside the triangle in Fig. 3.7 goes to zero. In addition, there exists a branch where $\varepsilon \to 0$. This means that not only there exist collective excitations, but also that the dissipation in certain parameter range is zero. This last conclusion is, of course, based on the RPA approximation used here. In reality, to observe dissipation and, therefore, finite lifetime of excitations, one needs to go beyond RPA.

Let us now use real numbers in order to demonstrate the theory in action. For a plasmonic mode to exist, the reflecton coefficient $\beta = 1 - 2/[\varepsilon^{\mathrm{RPA}}(\varepsilon^{\mathrm{RPA}} + 1)]$ must go to infinity. This occurs when $\varepsilon^{\mathrm{RPA}} \to 0$, as we already know. By plotting the imaginary part of β one can see the plasmonic branch assuming that $\gamma \neq 0$. Considering the chemical potential $\mu/hc = 900\,\mathrm{cm}^{-1}$, we plot the imaginary part of β for a range of ω and q in Fig. 3.8.

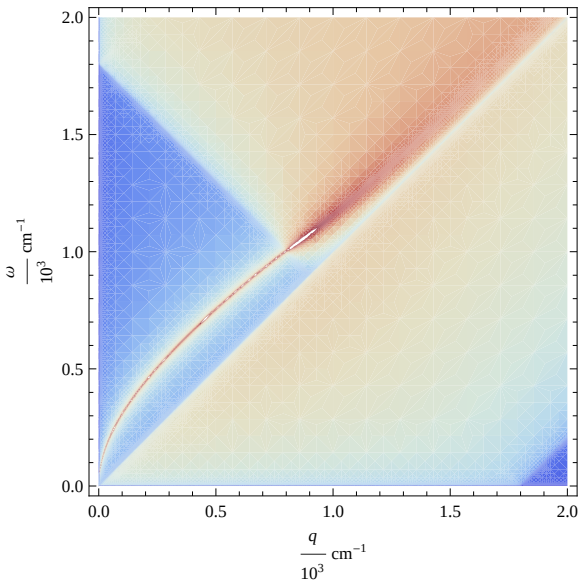

Figure 3.8: Imaginary part of the reflection coefficient for $\mu/hc = 900\,\mathrm{cm}^{-1}$ showing a plasmon branch.

Low-q limit

In our study, we are primarily interested in the long-wavelength behavior. Therefore, we investigate the behavior of the polarizability and the dielectric constant in the limit of low q. We begin by expanding the cosine to the leading order in q:

$$\begin{aligned}
\chi(q,\omega) &\approx \frac{g}{V}\sum_k \sum_{s,s'=\pm} \frac{n_F(\xi_k^{s'}) - n_F(\xi_{|k+q|}^{s})}{\xi_k^{s'} - \xi_{|k+q|}^{s} + \omega + i\gamma} \frac{1 + s's - s's\frac{q^2\sin^2\theta_k}{2k^2}}{2} \\
&\approx \frac{g}{V}\sum_k \left[\frac{n_F(\xi_k^-) - n_F(\xi_k^+)}{\xi_k^- - \xi_k^+ + \omega + i\gamma} + \frac{n_F(\xi_k^+) - n_F(\xi_k^-)}{\xi_k^+ - \xi_k^- + \omega + i\gamma}\right] \frac{\frac{q^2\sin^2\theta_k}{2k^2}}{2} \\
&+ \frac{g}{V}\sum_k \frac{n_F(\xi_k^+) - n_F(\xi_{|k+q|}^+)}{\xi_k^+ - \xi_{|k+q|}^+ + \omega + i\gamma} \\
&\approx \frac{gq^2}{V}\sum_k \left[\frac{1-\theta(\mu-k)}{-2k+\omega} + \frac{\theta(\mu-k)-1}{2k+\omega}\right] \frac{\sin^2\theta_k}{4k^2} + \frac{\cos^2\theta_k \delta(\mu-k)}{\omega^2} \\
&= \frac{gq^2}{(2\pi)^2}\int_0^{2\pi} d\theta_k \int_{\mu-0}^{\infty} dk \left[\frac{1}{-2k+\omega} - \frac{1}{2k+\omega}\right] \frac{\sin^2\theta_k}{4k} + k\frac{\cos^2\theta_k\delta(\mu-k)}{\omega^2} \\
&= \frac{\pi g q^2}{(2\pi)^2}\left[\frac{\mu}{\omega^2} - \frac{1}{4\omega}\ln\frac{2\mu+\omega}{2\mu-\omega}\right]. \qquad (3.29)
\end{aligned}$$

From the expression above, using the bare Coulomb interaction $\tilde{V}(q) = 2\pi e^2/\kappa q$ we obtain the dielectric function:

$$\varepsilon^{\mathrm{RPA}}(q,\omega) \approx 1 - \frac{e^2}{\kappa}\frac{gq}{2}\frac{\mu}{\hbar^2\omega^2}\,, \tag{3.30}$$

where we have assumed that $\mu \gg \omega$ and dropped the logarithmic term. Setting the expression equal to zero gives the plasmonic dispersion:

$$\omega^2(q) = \frac{2e^2}{\kappa\hbar^2}\,|\mu|q\,, \tag{3.31}$$

in agreement with the literature. [100, 65]

The conductivity $\sigma(q,\omega)$ of a 2D system such as graphene is related to its polarization function $\chi,\omega)$ by $\sigma(q,\omega) = ie^2(\omega/q^2)\chi(q,\omega)$. In the low-$q$ limit, the RPA approximation gives the following formula for the conductivity:

$$\sigma(\omega) = \frac{i}{\pi}\frac{e^2}{\hbar}\left[\frac{1}{\bar{\omega}} - \frac{1}{4}\ln\left(\frac{2+\bar{\omega}}{2-\bar{\omega}}\right)\right]\,, \quad \bar{\omega} = \frac{\hbar\omega}{\mu}\,. \tag{3.32}$$

As one can easily see, in the $q \ll \omega/v$ limit, the conductivity becomes independent of the momentum q. The disappearance of the q-dependence means that quasiparticles perceive the perturbing electric field as locally uniform. This is because the quasiparticle displacement $2\pi v/\omega$ over the time period of the field is much smaller than its wavelength $2\pi/q$.

If, in addition to $q \ll \omega/v$, the condition $\hbar\omega \ll \mu$ is also met, so that $\bar{\omega} \ll 1$, Eq. (3.32) reduces to the Drude-like formula

$$\sigma(\omega) = \frac{e^2}{\pi\hbar^2}\frac{\mu\tau}{1 - i\Re[\omega]\tau}\,, \tag{3.33}$$

where $\tau = \gamma^{-1}$ is the scattering time.

3.2.2 General Plasmon Equation

As was shown, plasmons can be excited by an external time-varying electric potential. We have derived the long-wavelength plasmonic dispersion using polarizability and charge-charge correlation. This section will focus on an alternative, more physically transparent derivation of long-wavelength plasmons. We

demonstrate that oscillatory behavior can be obtained from continuity equation, Ohm's law, and Coulomb's law in a straightforward fashion. Since this chapter is dedicated to graphene, we will only discuss plasmons that are confined to two dimensions. The total in-plane potential is the sum of the external and the induced ones:

$$U = U_{\text{ext}} + U_{\text{ind}} \,. \tag{3.34}$$

If the characteristic variations of the in-plane electric field $\vec{E} = -\nabla U$ occur on length scales L longer than the Fermi wavelength and additionally $v_F/L \ll \omega$, the conductivity of graphene can be treated as momentum-independent. In this case we have the following relations:

$$\nabla \vec{j} = -ie\omega n \,, \quad \vec{j} = -\sigma \nabla U \,, \tag{3.35}$$

$$\begin{aligned} -eU_{\text{ind}}(x,y,z) &= \int V(x-x',y-y',z-z')n(x',y',z')dx'\,dy'\,dz' \\ &\equiv \hat{V} n(x,y,z) \,. \end{aligned} \tag{3.36}$$

Above, $\vec{j}$ is the two-dimensional (2D) current density, n is the 2D electron density, $V(x,y,z)$ is the interaction potential (either bare e^2/r or screened Coulomb potential), and $\hat{V}$ is the corresponding integral operator. Since all the charge variation occurs in the x-y plane, we will drop the z component. This entails

$$U_{\text{ext}}(x,y) = U - \hat{V}\left[\nabla\left(\frac{i\sigma}{e^2\omega}\nabla U\right)\right] \,, \tag{3.37}$$

which is similar to a wave equation with the driving function $U_{\text{ext}}(x,y)$. Note that if the static density n_0 is a function of position, then so is the conductivity σ. Hence, it cannot be moved to the left of the first gradient. However, it is convenient to write σ in terms of the Drude weight, Eq. (3.32)

$$\sigma = \frac{iD}{\omega} \,. \tag{3.38}$$

The equation for U becomes

$$U_{\text{ext}}(x,y) = U + \hat{V}\left[\nabla\left(\frac{D}{e^2\omega^2}\nabla U\right)\right] \,, \tag{3.39}$$

Consider first this equation in the simplest case where $D(x,y) = \text{const}$, the system is infinite, and $U_{\text{ext}}(x,y)$ vanishes. The solution is then a plane wave with the wavenumber q_p that satisfies the condition

$$q_p^2 = \frac{e^2\omega^2}{D\tilde{V}(q_p)} = \frac{\kappa q_p \omega^2}{2\pi D}\,. \tag{3.40}$$

To make this result agree with Eq. 3.31, we set

$$D = \frac{e^2}{\pi\hbar^2}\,|\mu|\,, \tag{3.41}$$

which is equivalent to Eq. (3.33).

Note that $\mu \propto \sqrt{n_0}$, and so $\omega^2(q) \propto \sqrt{n_0}q$. Equation 3.30 can also be inverted to obtain q_p for a given ω. Hence, the plasmon wavelength is

$$\lambda = \frac{2e^2 v_F\sqrt{\pi}}{\kappa\hbar\omega^2}\,\sqrt{n_0}\,. \tag{3.42}$$

If n_0 is a function of position, we can use Eq. (3.40) to formally define the *local* plasmon wavelength $\lambda(x,y) = 1/q_p(x,y)$ which corresponds to the local Drude weight. Therefore, one can determine the local conductivity from the observed oscillation wavelength. In addition, $\lambda(x,y)$ can be used to calculate the local charge density from Eq. (3.42). Thus, we rewrite Eq. (3.39) as

$$U_{\text{ext}}(x,y) = U + \frac{\kappa}{2\pi e^2}\hat{V}\left[\nabla\left(\frac{1}{q_p(x,y)}\nabla U(x,y)\right)\right]\,. \tag{3.43}$$

The *most* important point of the above derivation is that the solution to Eq. (3.37) is a plane wave with the wavelength that depends on the local charge density in the manner described by Eq. (3.42).

3.3 SNOM

3.3.1 Basic Methodology

In traditional optical microscopy, the resolution of a device is ultimately limited by Raleigh criterion. Typically, one cannot resolve two light scatterers that are separated by less than a couple of hundred nanometers. It is, however,

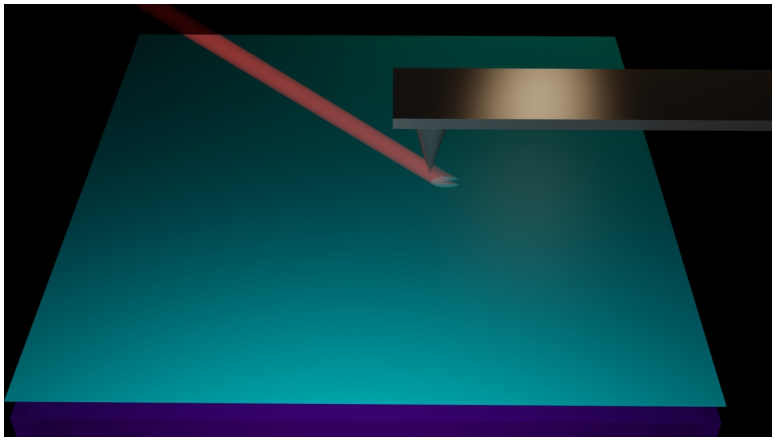

Figure 3.9: AFM tip used for scattering SNOM.

possible to use the near field signal to achieve much better resolution. The principal idea of Scanning Near-field Optical Microscopy (SNOM) is the use of evanescent waves instead of the propagating far-field signal. There are a number of near-field setups that accomplish this. The main two classes are aperture and apertureless modes. In the first case, the probe has an aperture that can be used to either illuminate the sample, collect the light, or both. The apperture size is now the limiting factor in the resolution of the device: smaller appertures focus the signal on a smaller area. The downside of using very small apertures is that the signal strength drops substantially.

Aperturless setups use sharp metallic tips, positioned close to the sample and illuminated by a laser beam. This results in the field enhancement, localized around the tip. The resolution in this case depends on the diameter of the tip. One often uses AFM tips for this purpose as they are sharp enough to achieve required resolution, see Fig. 3.9.

A very important feature of SNOM is that the wavelength becomes decoupled from the frequency. This means that one is free to choose the frequency that suits that particular system. Since plasmonic oscillations in graphene are in the terahertz range, it is possible to use infrared radiation to create these excitations. By moving the tip over the sample, it is possible to register the local response to the tip polarization which should correspond to the plasmonic modes. This is pre-

cisely the experiment performed by our collaborators from Dimitri Basov's group at UCSD where the material analyzed is graphene monolayer. In the following section, we will go over the model used for analyzing this experiment and then we will spend some time discussing two specific geometries.

3.3.2 Modeling

The goal of the modeling is to understand the imaging contrast, i.e., relative variations of the scattering amplitude S measured by s-SNOM as a function the in-plane tip position $\mathbf{r}_d$. Any quantities that do not depend on $\mathbf{r}_d$ are considered unimportant multiplicative constants and so were neglected. Our model is based on three main assumptions: (i) the point-dipole approximation for the tip, (ii) the quasi-static coupling between the tip and the sample and also among the charges inside the sample, and (iii) the local-conductivity approximation for graphene.

The point-dipole approximation is certainly crude but it has a long tradition in the literature. [39, 93, 1] One imagines that the AFM tip can be replaced by a point dipole. The desired scattering amplitude S is then proportional to the dipole moment $p_z = \chi E_z$ of this dipole. Here E_z is the out-of-plane (z-direction) electric field at the dipole position (excluding the dipole's own field) and $\chi = a^3$ is the polarizability. Neglecting the in-plane polarizability of the dipole compared to the out-of-plane helps one to mimic properties of the actual tip, which is strongly elongated. Typical choice of the adjustable parameter a is 20–30 nm, which is somewhat larger than the curvature radius of the real tip.

Since the far-field infrared reflectivity of graphene is very small, [55] the illumination of the sample area covered and uncovered by graphene is nearly the same. Therefore, the imaging contrast is predominatly due to the variations in the near-field coupling [39, 93, 1] between the dipole and the sample,

$$S(\mathbf{r}_d) = \frac{1}{1 - \chi G(\mathbf{r}_d)}\,, \tag{3.44}$$

where $G(\mathbf{r}_d)$ is the electric field generated by the sample in response to a *unit* dipole (see below).

In the experiment the AFM is used in the tapping mode and the tapping

harmonics $s_m e^{i\phi_m}$ are recorded. We model this by considering the time-dependent z_d in the form

$$z_d(t) = b + \Delta z\,(1 - \cos\Omega t)\,, \tag{3.45}$$

where $b \lesssim a$ is another adjustable parameter. Computing $s(t)$ for a suitably dense grid of t-points and taking the discrete Fourier transform at frequency $m\Omega$, the desired demodulated amplitudes $s_m e^{i\phi_m}$ are obtained.

Calculating function G as a function of $\mathbf{r}_d$ and z_d is the main part of the problem. This function is the sum of two terms:

$$G(\mathbf{r}_d) = G_s + G_g(\mathbf{r}_d)\,. \tag{3.46}$$

The first term G_s is the position-independent contribution of the SiO_2 substrate. Within the quasi-static approximation, valid if the dipole-sample distance z_d is much shorter than the wavelength $2\pi c/\omega$, it is given by the usual formula for the field of the image dipole,

$$G_s = \frac{\beta}{4z_d^3}\,, \quad \beta = 1 - \frac{1}{\kappa}\,, \tag{3.47}$$

where κ is the average of the dielectric constants above and below graphene. The second term in Eq. (3.46) is due to electrons in graphene:

$$G_g(\mathbf{r}_d) = e\frac{\partial}{\partial z_d} U_{\rm ind}(\mathbf{r}, z_d)\,, \tag{3.48}$$

see Eq. 3.36. The induced potential arises in response to the external dipole potential, given by

$$U_{\rm ext}(\mathbf{r}) = \frac{1}{\kappa}\,\frac{z_d}{(|\mathbf{r} - \mathbf{r}_d|^2 + z_d^2)^{3/2}}\,. \tag{3.49}$$

One can solve for the total $U(\mathbf{r})$ using Eq. (3.37) which leads to the induced charge density and $G_g(\mathbf{r})$.

3.3.3 Graphene Half-Plane

Numerical Approach

Consider now a more realistic situation, where graphene occupies $x \geq 0$ half-plane. Equation (3.37) is still valid if we define $\sigma(x < 0) \equiv 0$ and also add a

boundary condition $\partial U/\partial x = 0$ at $x = 0$ to preserve the continuity relation. Let us assume that $\sigma = \sigma(x)$ is invariant along y but may be a function of x. Then, without loss of generality, we can choose $y_d = 0$. The x-coordinate of the tip is L. Taking the one-dimensional Fourier transform in y of both sides of Eq. (3.37), we obtain

$$\tilde{U}(x) + 2K_0(x|q_y|) * \delta\tilde{\rho}(x, q_y) = \tilde{U}_{\text{ext}}(x, q_y) = -\frac{2}{\kappa}\,\frac{z_d}{r}\,|q_y|K_1(r|q_y|)\,, \tag{3.50}$$

$$\delta\tilde{\rho}(x, q_y) = -\frac{1}{2\pi}\left[\frac{d}{dx}\frac{1}{q_p(x)}\frac{d}{dx} - \frac{q_y^2}{q_p(x)}\right]\tilde{U}(x, q_y)\,, \tag{3.51}$$

where the convolution $(*)$ is now done along the x only, $K_\nu(z)$ is the modified Bessel function of the second kind, and $r = \sqrt{(x-L)^2 + z_d^2}$. In turn, the equation for G_d becomes

$$G_g(x_d) = -\int_0^\infty dx \int_{-\infty}^\infty \frac{dq_y}{2\pi}\,\tilde{U}_{\text{ext}}(x, q_y)\delta\tilde{\rho}(x, q_y)\,. \tag{3.52}$$

For purposes of numerical solution, these equations can be converted to linear equations of finite size. To this end instead of a semi-infinite plane, we consider a strip of a large width. We discretize the x axis and replace all derivatives by finite differences on the x-grid. The convolution integral has been replaced by an integral sum. A special care has to be taken to regularize the divergence of the Bessel functions at zero argument by requiring that the convolution gives the same result for $\delta\tilde{\rho} = \text{const}$ whether it is computed numerically or analytically at all points of the x-grid. Similarly, we introduce a grid of q_y extending up to a suitably large value. Grid parameters are adjusted to ensure that the accuracy of our solution is never less than 1%.

The sequence of steps involved in our numerical simulations is as follows. Given the profile of $q_p(x)$ and the tip coordinates (L, z_d), the matrices of the linear systems are generated as discussed above. These linear equations are solved and G_g is computed. Substituting this value into Eqs. (3.46) and then into Eq. (3.44), one computes the scattering amplitude S. These calculations are repeated for a grid of tip positions L and heights $b \le z_d \le b + 2\Delta z$. Typically, we have six to eight L points per distance $\pi/|q_p|$ in order to adequately describe the plasmon interference pattern near the edge. We also use about twenty z_d points to do the

demodulation reliably. Upon demodulation, we obtain the spatial profile of $s_3(L)$ that can be compared with the experimental data.

Comparison with experiment

The experimental setup consisted of graphene positioned on a SiO_2/Si wafer. An AFM tip located above the system was illuminated by a CO_2 $892\,\mathrm{cm}^{-1}$ laser. The SNOM data was collected by measuring the response of the graphene half-plane along a series of traces perpendicular to the edge. The signal was then averaged to reduce the effect of disorder. The experiment has demonstrated that the oscillation wavelength is larger closer to the edge and that the oscillations decay away from the edge.

The input into our simulation consists of the tip modeling parameters a, b, Δz, the value of κ, and also the profile of $q_p(x)$. We fixed $a = 30\,\mathrm{nm}$, $b = 0.7a$, $\Delta z = 40\,\mathrm{nm}$. We set $\kappa(\omega = 892\,\mathrm{cm}^{-1}) = 2.52 + 0.13i$ based on our ellipsometric measurements of SiO_2/Si wafers. For $q_p(x) = q_1(x) + iq_2(x)$ we adopted the following trial form:

$$\lambda_p(x) = \frac{2\pi}{q_1(x)} = \lambda_0 + c\,\theta(l-x)|x|^n\,, \quad q_2(x) = \gamma_p q_1(x)\,. \tag{3.53}$$

The starting values of the λ_0, c, n, and l were determined by fitting $\lambda_p(x)$ in Eq. (3.53) to the observed plasmon wavelength. A relatively high value of $n = 6$ was necessary to account for the sharp rise of the measured $\lambda_p(x)$ close to the graphene edge. For simplicity, the damping parameter γ_p was taken to be position-independent. Several representative γ_p have been considered. For each of them, the values of all other fitting parameters were manually fine-tuned by repeatedly running the simulations until the position and relative amplitude of the peaks in $s_3(L)$ agreed as close as possible with the experimental data. The best-fitting γ_p was determined to be 0.135 ± 0.1, see Fig. 3.10.

The result presented in Fig. 3.10 shows qualitative agreement with all salient features of the data but also some quantitative discrepancy between the experiment and the simulations. Such discrepancy could be in part due to the crudeness of the point-dipole approximation and also the lack of perfect translational invariance of the system along the edge.

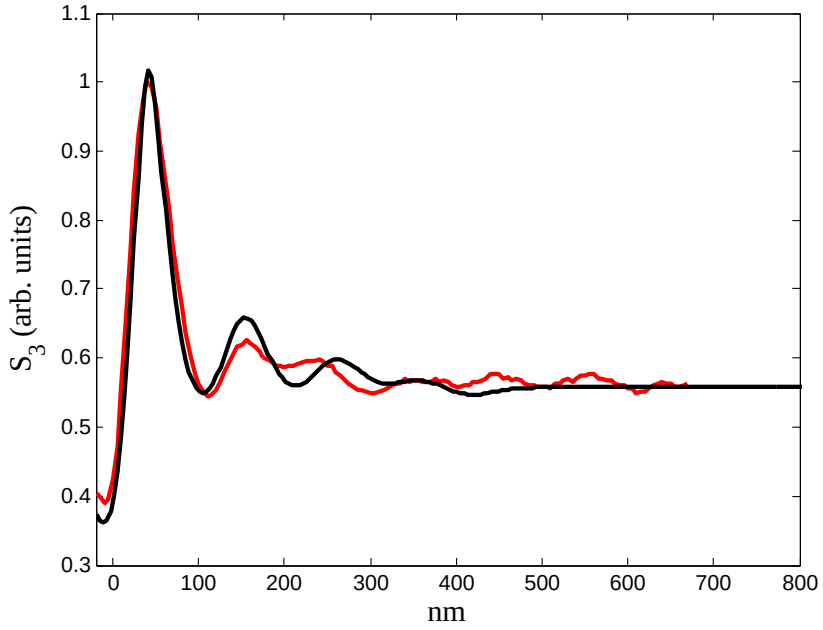

Figure 3.10: Experimental [25] (red) and numerical (black) curves showing agreement of principal features in S_3 signal.

It has been, therefore, demonstrated that our numerical approach can capture the most important features observed experimentally, even though further refinements are necessary for a better agreement.

3.3.4 Plasmons in a Flake

Another interesting geometry that has been studied using SNOM is a narrow graphene flake, see Fig. 3.11. A fascinating feature that has been observed is the presence of "bright spots"—locations inside the flake where the response is very strong. This system is very different fromt the half-plane graphene as here, due to the relative proximity of the two edges, the communication between them is not completely suppressed by damping. This means that the plasmonic mode actually couples to both edges. What makes this particular structure very exciting is that we can solve a simplified plasmon equation for it.

For this case, we rewrite Eq. (3.37) by explicitly including the variable

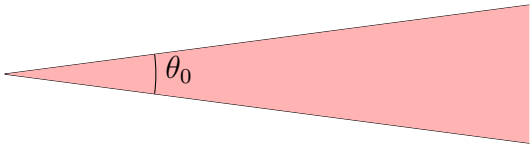

Figure 3.11: Graphene flake with the vertex angle θ_0.

wavelength in the inhomogeneous wave equation:

$$U_{\text{ext}}(x,y) = U(x,y) + \nabla\left[\lambda^2(x,y)\nabla U(x,y)\right] . \tag{3.54}$$

This is valid because narrow wires (flakes) behave as 1D systems. In the case of $\ln(1/\theta_0) \gg 1$, one may, with leading logarithmic accuracy, replace the Coulomb interaction with a delta function of strength $2(e^2/\kappa)\ln(1/\theta_0)$. The benefit of using the above expression is that while it retains the principal characteristics of the solution, it is considerably simpler as we have reduced the integro-differential equation to a differential one. If the static charge density is constant, using the standard Green's function method, the solution can be given as a sum of eigenstates. The result is given by

$$U(r,\theta) = \sum_{n=0}^{\infty} u(r)\cos\nu_n\theta\,, \tag{3.55}$$

$$u(r) = q^2\int_0^\infty dr' r' G_n(r,r') u_n^{\text{ext}}(r')\,, \tag{3.56}$$

$$G_n(r,r') = -i\frac{\pi}{2} J_{\nu_n}(qr_<)\left[J_{\nu_n}(qr_>) + iY_{\nu_n}(qr_>)\right] , \tag{3.57}$$

$$u_n^{\text{ext}} = \frac{2-\delta_{n,0}}{\theta_0}\Re\left[\int_0^{\theta_0} d\theta' e^{i\nu_n\theta'} U_{\text{ext}}\right] , \tag{3.58}$$

$$\nu_n = n\frac{\pi}{\theta_0}\,, \quad r_< \equiv \min(r,r')\,, \quad r_> \equiv \max(r,r')\,. \tag{3.59}$$

Each mode in the eigenmode expansion corresponds to the number of angular oscillations. Similarly to the case of waveguides, every mode has a turning point and modes with lower n penetrate closer to the tip. To illustrate the behavior of the solution, we impose a local perturbing potential $U_{\text{ext}} = \delta(\vec{r} - \vec{r}_S)$. For every position $\vec{r}_S$ we determine the potential at the location of the perturbation and generate a potential map over the flake. Finally, we the individual conributions of the first four modes $n = 0, 1, 2, 3$, see Fig. 3.12.

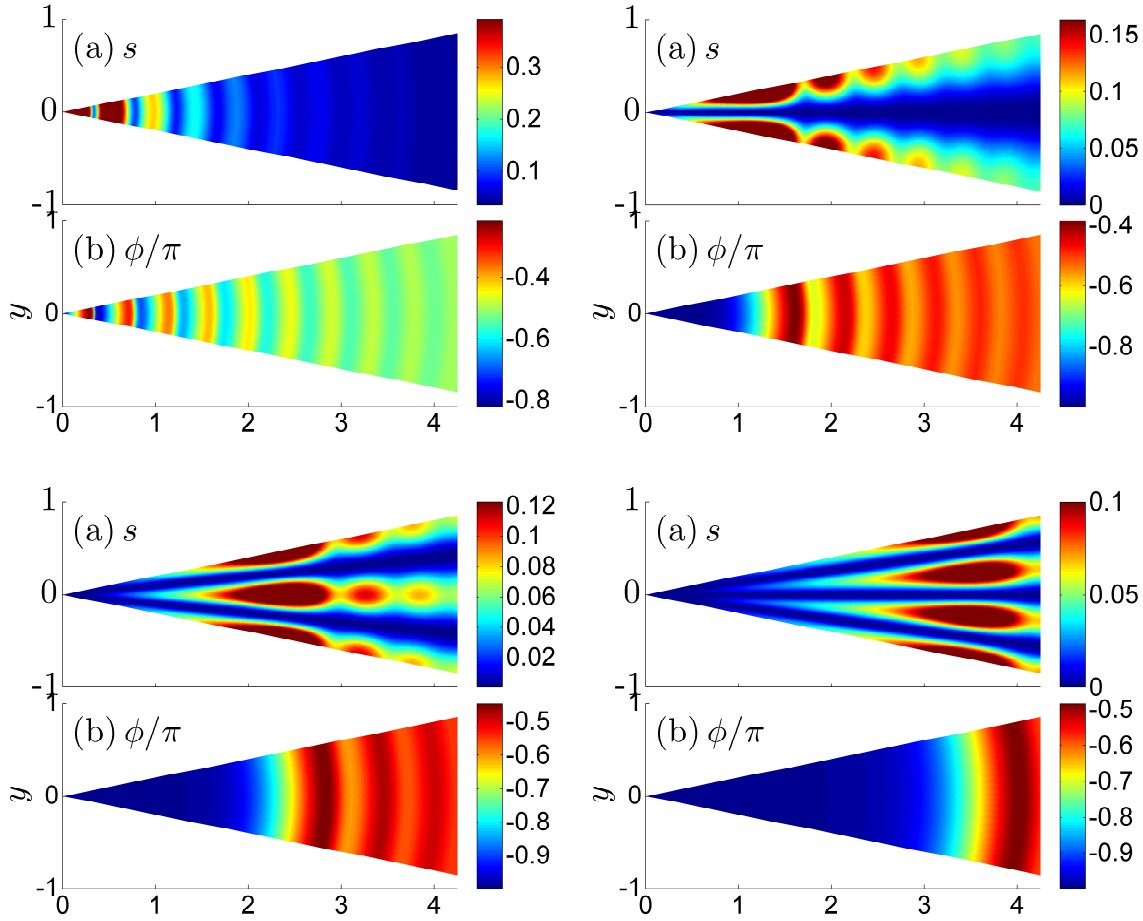

Figure 3.12: (Top row) $n = 0$, $n = 1$, (Bottom row) $n = 2$, $n = 3$. For every figure, the top illustration is the absolute value of the potential and the bottom one is the phase.

We can also conduct numerical simulations to solve Eq. (3.54) without resorting to the eigenmode expansion. To do so, we first generate a two-dimensional mesh over which the equation will be solved. In this case, our external perturbation is a dipole positioned at height z_0 above the flake. By solving Eq. (3.54), we determine the potential right under the dipole which corresponds to the charge density at that point. Just like before, we move the perturbation over the flake to generate a density map.

Here, we also treat a system with a constant charge density. Since, in reality, we expect damping, an imaginary component is included in the wavelength. The solution is shown in Fig. 3.13. Upon comparing our numerical simulations with the prior analytical derivation, one can see that despite the different nature of perturbation, there are qualitative similarities between the plots.

Let us now discuss the nature of the modes in the flake. The simplest observable feature is the angular oscillation in potential. This is due to the cosine term which takes on the value of 1 at the edges of the flake. One needs to keep in mind that the edges of a narrow flake are not independent entities, instead carrying the same mode together. Higher mode numbers have shorter cosine period which results in more oscillations.

Another characteristic of the modes that can be seen from the plots is the difference of how closely they come to the corner. A convenient analogy for our situation is the case of waveguides. In a hollow rectangular waveguide we can have modes whose allowed transverse momenta depend on the geometry of the waveguide. For each particular mode, there is a cutoff frequency (itself dependent on the geometry) below which the mode may not propagate. The wave number for a wave of frequency ω is $k_\parallel = \sqrt{\omega^2 - \omega_{\text{cut}}^2}/c = \sqrt{q^2 - k_\perp^2}$. Clearly, if the frequency is below the cutoff, the wave number is imaginary and the wave is attenuated. A very similar situation can be seen in our case. Modes of higher number must have a higher momentum in the angular direction. This momentum also increases as the wave gets closer to the corner and the width of the flake gets smaller. One can write the total wave number of the mode as

$$q = \sqrt{k_\parallel^2 + k_\perp^2} = \sqrt{k_\parallel^2 + \left(\frac{\nu_n}{r}\right)^2}. \tag{3.60}$$

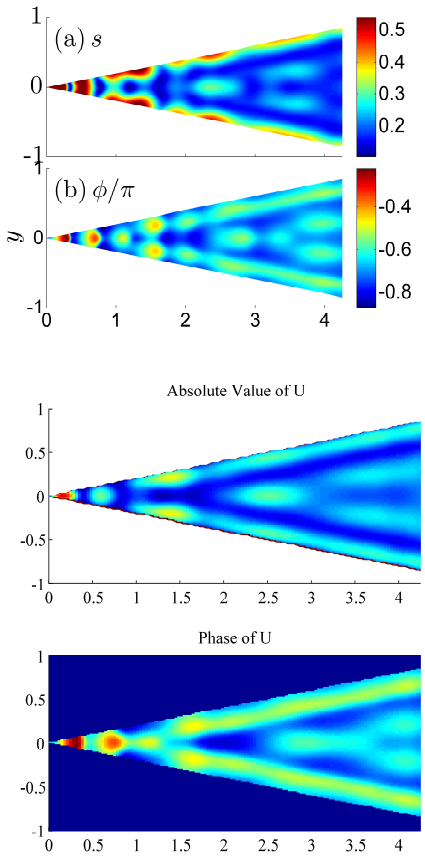

Figure 3.13: (Top Pair) Eigenvalue expansion. The absolute value is plotted above the phase. (Bottom Pair) Solution by the standard finite-element method with the dipole perturbation.

Far away from the corner, the mode is a plane wave with momentum q. However, as it gets closer to the tip of the flake, the transverse momentum becomes important. When $k_{\|}$ becomes zero, the wave reaches its turning point and this occurs at

$$r = \frac{\nu_n}{q} \,. \tag{3.61}$$

For smaller r, the wave number $k_{\|}$ is imaginary, which results in the attentuation of the wave, as seen in waveguides. From this expression, we can see that only $n = 0$ mode can actually reach the corner as all the others will be turned around at larger r. This is precisely what we obtain with higher n modes beginning to get attenuated farther from the corner.

As of now, we have explained the cutoff of the mode propagation. However,

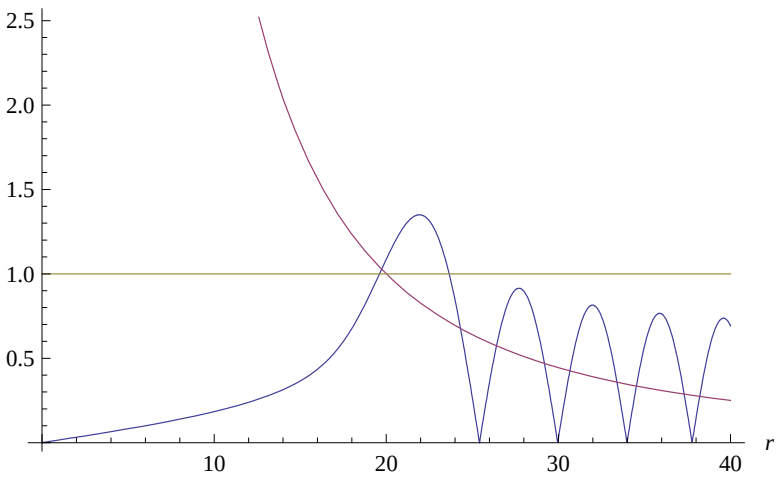

Figure 3.14: The maximum of $|\psi_j(r)|^2$ is slightly to the right of the turning point.

we still need to rationalize the signal maximum that is observed around the cutoff point. These are the bright spots observed experimentally. To do so, we perform a substitution $\psi_j(r) = \sqrt{r}u_j(r)$. This allows us to rewrite Eq. (3.54) after a separation of variables as a Schrödinger's equation:

$$-\psi_j''(r) + V_j(r)\psi(r) = q^2\psi_j(r)\,, \tag{3.62}$$

$$V_j(r) = \frac{4\nu_j^2 - 1}{4r^2}\,. \tag{3.63}$$

Solving the equation and plotting the solution along with the potential and $q^2 = 1$ on the common axes shows that the maximum of $|\psi_j(r)|^2$ lies just right of the turning point of the solution, see Fig. 3.14 More precisely, it is located at $qr_j = \nu_j + (\nu_j/2)^{1/3}$.

The complex potential pattern seen in Fig. 3.13 is the result of the interference of the modes as they propagate through the flake. It is important to note that if one were to consider the flake only up to $r = R_0$, one would only need $N = R_0 q\theta_0/\pi$ modes in the analysis as those with $n > N$ do not penetrate into the region under consideration.

These rigid mode cutoffs can function as filters for certain modes. Using constrictions in the geometry allows one to control which modes are allowed to propagate and which ones are reflected. This would permit one to use the flakes for injecting plasmon modes into other structures in a controlled fashion by changing

the point of contact between the two systems. A way to check this effect would be to use two tips positioned over the two subsystems: one of the tips serves to launch the plasmons in the flake and the other one picks up the modes that make it to the other side of the constriction. In an ideal situations, the two subsystems would be mirror images of each other which would allow one to see the different mode profiles on both sides of the narrow point.

3.4 Future work

Currently, plasmonics in graphene is still the main focus of the research. A major problem that needs to be investigated is the finite lifetime of plasmons. As was seen in the SNOM experiments, they experience a significant damping in amplitude along their path of propagation. This is the result of higher order dissipative processes, not captured by the RPA. More specifically, this behavior originates from the imaginary part of the quasi-particle self-energy. For now, this problem remains unsolved due to its analytical intractability and high demand of resources for a numerical approach. Nevertheless, understanding the finite lifetime of plasmons is crucial for being able to control their propagation in the system. Such tunable plasmonic structures can be utilized for signal transfer at frequencies much higher than the traditional electronic ones.

The second major question that needs to be answered is the inhomogeneous charge density in graphene. Experimental results consistently show the variation of the plasmonic wavelength throughout the system which translates to non-constant background charge. The reason behind this charge variation is not entirely clear. Some possible explanations involve dopands and electronic traps. Clear understanding of the charge distribution in ungated graphene would help to explain graphene's dependence on these foreign elements. This would allow for a better control of graphene plasmons by varying the local wavelength. From a more general standpoint, understanding the origin of the intrinsic charge variation is crucial in manufacturing of devices.

Bibliography

[1] J. Aizpurua, T. Taubner, F. J. G. de Abajo, M. Brehm, and R. Hilenbrand. Substrate-enhanced infrared near-field spectroscopy. *Opt. Express*, 16:1529, 2008.

[2] D. I. Aladashvili and Z. A. Adamia. High-field hopping and 'hopping domains'. *Phil. Mag. B*, 81:1033–1047, Sept. 2001.

[3] A. N. Aleshin, H. J. Lee, S. H. Jhang, H. S. Kim, K. Akagi, and Y. W. Park. Coulomb-blockade transport in quasi-one-dimensional polymer nanofibers. *Phys. Rev. B*, 72(15):153202, Oct 2005.

[4] A. N. Aleshin, H. J. Lee, Y. W. Park, and K. Akagi. One-dimensional transport in polymer nanofibers. *Phys. Rev. Lett.*, 93:196601, 2004.

[5] A. N. Aleshin, J. Y. Lee, S. W. Chu, S. W. Lee, B. Kim, S. J. Ahn, and Y. W. Park. Hopping conduction in polydiacetylene single crystals. *Phys. Rev. B*, 69(21):214203, Jun 2004.

[6] B. L. Altshuler, V. E. Kravtsov, I. V. Lerner, and I. L. Aleiner. Jumps in current-voltage characteristics in disordered films. *Phys. Rev. Lett.*, 102:176803, 2009.

[7] V. I. Arkhipov and H. Bässler. Field-dependent effective temperature of localized charge carriers in hopping systems with a random energy distribution. *Phil. Mag. Lett.*, 69(4):241–246, 1994.

[8] M. Y. Azbel and D. P. DiVincenzo. Finite-temperature conductance in one dimension. *Phys. Rev. B*, 30(12):6877–6888, Dec 1984.

[9] A. Bachtold, M. de Jonge, K. Grove-Rasmussen, P. L. McEuen, M. Buitelaar, and C. Schönenberger. Suppression of tunneling into multiwall carbon nanotubes. *Phys. Rev. Lett.*, 87(16):166801, 2001.

[10] H. Bahlouli, K. A. Matveev, D. Ephron, and M. R. Beasley. Coulomb correlations in hopping through a thin layer. *Phys. Rev. B*, 49:14496–14503, 1994.

[11] L. Balents. Orthogonality catastrophes in carbon nanotubes. In D. C. Glattli and M. Sanquer, editors, *XVIII Moriond Les Arcs Conference Proceedings*, Paris, 1999. Edition Frontiers.

[12] A. D. Ballard and M. E. Raikh. Regimes of correlated hopping via a two-site interacting chain. *Phys. Rev. B*, 74:035117, 2006.

[13] C. W. J. Beenakker. Random-matrix theory of quantum transport. 69(3):731–808, 1997.

[14] L. Berlyand and J. Wehr. The probability distribution of the percolation threshold in a large system. *J. Phys. A*, 28:7127, 1995.

[15] M. Bockrath, D. H. Cobden, J. Lu, A. G. Rinzler, R. E. Smalley, L. Balents, and P. L. McEuen. Luttinger-liquid behaviour in carbon nanotubes. *Nature*, 397:598, 1999.

[16] H. Böttger and V. V. Bryksin. Investigation of non-ohmic hopping conduction by methods of percolation theory. *Phil. Mag. B*, 42(2):297–310, 1980.

[17] W. Brenig, G. H. Döhler, and H. Heyszenau. Hopping conductivity in highly anisotropic systems. *Phil. Mag.*, 27:1093, 1973.

[18] A. M. Chang. Chiral luttinger liquids at the fractional quantum hall edge. *Rev. Mod. Phys.*, 75:1449, 2003.

[19] J. C. Coiffic, M. Fayolle, S. Maitrejean, L. E. F. Foa Torres, and H. L. Poche. Conduction regime in innovative carbon nanotube via interconnect architectures. *Appl. Phys. Lett.*, 91(25):252107, 2007.

[20] C. N. Colesniuc, R. R. Biswas, S. A. Hevia, A. V. Balatsky, and I. K. Schuller. Exponential behavior of the ohmic transport in organic films.

[21] J.-F. Dayen, T.L.Wade, G. Rizza, D. Golubev, C.-S. Cojocaru, D. Pribat, X. Jehl, M. Sanquer, and J.-E.Wegrowe. Conductance of disordered semiconducting nanowires and carbon nanotubes: a chain of quantum dots. *Eur. Phys. J. Appl. Phys.*, 48:10604, 2009.

[22] R. W. V. der Heijden, G. Chen, A. T. A. M. de Waele, H. M. Gijsman, and F. P. B. Tielen. Nonlinear current-voltage characteristics of ion-implanted si:as in the hopping transport regime. *Phil. Mag.*, 65:849, 1992.

[23] V. V. Deshpande, M. Bockrath, L. I. Glazman, and A. Yacoby. Electron liquids and solids in one dimension. *Nature*, 464(7286):209–216, 2010.

[24] E. W. Dijkstra. A note on two problems in connexion with graphs. *Numerische Mathematik*, 1:269–271, 1959.

[25] Z. Fei, A. S. Rodin, G. O. Andreev, W. Bao, A. S. McLeod, L. M. Zhang, G. Dominguez, M. Thiemens, M. M. Fogler, A. H. Castro-Neto, C. N. Lau, F. Keilmann, and D. N. Basov. Gate-tunable plasmons in graphene revealed by infrared nano-imaging.

[26] M. M. Fogler and R. S. Kelley. Non-ohmic variable-range hopping transport in one-dimensional conductors. *Phys. Rev. Lett.*, 95:166604, 2005.

[27] M. M. Fogler, S. V. Malinin, and T. Nättermann. Coulomb blockade and transport in a chain of one-dimensional quantum dots. *Phys. Rev. Lett.*, 97:096601, 2006.

[28] M. M. Fogler, S. Teber, and B. I. Shklovskii. Variable-range hopping in quasi-one-dimensional electron crystals. *Phys. Rev. B*, 69:035413, 2004.

[29] A. B. Fowler, A. Hartstein, and R. A. Webb. Conductance in restricted-dimensionality accumulation layers. *Phys. Rev. Lett.*, 48(3):196–199, Jan 1982.

[30] M. Galeazzi, D. Liu, D. McCammon, L. E. Rocks, W. T. Sanders, B. Smith, P. Tan, J. E. Vaillancourt, K. R. Boyce, R. Brekosky, J. D. Gygax, R. Kelley, F. S. Porter, C. K. Stahle, C. M. Stahle, and A. E. Szymkowiak. Hot-electron effects in strongly localized doped silicon at low temperature. *Phys. Rev. B*, 76:155207, 2007.

[31] B. Gao, D. C. Glattli, B. Plaçais, and A. Bachtold. Cotunneling and one-dimensional localization in individual disordered single-wall carbon nanotubes: Temperature dependence of the intrinsic resistance. *Phys. Rev. B*, 74:085410, 2006.

[32] B. Gao, A. Komnik, R. Egger, D. C. Glattli, and A. Bachtold. Evidence for luttinger-liquid behavior in crossed metallic single-wall nanotubes. *Phys. Rev. Lett.*, 92:216804, 2004.

[33] M. E. Gershenson, Y. B. Khavin, D. Reuter, and P. S. A. D. Wieck. Hot-electron effects in two-dimensional hopping with a large localization length. *Phys. Rev. Lett.*, 85:1718, 2000.

[34] T. Giamarchi. *Quantum Physics in One Dimension.* Oxford, New Dehli, 2004.

[35] L. I. Glazman and K. A. Matveev. Inelastic tunneling across thin amorphous films. *Sov. Phys. JETP*, 67:332, 1988.

[36] M. Y. Han, J. C. Brant, and P. Kim. Electron transport in disordered graphene nanoribbons. *Phys. Rev. Lett.*, 104:056801, 2010.

[37] L. He, E. Kogan, and D. Luo. Shortest path across a mesoscopic system. *Phys. Rev. B*, 67(11):113201, Mar 2003.

[38] R. M. Hill. Hopping conduction in amorphous solids. *Phil. Mag.*, 24(192):1307–1325, 1971.

[39] R. Hillenbrand and F. Keilmann. Complex optical constants on a subwavelength scale. *Phys. Rev. Lett.*, 85:3029, 2000.

[40] J.-P. Hovi and A. Aharony. Scaling and universality in the spanning probability for percolation. *Phys. Rev. E*, 53:235, 1996.

[41] R. J. F. Hughes, A. K. Savchenko, J. E. F. Frost, E. H. Linfield, J. T. Nicholls, M. Pepper, E. Kogan, and M. Kaveh. Distribution function analysis of mesoscopic hopping conductance fluctuations. cond-mat/9603058 (March 1996).

[42] A. Kanda, K. Tsukagoshi, Y. Aoyagi, and Y. Ootuka. Gate-voltage dependence of zero-bias anomalies in multiwall carbon nanotubes. *Phys. Rev. Lett.*, 92:036801, 2004.

[43] C. L. Kane and M. P. A. Fisher. Transmission through barriers and resonant tunneling in an interacting one-dimensional electron gas. *Phys. Rev. B*, 46:15233–152620, 1992.

[44] Y. B. Khavin, M. E. Gershenson, and A. L. Bogdanov. Strong localization of electrons in quasi-one-dimensional conductors. *Phys. Rev. B*, 58(12):8009–8019, Sep 1998.

[45] J. Kurkijärvi. Hopping conductivity in one dimension. *Phys. Rev. B*, 8:922–924, 1973.

[46] F. Ladieu and J. P. Bouchaud. Conductance statistics in small gaas:si wires at low temperatures. i. theoretical analysis: truncated quantum fluctuations in insulating wires. *J. Phys. I (France)*, 3:2311–2320, Nov 1993.

[47] F. Ladieu, D. Mailly, and M. Sanquer. Conductance statistics in small insulating gaas:si wires at low temperature. ii: experimental study. *J. Phys. I (France)*, 3:2321–2341, Nov 1993.

[48] F. Ladieu, M. Sanquer, and J. P. Bouchaud. Depinning transition in mott-anderson insulators. *Phys. Rev. B*, 53(3):973–976, Jan 1996.

[49] A. I. Larkin and D. E. Khmel'nitskii. Activation conductivity in disordered systems with large localization length. *Sov. Phys. JETP*, 56(3):647–52, September 1982.

[50] P. A. Lee. Variable-range hopping in finite one-dimensional wires. *Phys. Rev. Lett.*, 53:2042, 1984.

[51] R. Leturcq, D. L'Hote, R. Tourbot, V. Senz, U. Gennser, T. Ihn, K. Ensslin, G. Dehlinger, and D. Grutzmacher. Hot hole effects in a dilute two-dimensional gas in sige. *Europhys. Lett.*, 61:499, 2003.

[52] E. Levin and B. I. Shklovskii. Low-temperature hopping conduction in strong electric field. computer experiment. *Sov. Phys. Semicond.*, 11:534, 1984.

[53] E. I. Levin, I. M. Ruzin, and B. I. Shklovskii. Transverse hopping conductivity of amorphous films in strong electric fields. *Sov. Phys. Semicond.*, 22:401, 1988.

[54] E. I. Levin and B. I. Shklovskii. Negative differential conductivity of low density electron gas in random potential. *Solid State Commun.*, 67(3):233–237, 1988.

[55] Z. Q. Li, E. A. Henriksen, Z. Jiang, Z. Hao, M. C. Martin, P. Kim, H. L. Stormer, and D. N. Basov. Dirac charge dynamics in graphene by infrared spectroscopy. *Nat. Phys.*, 4:532, 2008.

[56] Y. Z. Long, J. L. Duvail, M. M. Li, C. Gu, Z. Liu, and S. P. Ringer. Electrical conductivity studies on individual conjugated polymer nanowires: Two-probe and four-probe results. *Nanoscale Res Lett*, 5:237, 2010.

[57] S. Marianer and B. I. Shklovskii. Effective temperature of hopping electrons in a strong electric field. *Phys. Rev. B*, 46:13100–13103, 1992.

[58] S. Marnieros, L. Bergé, A. Juillard, and L. Dumoulin. Dynamical properties near the metal-insulator transition: Evidence for electron-assisted variable range hopping. *Phys. Rev. Lett.*, 84:2469–2472, 2000.

[59] J. A. McInnes, P. N. Butcher, and G. P. Triberis. Numerical calculations of non-ohmic hopping conductivity in one-dimensional systems. *J. Phys.: Condens. Mat.*, 2(38):7861–7865, 1990.

[60] A. Miller and E. Abrahams. Impurity conduction at low concentrations. *Phys. Rev.*, 120(3):745–755, Nov 1960.

[61] E. G. Mishchenko, A. V. Andreev, and L. I. Glazman. Zero-bias anomaly in disordered wires. *Phys. Rev. Lett.*, 87(24):246801, 2001.

[62] M. Monteverde, G. Garbarino, M. Núñez-Reguiero, J. Souletie, C. Acha, X. Jing, L. Lu, Z. W. Pan, S. S. Xie, and R. Egger. Tomonaga-luttinger liquid and coulomb blockade in multiwall carbon nanotubes under pressure. *Phys. Rev. Lett.*, 97:176401, 2006.

[63] N. F. Mott. Conduction in non-crystalline systems. vii. non-ohmic behaviour and switching. [ovshinsky switches]. *Phil. Mag.*, 24(190):911–34, 1971.

[64] A. V. Nenashev, F. Jansson, S. D. Baranovskii, R. Österbacka, A. V. Dvurechenskii, and F. Gebhard. Hopping conduction in strong electric fields: Negative differential conductivity. *Phys. Rev. B*, 78(16):165207, 2008.

[65] A. H. C. Neto, F. Guinea, N. M. R. Peres, K. S. Novoselov, and A. K. Geim. The electronic properties of graphene. *Rev. Mod. Phys.*, 81:109, 2009.

[66] M. E. J. Newman and R. M. Ziff. Fast monte carlo algorithm for site or bond percolation. *Phys. Rev. E*, 64:016706, 2001.

[67] V. L. Nguyen and B. I. Shklovskii. Hopping conduction in strong electric fields and directed percolation. *Solid State Communication*, 38(2):99 – 102, 1981.

[68] K. S. Novoselov, A. K. Geim, S. V. Morozov, D. Jiang, Y. Zhang, S. V. Dubonos, I. V. Grigorieva, and A. A. Firsov. Electric field effect in atomically thin carbon films. *Science*, 306:666, 2004.

[69] J. B. Oostinga, H. B. Heersche, X. Liu, A. F. Morpurgo, and L. M. K. Vandersypen. Gate-induced insulating state in bilayer graphene devices. *Nature Mater.*, 7:151, 2007.

[70] A. O. Orlov, M. E. Raikh, I. M. Ruzin, and A. K. Savchenko. Statistical properties of mesoscopic conductivity fluctuations in a short-channel gaas field-effect transistor. *Sov. Phys. JETP*, 69(6):1229–1236, 1989.

[71] M. Ovadia, B. Sacépé, and D. Shahar. Electron-phonon decoupling in disordered insulators. *Phys. Rev. Lett.*, 102(17):176802, 2009.

[72] Y. Park. Tunnel hopping conductivity of an amorphous film. *Solid State Commun.*, 115:281, 2000.

[73] M. Pollak and J. J. Hauser. Note on the anisotropy of the conductivity in thin amorphous films. *Phys. Rev. Lett.*, 31:1304, 1973.

[74] M. Pollak and I. Riess. A percolation treatment of high-field hopping transport. *J. Phys. C*, 9(12):2339–2352, 1976.

[75] A. Rahman and M. K. Sanyal. Bias dependent crossover from variable range hopping to power law characteristics in the resistivity of polymer nanowires. *J. Phys.: Condens. Matter*, 22:175301, 2010.

[76] M. E. Raikh and I. M. Ruzin. Transparency fluctuations in randomly inhomogeneous barriers of finite area. *Sov. Phys. JETP*, 65:1273–1982, 1987.

[77] M. E. Raikh and I. M. Ruzin. Fluctuations of the hopping conductance of one-dimensional systems. *Sov. Phys. JETP*, 68:642–647, 1989.

[78] M. E. Raikh and I. M. Ruzin. Size effect in the longitudinal hopping conduction of a narrow two-dimensional channel. *Phys. Rev. B*, 42(17):11203–11207, Dec 1990.

[79] A. S. Rodin and M. M. Fogler. Apparent power-law behavior of conductance in disordered quasi-one-dimensional systems. *Phys. Rev. Lett.*, 105:106801, 2010.

[80] I. M. Ruzin. Fine structure of hopping conductance fluctuations in finite-size semiconductors. *Phys. Rev. B*, 43:11864, 1991.

[81] M. Sassetti and U. Weiss. Transport of 1d interacting electrons through barriers and effective tunneling density of states. *Europhys. Lett.*, 27:311, 1994.

[82] K. Schönhammer and V. Meden. Correlation effects in photoemission from low dimensional metals. *J. Electron Spectrosc. Relat. Phenom.*, 62:225–236, 1993.

[83] R. A. Serota, R. K. Kalia, and P. A. Lee. New aspects of variable-range hopping in finite one-dimensional wires. *Phys. Rev. B*, 33:8441–8446, 1986.

[84] V. K. S. Shante, C. M. Varma, and A. N. Bloch. Hopping conductivity in one-dimensional disordered compounds. *Phys. Rev. B*, 8(10):4885–4889, 1973.

[85] B. I. Shklovskii. Hopping conduction in semiconductors in a strong electric field. *Sov. Phys. Semicond.*, 6:1964, 1973.

[86] B. I. Shklovskii. Nonohmic hopping conduction. *Sov. Phys. Semicond.*, 10(8):855–860, 1976.

[87] B. I. Shklovskii and A. L. Efros. *Electronic Properties of Doped Semiconductors*. Springer-Verlag, Berlin, 1984.

[88] E. Slot, M. A. Holst, H. S. J. van der Zant, and S. V. Zaitsev-Zotov. One-dimensional conduction in charge-density-wave nanowires. *Phys. Rev. Lett.*, 93:176602, 2004.

[89] P. Stephanyi, C. C. Zammit, P. Fozooni, M. J. Lea, and G. Ensell. A new critical point in the non-linear conductivity due to variable-range hopping in si. *J. Phys.: Condens. Matter*, 9:881–888, 1997.

[90] J. Talamantes, M. Pollak, and R. Baron. Moderate-field variable-range hopping transport. *J. Non-Cryst. Solids*, 97-98:555–558, 1987.

[91] A. V. Tartakovski. Conductivity fluctuations and the superlinear current-voltage characteristics in one-dimensional disordered systems. *Phys. Lett. A*, 174(1-2):133 – 138, 1993.

[92] A. V. Tartakovskii, M. V. Fistul', M. E. Raikh, and I. M. Ruzin. Hopping conductivity of metal-semiconductor-metal contacts. *Sov. Phys. Semicond.*, 21:603–608, 1987.

[93] T. Taubner, F. Keilmann, and R. Hillenbrand. Nanomechanical resonance tuning and phase effects in optical near-field interaction. *Nano Lett.*, 4:1669, 2004.

[94] T. B. Tran, I. S. Beloborodov, X. M. Lin, T. P. Bigioni, V. M. Vinokur, and H. M. Jaeger. Multiple cotunneling in large quantum dot arrays. *Phys. Rev. Lett.*, 95:076806, 2005.

[95] Y. Tserkovnyak, B. I. Halperin, O. M. Auslaender, and A. Yacoby. Interference and zero-bias anomaly in tunneling between luttinger-liquid wires. *Phys. Rev. B*, 68:125312, 2003.

[96] L. Venkataraman, Y. S. Hong, and P. Kim. Electron transport in a multichannel one-dimensional conductor: Molybdenum selenide nanowires. *Phys. Rev. Lett.*, 96:076601, 2006.

[97] N. Wang, F. C. Wellstood, B. Sadoulet, E. E. Haller, and J. Beeman. Electrical and thermal properties of neutron-transmutation-doped ge at 20 mk. *Phys. Rev. B*, 41:3761, 1990.

[98] R. A. Webb, A. B. Fowler, A. Hartstein, and J. J. Wainer. Hopping conduction in quasi-one-dimensional systems. *Surf. Sci.*, 170(1-2):14–27, 1986.

[99] J. H. Worne, J. E. Anthony, and D. Natelson. Transport in organic semiconductors in large electric fields: From thermal activation to field emission. *Appl. Phys. Lett.*, 96:053308, 2010.

[100] B. Wunsch, T. Stauber, F. Sols, and F. Guinea. Dynamical polarization of graphene at finite doping. *New J. Phys.*, 8:318, 2006.

[101] Y. Xu, D. Ephron, and M. R. Beasley. Directed inelastic hopping of electrons through meta-insulator-metal tunnel junctions. *Phys. Rev. B*, 52:2843, 1995.

[102] Z. Yao, H. W. C. Postma, L. Balents, and C. Dekker. Carbon nanotube intramolecular junctions. *Nature*, 402:273, 1999.

[103] J. Yoshida and T. Nagano. Tunneling and hopping conduction via localized states in thin prba2cu3o7-x barriers. *Phys. Rev. B*, 55:11860, 1997.

[104] Z. G. Yu, D. L. Smith, A. Saxena, R. L. Martin, and A. R. Bishop. Molecular geometry fluctuations and field-dependent mobility in conjugated polymers. *Phys. Rev. B*, 63(8):085202, Feb 2001.

[105] J. D. Yuen, R. Menon, N. E. Coates, E. B. Namdas, S. Cho, S. T. Hannahs, D. Moses, and A. J. Heeger. Nonlinear transport in semiconducting polymers at high carrier densities. *Nature Mater.*, 8:572, 2009.

[106] S. V. Zaitsev-Zotov, Y. A. Kumzerov, Y. A. Firsov, and P. Monceau. Luttinger-liquid-like transport in long insb nanowires. *J.Phys.:Condens. Matter*, 12:303–309, 2000.

[107] J. Zhang, W. Cui, M. Juda, D. McCammon, R. L. Kelley, S. H. Moseley, C. K. Stahle, and A. E. Szymkowiak. Non-ohmic effects in hopping conduction in doped silicon and germanium between 0.05 and 1 k. *Phys. Rev. B*, 57:4472, 1998.

[108] Z. Zhou, K. Xiao, R. Jin, D. Mandrus, J. Tao, D. Geohegan, and S. Pennycook. One-dimensional electron transport in cu-tetracyanoquinodimethane organic nanowires. *Appl. Phys. Lett.*, 90:193115, 2007.